A Verification Suite of Test Cases for the Barotropic Solver of Ocean Models

Siddhartha Bishnu[1,2,5], Mark R. Petersen[1], Bryan Quaife[2,3], and Joseph Schoonover[4]

[1]Computational Physics and Methods Group, Los Alamos National Laboratory
[2]Department of Scientific Computing, Florida State University
[3]Geophysical Fluid Dynamics Institute, Florida State University
[4]Fluid Numerics
[5]Department of Earth, Atmospheric, and Planetary Sciences, Massachusetts Institute of Technology

Key Points:

- A suite of test cases is presented for the verification of barotropic dynamics of ocean models, with exact and manufactured solutions.
- Specifications are provided for the coastal Kelvin wave, the inertia-gravity wave, the planetary and topographic Rossby waves, the barotropic tide, and non-linear cases.
- Results are presented for a variety of time-stepping methods and two types of spatial discretizations: TRiSK and Discontinuous Galerkin Spectral Element Method.

Corresponding author: Siddhartha Bishnu, siddhartha.bishnu@gmail.com

Abstract

The development of any atmosphere or ocean model warrants a suite of test cases to verify its spatial and temporal discretizations, order of accuracy, stability, reproducability, portability, scalability, etc. In this paper, we present a suite of shallow water test cases designed to verify the barotropic solver of atmosphere and ocean models. These include the non-dispersive coastal Kelvin wave; the dispersive inertia-gravity wave; the dispersive planetary and topographic Rossby waves; the barotropic tide; and a non-linear manufactured solution. These test cases check the implementation of the linear pressure gradient term; the linear constant or variable-coefficient Coriolis and bathymetry terms; and the non-linear advection terms. Simulation results are presented for a variety of time-stepping methods as well as two spatial discretizations: a mimetic finite volume method based on the TRiSK scheme, and a high-order discontinuous Galerkin spectral element method. The experimental procedure for conducting these numerical experiments is detailed. It underscores several key considerations that vary depending on the chosen spatial discretization method. Finally, convergence studies of every test case are conducted with refinement in both space and time, only in space, and only in time. The convergence slopes match the expected theoretical predictions.

Plain Language Summary

Before running an atmosphere, ocean, or a coupled climate simulation, every model developer should ensure the correct implementation of each term in the governing equations that drive the models forward in time. This motivates the development of idealized test cases, each of which verifies a subset of terms in the governing equations with different initial and boundary conditions. Here we present a suite of six test cases for the momentum equation and sea surface height equation for ocean models in a single-layer configuration. The computed results from the ocean model can be compared to exact solutions. The computed solution always has a small error, but is said to converge to the exact solution with reduction in grid cell size and time step. If the model converges at the expected rate, then we know that it is solving the governing equations correctly. We show results of convergence tests from two models, and share the full specifications of these test cases so that other ocean modelers may reproduce them.

1 Introduction

The verification of spatial and temporal discretizations is an important step in the development of any computational physics model based on partial differential equations (PDEs). Verification suites, with tests of increasing complexity that exercise a subset of terms, are particularly useful to identify problems as well as to compare discretization methods. Analysis metrics include the order of accuracy, stability, reproducibility, portability, computational performance, and scalability to large core counts. Atmosphere and ocean models are no different in this regard. Numerous test cases (TC) have been implemented in these models for benchmarking their results and performance against accepted standards (Bishnu et al., 2023). In this introduction, we provide an overview of the most influential test cases for geophysical fluids, and those that inspired the development of this paper. Additionally, we show that the shallow water test cases presented here satisfy a need in ocean model verification that is not provided in previous publications.

We start with the work of D. L. Williamson et al. (1992) that was published over three decades ago. They introduced a set of seven test cases for the discretized shallow water equations in a spherical geometry:

(i) advection of a cosine bell with compact support around the sphere;
(ii) a zonal geostrophically balanced flow, which is a steady state solution of the full non-linear shallow water equations;

(iii) a steady state non-linear zonal geostrophic flow, almost equivalent to (ii), except with a compactly supported non-zero wind field;
(iv) forced non-linear advection of a translating low pressure center superimposed on a jet stream that is symmetric about the equator;
(v) zonal flow impinging on an isolated mountain;
(vi) Rossby-Haurwitz waves, representing exact solutions to the non-linear nondivergent barotropic vorticity equation; and
(vii) a numerical experiment initialized from observed atmospheric states, with results compared to the finest possible resolution.

The Williamson test cases have been adopted as verification tools by numerous atmosphere and ocean models, including spectral element models in spherical geometries (Taylor et al., 1997; Thomas & Loft, 2002) and continuous Galerkin spectral element dynamical core in the Community Atmosphere Model (CAM) version 5 (Dennis et al., 2012), computational performance in CAM Evans et al. (2019), and others (Spotz et al., 2015). The Williamson cases are so frequently used that they are the canonical set of tests for new geophysical fluid dynamical cores (Walko & Avissar, 2008; T. D. Ringler et al., 2010). Our group has recently used Williamson test cases to verify local time-stepping schemes (Capodaglio & Petersen, 2022) and to measure improvements in stability and accuracy in the TRiSK scheme (Calandrini et al., 2021).

The Aqua-Planet Experiment (APE) was first proposed by Neale and Hoskins (2000) as a benchmark for atmospheric general circulation models (AGCMs), and its aims were summarized by Blackburn and Hoskins (2013). The model setup consists of an idealised ocean-covered Earth, thereby eliminating the effect of topography and land on atmospheric flow. Surface forcing is provided by sea surface temperature varying only in latitude. Such an intermediate APE is more complex than a dry dynamical core experiment, but simpler than a full-climate simulation coupled to active land, ocean, and ice models. Therefore, the APE bridges the gap between realistic simulation and conceptual models of atmospheric phenomena in the existing modeling hierarchy. Despite these simplifications, APEs have produced realistic climate features like transient high and low pressure systems, convectively coupled equatorial waves, and tropical cyclones. Blackburn et al. (2013) compared climate simulations with 16 atmospheric general circulation models (AGCMs) on an aquaplanet, with the idealised configuration designed to expose differences in the circulation simulated by these models. APEs were performed with the variable-resolution spectral element dynamical core of CAM by Zarzycki et al. (2014), and the fundamental characteristics of the aquaplanet climate simulated by CAM5.3 are described in Medeiros et al. (2016). Chavas and Reed (2019) employed APEs under uniform thermal forcing and variable global dynamical forcing to test existing hypotheses regarding tropical cyclone genesis and size, whereas Merlis and Held (2019) provided a nice review of tropical cyclone simulations with APEs. Möbis and Stevens (2012) determined the factors controlling the position of the Intertropical Convergence Zone (ITCZ) on an aquaplanet. Although the Aquaplanet Experiment (APE) is predominantly tailored for atmospheric models, when integrated with a global ocean model, it sheds light on ocean-atmosphere dynamics without the influence of land-sea disparities and topographical intricacies. For instance, Donohoe et al. (2014) delved into the impact of the ocean mixed layer depth on climate using a series of slab ocean aquaplanet simulations.

The prominent test cases employed by ocean models to quantify mixing and dianeutral transport are:

(i) the lock exchange or dam break test case to measure mixing in the simplest possible configuration (D.-P. Wang (1984), Haidvogel and Beckmann (1999), Jankowski (1999), Ilıcak et al. (2012), Kärnä et al. (2013), Petersen et al. (2015), Gibson et al. (2017), Kärnä et al. (2018));

(ii) the overflow test case to investigate the impact of topography on spurious mixing (Haidvogel and Beckmann (1999), Ilıcak et al. (2012), Petersen et al. (2015));
(iii) the Dynamics of Overflow Mixing and Entrainment (DOME) test case to study the model's ability to simulate density-driven overflows (Ezer and Mellor (2004), Legg et al. (2006), Q. Wang et al. (2008), Burchard and Rennau (2008), Reckinger et al. (2015), Gibson et al. (2017), Kärnä et al. (2018));
(iv) the internal wave test case to examine spurious dianeutral mixing associated with the adjustment of an internal gravity wave in a vertically stratified fluid (Ilıcak et al. (2012), Petersen et al. (2015), Gibson et al. (2017));
(v) the three-dimensional mesoscale baroclinic eddies test case at eddy-permitting grid resolution in the presence of rotation, to measure mixing under conditions closer to a realistic high-resolution global ocean models (Ilıcak et al. (2012), Petersen et al. (2015), Gibson et al. (2017), Kärnä et al. (2018)); and
(vi) the spin-down of a global ocean climate model at non-eddying and eddy permitting grid resolutions (Ilıcak et al. (2012), Petersen et al. (2015)).

The COmmunity MODelling Ocean (COMODO) project was funded by the French National Agency for Research to benchmark and improve existing ocean models and methods, and guide their future evolution. It consisted of the following test cases:

(i) Stommel gyre test case of Hecht et al. (2000) for testing the conservation of tracers;
(ii) Adapted Smolarkeiwicz test case for testing the terrain-following coordinate;
(iii) Lock exchange test case for testing the tracer advection scheme and diapycnal mixing;
(iv) Barotropic vortex test case for testing the tracer and momentum advection schemes, and the time-stepping method;
(v) Baroclinic vortex test case for testing the tracer and momentum advection-diffusion schemes, the time-stepping method, and the vertical coordinate;
(vi) Baroclinic jet test case for testing the effective resolution, the tracer and momentum advection-diffusion schemes, the time-stepping method, and the vertical coordinate;
(vii) Thacker's bowl test case for testing the wetting and drying phenomenon, the pressure gradient term, and the vertical coordinate;
(viii) Two-dimensional vertical upwelling test case for testing the time-stepping method, the vertical coordinate, and the bottom boundary conditions;
(ix) Internal tide test case for testing the vertical coordinate, the tracer and momentum advection-diffusion schemes, and the pressure gradient term;
(x) Sea mount test case for testing the tracer and momentum advection-diffusion schemes, the lateral boundary conditions, and the current-topography interactions.

The COMODO project paved the way to the successful COMMODORE workshops on the numerical solution techniques of PDEs that govern ocean circulation from global to coastal scales.

Two simplified linear models of the stationary quasi-geostrophic equations, namely the Stommel (Stommel, 1948) and Stommel–Munk (Munk & Carrier, 1950) models, have been employed as verification tools by numerous shallow water and barotropic ocean models. The Stommel model can be used to test the ability of an ocean model to reproduce the western intensification phenomenon. The Stommel–Munk model, on the other hand, focuses on the wind-driven gyres and the Ekman spiral, and can be used to test the representation of wind-driven circulation and the response of the ocean surface layer to wind stress. Foster et al. (2013) and Kim et al. (2015) presented conforming finite-element methods of the streamfunction formulation of the stationary one-layer quasi-geostrophic equations for the study of the large scale wind-driven ocean circulation. The finite element discretization in Foster et al. (2013) employed Argyris elements, whereas Kim et al. (2015) used a B-spline basis. Rotundo et al. (2016) presented the error analysis of the method in Kim et al. (2015), and Jiang and Kim (2016) generalized the method to domains with arbitrary shaped coastal boundaries. Myers and Weaver (1995) presented a diagnostic barotropic finite-element ocean

circulation model in Cartesian and spherical coordinates, and tested it against the linear Stommel and Munk models, as well as the barotropic circulation in the North Atlantic Ocean in the presence of realistic lateral boundaries and topography. Comblen et al. (2010) considered continuous, discontinuous, as well as partially discontinuous finite element formulations for the non-conservative shallow water equations, that are second-order accurate in space. In addition to the linear and non-linear versions of the Stommel and Munk gyres, the numerical solution was benchmarked against unsteady and steady wave equations, Stokes flow, and the geostrophic equilibrium. Düben et al. (2012) studied the applicability of a new finite element in atmosphere and ocean modeling that combines a second-order continuous representation for the scalar field with a first-order discontinuous representation for the velocity field. Q. Chen and Ju (2018) proposed conservative finite-volume schemes for solving the inviscid and viscous quasi-geostrophic equations on coastal-conforming unstructured primal–dual meshes. They also performed numerical experiments with a freely evolving circular flow, and the intensified western boundary current. Beel et al. (2019) introduced a novel strong form-based meshfree collocation method to directly discretize the second-order Stommel model and the fourth-order Stommel–Munk model for the large-scale wind-driven ocean circulation simulations.

We mention the relevant limited area, coastal, and tidal test cases in the ocean modeling literature, starting with Drago and Iovenitti (2000). They introduced a three-dimensional finite-difference model for coastal oceans and evaluated its performance against various scenarios, including a wind-driven current, a wind and Coriolis force balance, an Ekman spiral, tidal circulation, tidal flood and ebb on a beach, and a coastal jet influenced by a long-shore wind. Fringer et al. (2006) discussed the fundamental hydrodynamic kernel of the Stanford Unstructured Nonhydrostatic Terrain-following Adaptive Navier–Stokes Simulator (SUNTANS), a finite-volume, unstructured-grid, nonhydrostatic, parallel, coastal-ocean solver. They tested it against a non-hydrostatic lock exchange test case, a non-hydrostatic internal seiche test case, and the generation of internal waves in the Monterey Bay region. Santilli and Scotti (2015) presented the Stratified Ocean Model with Adaptive Refinement (SOMAR), a computational framework for the evolution of non-hydrostatic, baroclinic flows encountered in regional and coastal ocean simulations. It combines the flexibility of Adaptive Mesh Refinement with a set of numerical tools specifically developed to address the high degree of anisotropy of oceanic flows and the accompanying numerical challenges. The modeling framework was applied to (1) the lock exchange test case; (2) the beam generation test case following Jalali et al. (2014) to analyze the generation of internal waves; and (3) the Dubreil–Jacotin–Long (DJL) solution, which is an exact solution of the Euler equations. Garcia et al. (2019) validated the nonhydrostatic General Curvilinear Coastal Ocean Model (GCCOM) for stratified flows against the lock exchange test case; a three dimensional internal seiche test case; and a field-scale internal wave beams test case, following the experimental setup of Vitousek and Fringer (2014). Herzfeld et al. (2011) reviewed some realistic test cases for limited area ocean modelling, including a coastal shelf model application used for down-scaling; tidal response of a gulf with one open boundary across the mouth of the gulf; and the response of a coastal region to the passage of a tropical cyclone.

Many atmosphere, ocean and climate models are equipped with test suite creation and verification infrastructure, in addition to the forward time-stepping core. For example, test cases for MPAS-Ocean (T. Ringler et al., 2013) are available in the Configuration of Model for Prediction Across Scales Setups (COMPASS) repository (Asay-Davis et al., 2024) and more recently the Polaris repository (Asay-Davis & Begeman, 2024). The test cases are often contained within a separate directory of the model itself, and tutorials for a subset of the test cases are available on the online manual e.g. MITgcm (Marshall et al., 1997), MOM (Griffies et al., 2005), SUNTANS (Fringer et al., 2006), or the README file of the Github repository of the model e.g. Oceananigans (Ramadhan et al., 2020), NEMO (Madec et al., 2023), or a Wikipedia page e.g. ROMS (Shchepetkin & McWilliams, 2005). Standardized test cases provide a method to compare the solution quality and computational speed between models,

and even between different languages and architectures. For example, Bishnu et al. (2023) uses the coastal Kelvin wave and inertia-gravity wave cases to compare Fortran-MPI against Julia-MPI on CPUs and GPUs.

1.1 Contributions of this work

The majority of test cases mentioned in the introduction of our study are primarily used for validation, rather than verification. Verification, in simplest terms, investigates 'if we are solving the equations right,' contrasting with validation, which scrutinizes 'if we are solving the right equations.' Verification is a methodical process that quantifies simulation errors, displays the convergence of the numerical solution towards established benchmarks such as analytical and manufactured solutions with refinement in space and time, and ensures software quality. In contrast, code validation delves into whether the models themselves are representations of the right equations, aiming to assess how well a model mirrors the real world from the perspective of its intended application. The core objective of validation is to instill confidence in the model's predictive capability by comparing it with observed and experimental data. As a best practice, verification should precede validation to facilitate precise assessments.

Our work with MPAS-Ocean and interactions with fellow ocean modelers has enlightened us to the dangers of overlooking essential verification steps in favor of more advanced validation exercises. For instance, bypassing proper verification can inadvertently allow subtle software bugs to slip through, that are challenging to detect later on. As an illustrative example, consider a scenario where an implementation error in the spatial discretization of the non-linear advection term in the continuity equation compromises the spatial order of accuracy of an ocean model under development. The model remains stable due to the diffusion terms in the governing equations and the inherent diffusion within the numerical scheme. It performs satisfactorily against standard validation exercises, thereby arousing no suspicion. If this ocean model's predictive capability falls short compared to a more mature model, one might contemplate enhancing specific attributes like the discretization scheme, parametrizations, topographic representation, open boundary conditions, or coupling with other Earth system model components. While some of these modifications may still be necessary, without definitive evidence, we might completely overlook the possibility of incorrect implementation of the non-linear advection term. Its cumulative effect over long simulation times is far from negligible, and rectifying it may significantly improve the model's predictive capability. This highlights the imperative of extensive verification exercises—the primary subject of this paper—before proceeding with model validation. Such meticulous scrutiny could have exposed the non-linear advection term's bug early in the model's developmental phase, thereby saving valuable time for the developers. Moreover, the creation of a verification suite, although a one-time investment, can be integrated within an automated nightly regression suite. This allows for regular examination every time a substantial modification is introduced into the model, promoting a robust and consistent development process.

In this paper, we present a verification suite of shallow water test cases consisting of the non-dispersive coastal Kelvin wave, the dispersive inertia-gravity wave, the dispersive planetary and topographic Rossby waves, the barotropic tide, and a non-linear manufactured solution specifically designed for the barotropic mode. Our primary motivation for selecting these shallow water test cases stems from their routine usage in evaluating the dynamical core of atmosphere and ocean models. Moreover, many of these models are equipped with a barotropic-baroclinic time-splitting operation. This technique advances the fast, two-dimensional, depth-independent external gravity waves explicitly with a small barotropic time step or implicitly with a large one. The residual three-dimensional subsystem, which models slower internal gravity waves and ocean currents, is advanced using a large baroclinic time step. This splitting approach substantially enhances the computational efficiency of the models, often by orders of magnitude, when compared to employing a small time step for

the full three-dimensional equations, as dictated by the CFL condition for the fastest wave. Notably, within this framework, the barotropic equations adopt the form of inhomogeneous rotating shallow water equations, with the source term represented by the barotropic average of a subset of terms within the baroclinic momentum equation. As a result, our carefully chosen shallow water test cases can also serve as verification tools for the barotropic solver integrated within these models.

A secondary, yet substantial motivation for this research is to furnish model developers with a method to critically assess their code designed to numerically solve fluid dynamics problems, such as those pertaining to the shallow water equations or the hydrostatic primitive equations. Our methodology initiates with a set of governing equations, upon which we apply spatial and temporal discretizations. We then implement this discretized formulation into the code. Our approach leverages fundamental knowledge of classical geophysical phenomena such as non-dispersive and dispersive geophysical waves, which can be modeled by the code. So, we devise straightforward test cases, beginning with linear ones, and then progressing to non-linear ones. This ensures that we accurately capture the behaviors of these geophysical phenomena. After all, correctly modeling basic problems is foundational to successful oceanic modeling, not to mention the development of general circulation models (GCMs). However, securing the correct answer using a fixed spatial grid and time step size is insufficient. It is essential to perform refinement in spatial grid size and time step to demonstrate the attainment of the appropriate convergence rate. In essence, this not only verifies that the correct solution is achieved but also assures that it is achieved for the correct underlying reasons. If the correct convergence rate is not obtained, the numerical method or its implementation may be flawed, and any successful result could be coincidental rather than systematic. Our robust set of test cases is therefore an invaluable resource for anyone engaged in the development of a GCM. At some stage in the development process, the accurate resolution of the shallow water equations is almost inevitably required. Moreover, the present work elucidates a comprehensive process for evaluating both the physical and numerical correctness of the code. Through carefully chosen examples, this paper aims to demonstrate not only the methodology but also the underlying principles, thereby contributing a vital tool for future developments in the field of ocean modeling.

Equally pivotal, and forming the third cornerstone of our paper's objectives, is its pedagogical value, particularly in enriching the curriculum of geophysical fluid dynamics courses. This work extends beyond theoretical concepts, providing a practical, hands-on approach to learning. By integrating the physical characteristics of various geophysical waves (Sections 2.5, 2.6, 2.7, and 2.8), including equatorial waves (Section A2), with their numerical simulations, this work bridges the gap between theory and practice. Students can visualize and appreciate the dynamic evolution of these waves, enhancing their understanding of these complex geophysical phenomena. Moreover, the paper equips students with the tools and knowledge to critically evaluate the accuracy of numerical ocean models, or even a basic code they develop for visualizing geophysical waves. They can verify the correctness of the discretized equations of motion implemented in these models, by ensuring that the numerical solution convergences at the expected theoretical rate based on the spatial and temporal orders of accuracy.

Among the cited literature, the seven cases of D. L. Williamson et al. (1992), the Stommel and Stommel-Munk test cases, and the COMODO barotropic vortex test case are specifically designed for shallow water equations. Only test cases (i)–(iv) of D. L. Williamson et al. (1992), the Stommel, and Stommel-Munk test cases are equipped with exact solutions. However, the exact solution of the fluid layer depth of test case (iii) and the exact solution of all the prognostic variables of test case (iv) of D. L. Williamson et al. (1992) consists of an integral which is difficult to evaluate analytically, and is computed using numerical quadrature. The exact solutions of test cases (ii) and (iii) of D. L. Williamson et al. (1992) as well as the Stommel and Stommel-Munk test cases are steady-state solutions. The remaining test cases, meant for validation rather than verification, investigate anomalous

mixing, coastal processes, etc., but not the accuracy of the barotropic solver in a split baroclinic-barotropic time stepping scheme. To properly test the accuracy of the barotropic solver, the existence of analytical time-dependent solutions is crucial. They serve as a benchmark, towards which the numerical solutions are expected to converge, when refined simultaneously in both space and time. The creation of our test cases arose from these practical needs during the development and improvement of MPAS-Ocean. Although the exact solutions of some of these test cases are provided in standard geophysical fluid dynamics textbooks e.g. Cushman-Roisin and Beckers (2011), this work contributes to the development of a standard verification suite by providing specific details of the initial and boundary conditions, error plots, and rates of convergence, that will be useful for comparison with other ocean models.

The structure of this paper is organized as follows: Section 2 provides the essential theoretical foundation on the shallow water equations and offers a concise overview of the test cases, which encompass geophysical waves, barotropic tide, and a non-linear manufactured solution. In Section 3, we discuss the spatial and temporal discretizations applied to the prognostic equations. Our study employs two types of spatial discretizations: (1) a mimetic finite volume based on the TRiSK scheme and used in MPAS-Ocean; and (2) a high-order Discontinuous Galerkin Spectral Element Method implemented in the Spectral Element Library in Fortran (SELF). The prognostic equations are advanced using a variety of time-stepping methods. Section 6 presents the numerical results, including time evolution of the error as well as convergence plots with refinement in both space and time, only in space, and only in time. Conclusions are drawn in Section 7. Appendix A outlines an additional suite of shallow water test cases with exact solutions, consisting of a plane wave, diffusion, advection-diffusion, a moving shock, as well as non-dispersive and dispersive equatorial waves. Appendix B underscores the relevance of the shallow water test cases in the context of baroclinic-barotropic splitting in oceanic models, illustrating how the barotropic equations align with the form of inhomogeneous rotating shallow water equations. Finally, Appendix C delves into nuanced aspects of the numerical implementation, including the specification of initial and boundary conditions on hexagonal meshes, and the interpolation of the numerical solution or the error to the coarsest mesh for refinement only in space.

2 A Verification Suite of Shallow Water Test Cases

We have developed a verification suite for shallow water cases, starting with linear test cases before advancing to non-linear ones. With each test case, we incrementally introduce a new layer of complexity, enabling us to verify the implementation of every term in the equations governing barotropic motion and the shallow water core in ocean models. The linear test cases, consisting of the linear geophysical waves and the barotropic tide, are tailored to verify the pressure gradient, Coriolis, and linearized advection terms. Conversely, the non-linear test cases, encompassing the non-linear planetary and topographic Rossby waves, along with the manufactured solution, prove instrumental for examining the non-linear advection terms. The source term in the manufactured solutions can exemplify the barotropic average of the baroclinic terms found on the right-hand side of the barotropic equations.

Although lacking exact solutions, we have incorporated the Rossby waves into our verification suite for several compelling reasons. First, these comprehensive test cases, in their non-linear form, verify the implementation of each and every term in the non-linear shallow water equations. Second, they feature non-trivial variations in the meridional gradient of the Coriolis parameter and the bottom topography (Section 2.4). Third, Rossby wave test cases illustrate that exact solutions are not a prerequisite for verifying the model's spatial and temporal orders of accuracy. This can be achieved by plotting the norm of the differences between numerical solutions over successive pairs of spatial and temporal resolutions, refined at a constant ratio, instead of the actual error norm (Section 4.5).

Finally, these test cases significantly contribute to the educational aspect of our research (Section 1.1).

Building on the rationale for including Rossby waves in our verification suite, it is important to clarify that the second reason does not diminish the value of test cases with exact solutions. In fact, the actual error norm of the numerical solution, defined only for these test cases, converges under the simultaneous spatial and temporal refinement (Section 4.3). Additionally, it is worth noting that for certain test cases and specific resolution ranges, the norm of differences between numerical solutions over a pair of spatial or temporal resolution, may be minimal and susceptible to overshadowing by round-off errors. This scenario underscores the need for additional test cases, preferably those with exact solutions, to ensure comprehensive verification (Section 6.1, bullet point 10).

Before delving into detailed descriptions of the various test cases, we provide a brief theoretical overview of equations representing shallow water and barotropic flows.

2.1 The Shallow Water Equations

The non-linear rotating shallow water equations, representing the shallow water core of ocean models, can be expressed compactly as

$$\boldsymbol{u}_t + \boldsymbol{u}\cdot\nabla\boldsymbol{u} + f\boldsymbol{k}\times\boldsymbol{u} = -g\nabla(h+b) + \nu\nabla^2\boldsymbol{u}, \tag{1a}$$

$$h_t + \nabla\cdot(h\boldsymbol{u}) = 0, \tag{1b}$$

where $\boldsymbol{u}(x,y,t) = u(x,y,t)\boldsymbol{i} + v(x,y,t)\boldsymbol{j}$ is the velocity vector, $h(x,y,t)$ is the shallow water layer thickness above the bottom topography $b(x,y)$ originating at $z=0$, $\eta(x,y,t)$ is the surface elevation, f is the Coriolis parameter, g is the acceleration due to gravity, and ν is the horizontal viscosity. The subscripts denote partial differentiation, and $\boldsymbol{i}$, $\boldsymbol{j}$, and $\boldsymbol{k}$ are the unit vectors in the x, y and z directions. If H represents the mean depth of the fluid at rest, then the surface elevation $\eta(x,y,t)$ at any point in time satisfies

$$\eta(x,y,t) = h(x,y,t) + b(x,y) - H, \tag{2}$$

Using (2) and replacing the non-linear advection term in (1a) with the right-hand side of the vector identity

$$\boldsymbol{u}\cdot\nabla\boldsymbol{u} = (\nabla\times\boldsymbol{u})\times\boldsymbol{u} + \nabla\frac{|\boldsymbol{u}|^2}{2} = \{\boldsymbol{k}\cdot(\nabla\times\boldsymbol{u})\}\boldsymbol{k}\times\boldsymbol{u} + \nabla\frac{|\boldsymbol{u}|^2}{2}, \tag{3}$$

we obtain the vector-invariant form of the momentum equation

$$\boldsymbol{u}_t + \nabla K + (\zeta+f)\boldsymbol{u}^\perp = -g\nabla\eta + \nu\nabla^2\boldsymbol{u}. \tag{4}$$

Here $\boldsymbol{u}^\perp = \boldsymbol{k}\times\boldsymbol{u}$, $K = |\boldsymbol{u}|^2/2$ is the kinetic energy, and $\zeta = \boldsymbol{k}\cdot(\nabla\times\boldsymbol{u})$ is the relative vorticity.

2.2 The Barotropic Equations

The barotropic equations of an ocean model can be expressed in vector-invariant form

$$\overline{\boldsymbol{u}}_t + f\overline{\boldsymbol{u}}^\perp = -g\nabla\eta + \nu\nabla^2\overline{\boldsymbol{u}} + \overline{\boldsymbol{G}}, \tag{5a}$$

$$\eta_t + \nabla\cdot(h_{\text{total}}\overline{\boldsymbol{u}}) = 0, \tag{5b}$$

where $h_{\text{total}} = \sum_{k=1}^{N} h_k$ is the total depth equivalent to the sum of individual layer thicknesses h_k, $\overline{\boldsymbol{u}} = \left(\sum_{k=1}^{N} h_k\boldsymbol{u}\right)/h_{\text{total}}$ is the barotropic velocity, and $\overline{\boldsymbol{G}}$ is the barotropic average of specific baroclinic terms. Typically, the diffusion term $\nu\nabla^2\overline{\boldsymbol{u}}$ is encapsulated within $\overline{\boldsymbol{G}}$, and it does not explicitly feature in the barotropic momentum equation (5a), except in some variants such as Blumberg and Mellor (1987). A comprehensive demonstration

of the barotropic-baroclinic splitting procedure, alongside a derivation of the barotropic equations of motion using MPAS-Ocean as a case study, can be found in Appendix B. In an analytical comparison against the shallow water equations (1), it becomes evident that the barotropic equations (5) essentially mirror the form of (1), albeit with some key differences: the exclusion of the non-linear advection term and the introduction of the source term $\overline{\boldsymbol{G}}$ in the momentum equation, and the substitution of the shallow water velocity and layer thickness by the barotropic velocity $\overline{\boldsymbol{u}}$ and the total depth h_{total} respectively.

The shallow water and barotropic equations can be succinctly expressed as the following set of equations:

$$u_t + \underbrace{\nabla K}_{(1)} + \underbrace{\zeta \boldsymbol{u}^{\perp}}_{(2)} + \underbrace{f_0 \boldsymbol{u}^{\perp}}_{(3)} + \underbrace{\beta_0 y \boldsymbol{u}^{\perp}}_{(4)} = -\underbrace{g \nabla \eta}_{(5)} + \underbrace{\nu \nabla^2 \boldsymbol{u}}_{(6)} + \underbrace{\overline{\boldsymbol{G}}}_{(7)}, \tag{6a}$$

$$\eta_t + \underbrace{\nabla \cdot (H \boldsymbol{u})}_{(8)} + \underbrace{\nabla \cdot (\eta \boldsymbol{u})}_{(9)} - \underbrace{\nabla \cdot (b \boldsymbol{u})}_{(10)} = 0, \tag{6b}$$

where the Coriolis parameter f has been decomposed into its leading-order components: f_0, the base Coriolis parameter at a reference latitude, and $\beta_0 y$, where β_0 is the meridional gradient of f. The non-linear advection term in the continuity equation has been split into three parts using (2). Each term in (6), excluding the temporal derivatives, is labeled for convenient referencing in test cases that verify its numerical implementation.

2.3 Shallow Water Equations in Cartesian Coordinates

The inviscid rotating shallow water equations in Cartesian coordinates are

$$u_t + uu_x + vu_y - fv = -g(h+b)_x, \tag{7a}$$

$$v_t + uv_x + vv_y + fu = -g(h+b)_y, \tag{7b}$$

$$h_t + (hu)_x + (hv)_y = 0. \tag{7c}$$

Inserting (2) into (7), we obtain

$$u_t + uu_x + vu_y - fv = -g\eta_x, \tag{8a}$$

$$v_t + uv_x + vv_y + fu = -g\eta_y, \tag{8b}$$

$$\eta_t + (hu)_x + (hv)_y = 0. \tag{8c}$$

The geophysical waves consisting of the coastal Kelvin wave, the inertia-gravity wave, and the planetary and topographic Rossby waves are solutions to the linearized rotating inviscid shallow water equations, obtained by dropping the non-linear terms in (8) as

$$u_t - fv = -g\eta_x, \tag{9a}$$

$$v_t + fu = -g\eta_y, \tag{9b}$$

$$\eta_t + \{(H-b)u\}_x + \{(H-b)v\}_y = 0. \tag{9c}$$

In the case of a flat bottom, $b(x,y) = 0$, $h(x,y,t) = H + \eta(x,y,t)$, and (9) reduces to

$$u_t - fv = -g\eta_x, \tag{10a}$$

$$v_t + fu = -g\eta_y, \tag{10b}$$

$$\eta_t + H\,(u_x + v_y) = 0. \tag{10c}$$

In the subsequent subsections, we review the exact solutions associated with the various test cases, which we have numbered 1–6 for convenient reference. The derivations of these exact solutions, particularly for some of the geophysical wave test cases, can be found in standard textbooks on geophysical fluid dynamics (GFD), such as those by Vallis (2017), Cushman-Roisin and Beckers (2011), Pedlosky (1987), and Gill (2016).

2.4 Summary of Shallow Water Test Cases

The test cases presented in the following sections, summarized in Table 1, assess the numerical implementation of various terms within the rotating shallow water equations. Each of them incorporates the Coriolis force, which imparts rotation to the shallow water. The Coriolis term is constant, rendering the domain of motion to be an *f-plane* for all but the planetary Rossby wave test case, where the Coriolis term is a linear function of y and the domain of wave motion is a *beta-plane*. The topographic Rossby wave test case uniquely features a sloping bottom as a linear function of y, while others possess a flat bottom. With the meridional gradient of the Coriolis parameter and the bottom topography being non-trivial for the planetary and the topographic Rossby waves respectively, the shallow water systems for these solutions are variable-coefficient. In contrast, the systems for other test cases remain constant-coefficient. The non-linear planetary and topographic Rossby waves, along with the manufactured solution test case verify the implementation of the non-linear advection terms. In fact, the non-linear Rossby wave test cases check every term in the non-linear homogeneous shallow water equations. On the other hand, the coastal Kelvin wave, inertia-gravity wave, linear Rossby waves, and the barotropic tide are solutions to the linearized form of these equations, thus their governing PDEs are stripped of non-linear terms. Table 1 concisely captures the assumptions underpinning the geophysical waves, the barotropic tide, and the non-linear manufactured solution. This table details the nature of the simplified PDEs for the shallow water equations, applied boundary conditions, and the specific terms from (6) that are tested. In the context of convergence studies, where extensive simulation times are unnecessary, the diffusion terms for the non-linear Rossby wave test cases are discretionary and are denoted with an asterisk.

Table 1. Summary of assumptions for the geophysical waves, barotropic tide, and non-linear manufactured solution, detailing the nature of the corresponding simplified PDEs for the shallow water equations, their applied boundary conditions, and the specific terms tested from (6), with optional ones indicated by an asterisk.

	Coriolis Parameter	**Bottom Topography**	**Numerical PDE**	**Boundary Conditions**	**Terms Verified in Equation** (6)
1. Coastal Kelvin Wave	Constant (*f-plane*)	Flat Bottom	Linear, Homogeneous, Constant-Coefficient	Non-Periodic in x Periodic in y	(3), (5), (8)
2. Inertia-Gravity Wave	Constant (*f-plane*)	Flat Bottom	Linear, Homogeneous, Constant-Coefficient	Periodic in x Periodic in y	(3), (5), (8)
3a. Planetary Rossby Wave	Linear in y (*beta-plane*)	Flat Bottom	Linear, Homogeneous, Variable-Coefficient	Radiation or No-Normal Flow	(3), (4), (5), (8)
3b. Planetary Rossby Wave (NL)	Linear in y (*beta-plane*)	Flat Bottom	**Non-Linear**, Homogeneous, Variable-Coefficient	Radiation or No-Normal Flow	(1), (2), (3), (4), (5), (6)*, (8), (9)
4a. Topographic Rossby Wave	Constant (*f-plane*)	Linear in y, Sloping Bottom	Linear, Homogeneous, Variable-Coefficient	Radiation or No-Normal Flow	(3), (5) (8), (10)
4b. Topographic Rossby Wave (NL)	Constant (*f-plane*)	Linear in y, Sloping Bottom	**Non-Linear**, Homogeneous, Variable-Coefficient	Radiation or No-Normal Flow	(1), (2), (3), (5), (6)*, (8), (9), (10)
5. Barotropic Tide	Constant (*f-plane*)	Flat Bottom	Linear, Homogeneous, Constant-Coefficient	Non-Periodic in x, Non-Periodic in y	(3), (5) (8)
6. Manufactured Solution	Constant (*f-plane*)	Flat Bottom	Non-Linear, Inhomogeneous, Constant-Coefficient	Periodic in x, Periodic in y	(1), (2), (3), (5), (7), (8), (9)

2.5 Test Case 1: Coastal Kelvin Wave

A Kelvin wave is a lateral disturbance that requires the presence of a topographic boundary e.g. the oceanic coast or a waveguide e.g. the equator. As the name implies, the coastal Kelvin wave belongs to the topographic boundary category and is therefore a

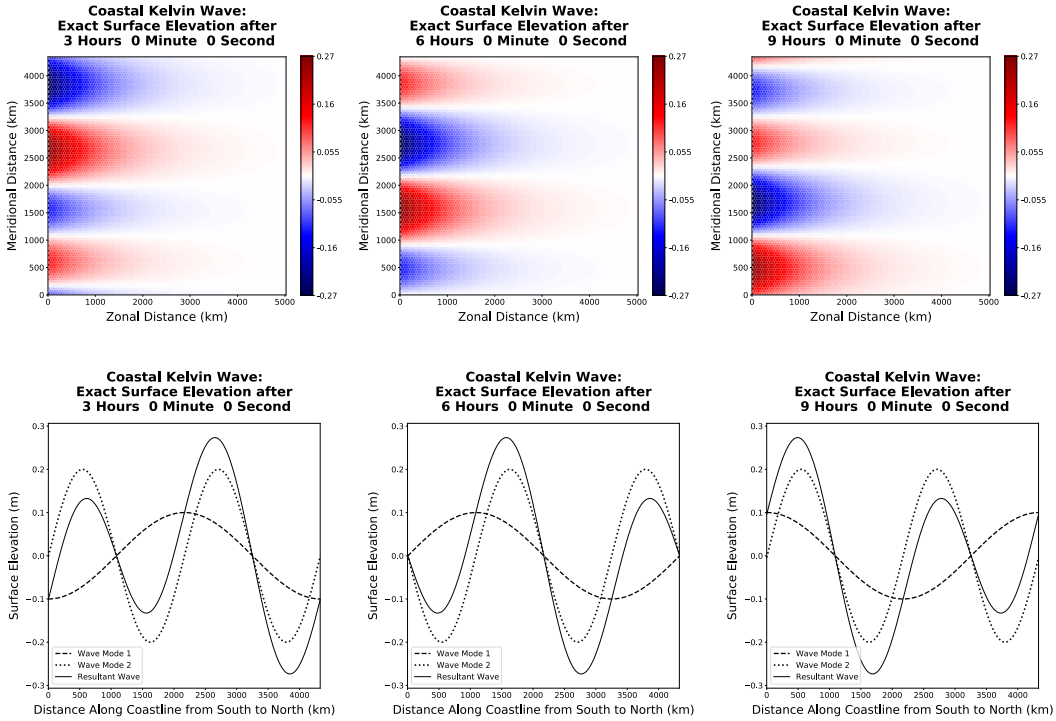

Figure 1. Time evolution of the exact surface elevation of TC1, the non-dispersive coastal Kelvin wave, in the entire domain (first row), and along the coastline (second row), with dashed and dotted lines representing component wave modes, and the solid line representing the resultant wave.

common phenomenon along coastlines. It travels with the coast on its right in the Northern Hemiphere and with the coast on its left in the Southern Hemisphere. Its amplitude decreases exponentially away from the coast with a decay scale equal to the barotropic Rossby radius of deformation. This is why the coastal Kelvin wave appears to be 'trapped' near the coast. It is non-dispersive which causes the coastal Kelvin wave to preserve its initial profile as it propagates in the alongshore direction over time.

Following the derivation in Cushman-Roisin and Beckers (2011), if the coastline is aligned along the y-axis ($x = 0$) and we specify $u = 0$ throughout the domain, we arrive at the physically feasible general solution

$$u = 0, \tag{11}$$

$$v = \sqrt{gH}F(y + ct)e^{-x/R}, \tag{12}$$

$$\eta = -HF(y + ct)e^{-x/R}. \tag{13}$$

Here $R = c/f = \sqrt{gH}/f$ is the barotropic Rossby radius of deformation, a length scale where rotational effects are considered important. From (12) and (13), we observe that R is also a measure of the trapping distance of the Kelvin wave from the coast. The dispersion relation of a coastal Kelvin wave mode with angular frequency ω and meridional wavenumber k_y is $\omega = ck_y$, where the wave speed $c = \sqrt{gH}$ is independent of k_y, a characteristic of non-dispersive waves.

In our numerical simulations, we choose a sinusoidal meridional profile defined by $F(y) = \hat{\eta}\sin(k_y y)$. In addition, we designate the exact solution to be a superposition of two wave modes, with the second mode having twice the amplitude and wavenumber components compared to the first, i.e., $\hat{\eta}^{(2)} = 2\hat{\eta}^{(1)}$ and $k_y^{(2)} = 2k_y^{(1)}$. Here, $\hat{\eta}^{(1)} = 10^{-4}$

m, $k_y^{(1)} = 2\pi/L_y$, and L_y denotes the meridional extent of the domain. For this test case and subsequent ones, we set $f_0 = 10^{-4}$ s^{-1}, $g = 10$ m s^{-2} and $H = 10^3$ m, yielding $c = \sqrt{gH} = 100$ m s^{-1} and $R = c/f_0 = 10^6$ m. As elaborated in Section 2.7, f_0 is identical to the Coriolis parameter f on an *f-plane*, but corresponds to its leading-order component on a *beta-plane*. The zonal extent is specified as $L_x = 5R = 5 \times 10^6$ m, ensuring the wave amplitude diminishes to virtually zero just west of the open eastern boundary. For all test cases, the meridional extent is set as $L_y = \sqrt{3}/2 L_x$ when modeled with the TRiSK-based finite volume method, and as $L_y = L_x$ when discretized with the discontinuous Galerkin spectral element method (DGSEM). Figure 1 presents the temporal evolution of the exact surface elevation of the coastal Kelvin wave. The first row illustrates the surface elevation throughout the entire domain, while the second row depicts the surface elevation along the coastline. Here, dashed and dotted lines denote the component wave modes, with the solid line indicating the resultant wave. Both component wave modes propagate at identical phase speeds, a fact that can be confirmed by tracking the crest or trough of the first wave mode and one crest or trough of the second wave mode, and observing that their relative positions do not vary over time. This phenomenon leads to the maintenance of the original resultant profile without distortion, a characteristic anticipated for a non-dispersive wave.

2.6 Test Case 2: Inertia-Gravity Wave

As discussed in Cushman-Roisin and Beckers (2011), by eliminating the requirement of a lateral boundary and the constraint $u = 0$, we can assume a Fourier series solution to (10) of the form

$$\begin{bmatrix} \eta \\ u \\ v \end{bmatrix} = \mathrm{Re}\left\{ \begin{bmatrix} \hat{\eta} \\ \hat{u} \\ \hat{v} \end{bmatrix} e^{i(k_x x + k_y y - \omega t)} \right\}, \tag{14}$$

and arrive at the dispersion relation

$$\omega \left\{ \omega^2 - \left(c^2 k^2 + f^2 \right) \right\} = 0, \tag{15}$$

where $k = \sqrt{k_x^2 + k_y^2}$. The root $\omega = 0$ corresponds to the steady geostrophic state and the remaining two roots $\omega = \pm\hat{\omega}$, where $\hat{\omega} = \sqrt{c^2 k^2 + f^2}$, correspond to oppositely-travelling inertia-gravity waves with super-inertial frequency ($\omega > f$). Since the zonal and meridional phase speeds, given by $c_x = \omega/k_x$ and $c_y = \omega/k_y$, are functions of the wavenumber components k_x and k_y, the inertia-gravity wave is dispersive. To arrive at a particular solution consisting of only the inertia-gravity wave mode $\hat{\omega}$, we replace ω by $\hat{\omega}$ and insert (14) in (10), which results in

$$-i\hat{\omega}\hat{u} - f\hat{v} = -ik_x g\hat{\eta}, \tag{16a}$$

$$-i\hat{\omega}\hat{v} + f\hat{u} = -ik_y g\hat{\eta}, \tag{16b}$$

$$-i\hat{\omega}\hat{\eta} + iH\left(k_x\hat{u} + k_y\hat{v}\right) = 0. \tag{16c}$$

We can now solve any two equations of (16) to obtain

$$\hat{u} = \frac{g\hat{\eta}}{\hat{\omega}^2 - f^2}\left(\hat{\omega}k_x + ifk_y\right), \tag{17}$$

$$\hat{v} = \frac{g\hat{\eta}}{\hat{\omega}^2 - f^2}\left(\hat{\omega}k_y - ifk_x\right), \tag{18}$$

and demonstrate that these values of $\hat{u}$ and $\hat{v}$ satisfy the third equation as well. Therefore, the particular solution consisting of only the inertia-gravity wave mode $\hat{\omega}$ is

$$\eta = \mathrm{Re}\left\{\hat{\eta} e^{i(k_x x + k_y y - \hat{\omega} t)}\right\}, \tag{19}$$

$$u = \mathrm{Re}\left\{\frac{g\hat{\eta}}{\hat{\omega}^2 - f^2}\left(\hat{\omega}k_x + ifk_y\right) e^{i(k_x x + k_y y - \hat{\omega} t)}\right\}, \tag{20}$$

$$v = \mathrm{Re}\left\{\frac{g\hat{\eta}}{\hat{\omega}^2 - f^2}\left(\hat{\omega}k_y - ifk_x\right) e^{i(k_x x + k_y y - \hat{\omega} t)}\right\}, \tag{21}$$

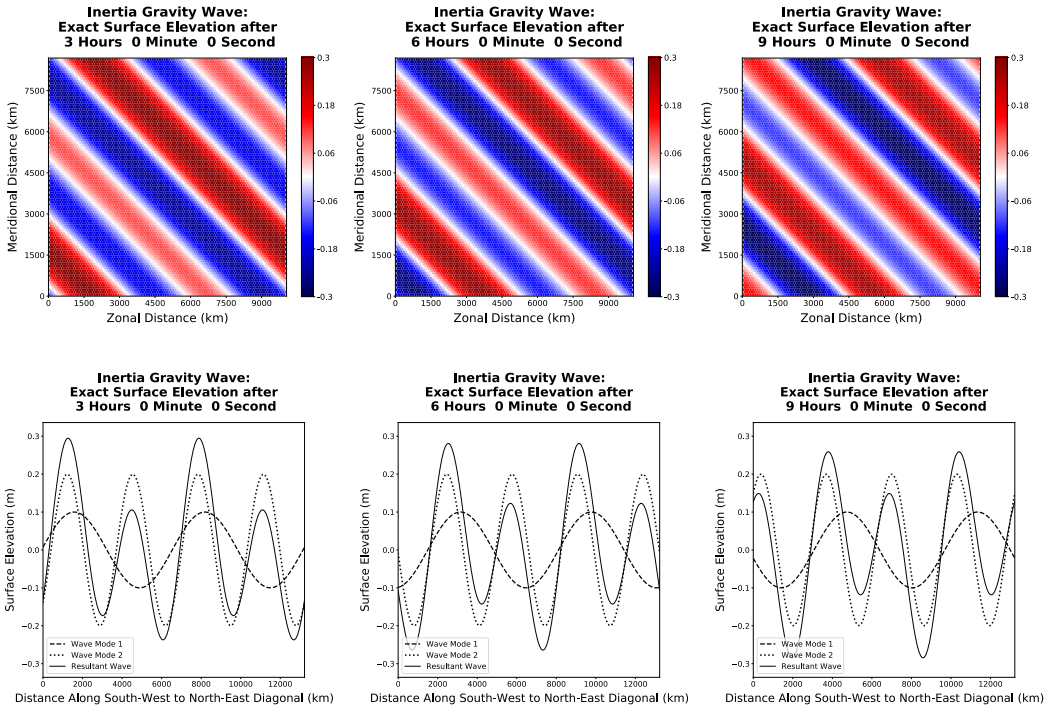

Figure 2. Same as Figure 1, but for TC2, the high-frequency dispersive inertia-gravity wave, with the second row depicting the time evolution of the exact surface elevation and its component wave modes (represented by solid, dashed, and dotted lines respectively) along the south-west to north-east diagonal of the domain.

which simplifies to

$$\eta = \hat{\eta}\cos(k_x x + k_y y - \hat{\omega}t), \tag{22}$$

$$u = \frac{g\hat{\eta}}{\hat{\omega}^2 - f^2}\left\{\hat{\omega}k_x\cos(k_x x + k_y y - \hat{\omega}t) - fk_y\sin(k_x x + k_y y - \hat{\omega}t)\right\}, \tag{23}$$

$$v = \frac{g\hat{\eta}}{\hat{\omega}^2 - f^2}\left\{\hat{\omega}k_y\cos(k_x x + k_y y - \hat{\omega}t) + fk_x\sin(k_x x + k_y y - \hat{\omega}t)\right\}. \tag{24}$$

We once again specify the exact solution in our numerical simulations to be the sum of two wave modes, whose amplitudes and wavenumbers satisfy $\hat{\eta}^{(2)} = 2\hat{\eta}^{(1)}$, $k_x^{(2)} = 2k_x^{(1)}$, and $k_y^{(2)} = 2k_y^{(1)}$, where $\hat{\eta}^{(1)} = 0.1$ m, $L_x = 10^7$ m, $k_x^{(1)} = 2\pi/L_x$, and $k_y^{(1)} = 2\pi/L_y$. The domain extents L_x and L_y are chosen carefully to ensure that the ratio f/ck ranges between 0.5 and 1.0 for these wave modes, so that both the gravity and the rotational forces play important roles in their generation. The first row of Figure 2 exhibits the surface elevation in the entire domain, and the second row depicts the surface elevation along the south-west to north-east diagonal. With the phase speed now being a function of the wavenumber, the component wave modes represented by dashed and dotted lines propagate at different phase speeds (as manifested by the temporal variation in the relative position of the crest or trough of the first wave mode with respect to a crest or trough of the second wave mode). This leads to modification of the resultant wave profile (represented by a solid line) with time, a characteristic that aligns with the behavior of a dispersive wave.

2.7 Test Case 3: Planetary Rossby Wave

Planetary Rossby waves are low-frequency dispersive waves that feel the rotation of the Earth. They owe their existence to the variation of the Coriolis parameter $f = 2\Omega \sin\theta$ with the latitude θ, where Ω denotes Earth's rotational rate. A Taylor expansion of f around a reference latitude θ_0, limited to the first two terms, results in $f = f_0 + \beta_0 y$. Here, $f_0 = 2\Omega \sin\theta_0$, $\beta_0 = 2(\Omega/a)\cos\theta_0$, and a represents Earth's radius. A geophysical wave motion's domain is termed a *beta-plane* if the β term is included, and an *f-plane* if not. The *beta-plane* approximation is applicable when $\beta_0 y \ll f_0$ across the domain, implying $\beta = \beta_0 L \ll f_0$, where L indicates the meridional extent of the domain and β is a dimensionless planetary number. For Earth's mid-latitudes, typical values are $f_0 \approx 10^{-4}$ s^{-1} and $\beta_0 \approx 2 \times 10^{-11}$ m^{-1} s^{-1}, which we adopt in our numerical simulations as well.

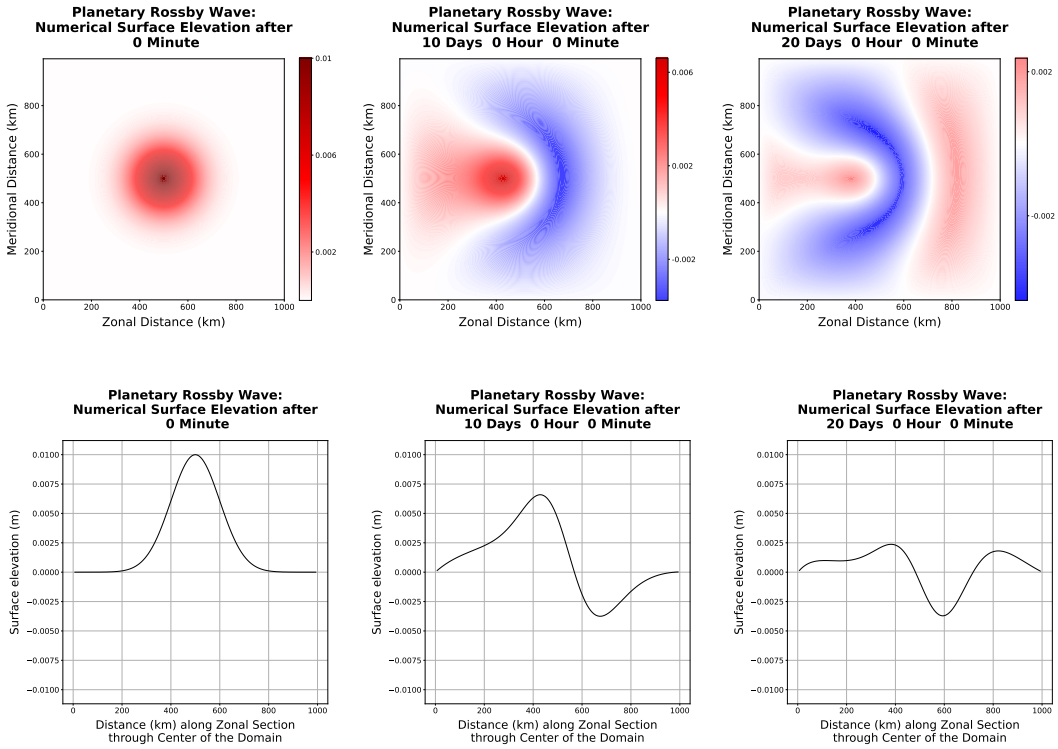

Figure 3. Time evolution of the numerical surface elevation of TC3, the low-frequency dispersive planetary Rossby wave, in the entire domain (first row) and along the zonal section through the domain center (second row), advanced with Williamson's low-storage third-order Runge-Kutta time-stepping method, and spatially discretized with DGSEM using 10 elements and polynomial basis functions of order 7 in each horizontal direction.

Planetary Rossby waves represent a slow evolution of steady geostrophic flows, with the velocity field consisting of a leading-order geostrophic term and an ageostropic perturbation term. Following the derivation in Cushman-Roisin and Beckers (2011), if the velocities are approximated solely by the geostrophic terms and inserted into the momentum equations, a first-order velocity approximation is obtained. Applying these velocities to the continuity equation (10c) yields a constant-coefficient equation, the Fourier series solution of which results in the dispersion relation

$$\omega = -\frac{\beta_0 R^2 k_x}{1 + R^2\left(k_x^2 + k_y^2\right)}. \tag{25}$$

For shorter waves, where the length scale $L(\sim 1/k_x \sim 1/k_y) \lesssim R$, we find $\omega \sim \beta_0 L$. Longer waves, with $L(\sim 1/k_x \sim 1/k_y) \gtrsim R$, yield $\omega \sim \beta_0 R^2/L \lesssim \beta_0 L$. In both cases, under the assumption $\beta_0 L \ll f_0$, we obtain $\omega \ll f_0$, affirming the subinertial nature of the planetary Rossby wave. The zonal and meridional phase speeds, represented by $c_x = \omega/k_x$ and $c_y = \omega/k_y$, are clearly functions of the wavenumber components k_x and k_y, thereby attributing to the wave's dispersive nature. Moreover, the zonal phase speed is invariably negative, with higher potential vorticity on the right of the propagation direction, resulting in a phase propagation in westward, northwestward, or southwestward directions.

Our attempt to simulate the planetary Rossby wave using the shallow water equations presents a unique challenge. Since the shallow water equations admit a spectrum of wave solutions, it is impossible to only extract the low-frequency planetary Rossby waves as a numerical solution. To simulate the low-frequency planetary Rossby waves, we numerically solve the linear but variable-coefficient shallow water equations on a *beta-plane*. We specify the initial surface elevation as a Gaussian blob at the center of the domain, and obtain the initial velocities using the pressure gradient force and geostrophic balance:

$$\eta(x, y, t = 0) = \hat{\eta} e^{-\{(x-x_0)^2/(2R_x^2) + (y-y_0)^2/(2R_y^2)\}}, \tag{26}$$

$$u(x, y, t = 0) = \frac{g}{f_0 R_y^2}(y - y_0)\hat{\eta} e^{-\{(x-x_0)^2/(2R_x^2) + (y-y_0)^2/(2R_y^2)\}}, \tag{27}$$

$$v(x, y, t = 0) = -\frac{g}{f_0 R_x^2}(x - x_0)\hat{\eta} e^{-\{(x-x_0)^2/(2R_x^2) + (y-y_0)^2/(2R_y^2)\}}. \tag{28}$$

Here $\hat{\eta} = 0.01$ m represents the surface elevation amplitude, (x_0, y_0) represents the center of the domain with zonal extent $L_x = 10^6$ m, and the decay scales R_x and R_y amount to 10% of the zonal and meridional extents of the domain. Time integration results in the evolution of this 'geostrophic' monopole on the *beta-plane*. Since we are not equipped with the time-dependent exact solutions, we demonstrate high-resolution numerical solutions in Figure 3 obtained using (a) a high-order discontinuous Galerkin spectral element method (DGSEM) in space with 10 elements and polynomial basis functions of order 7 in each horizontal direction, resulting in seventh-order spatial accuracy, and (b) the low-storage third-order Runge-Kutta method of J. Williamson (1980) in time. The first row illustrates the time evolution of the numerical surface elevation in the entire domain, and the second row depicts the same along the zonal section through the domain center. Right after initialization, some gravity waves radiate out of the monopole towards the domain boundaries. We impose radiation boundary conditions by setting the external state to a motionless fluid with no free surface height variation ($u = v = 0$, $\eta = 0$), leading to the eventual propagation of the gravity waves out of the domain. Alternatively, if solid wall or no-normal flow boundary conditions were applied, these gravity waves would continue propagating along the domain boundaries as coastal Kelvin waves. On a much slower time scale on the order of the diurnal motion of the Earth, we observe the monopole itself propagating in the direction of the planetary Rossby waves, with increasing potential vorticity to the right of the propagation direction. The monopole can be considered to be a superposition of infinite wave modes with different wavelengths, each of which propagates according to the dispersion relation (25). Due to the dispersive nature of the planetary Rossby wave, the wave modes with different wavelengths propagate with different phase speeds, resulting in a distortion of the initial Gaussian profile of the monopole with time (as observed in the plots of Figure 3).

The non-linear advection terms can also be turned on, along with appropriate diffusion terms to ensure a stable solution over prolonged simulation times. It is worth mentioning that the inclusion of non-linear and diffusion terms verifies the implementation of every term in the non-linear homogeneous shallow water equations. While we present the numerical solution for the linear version of the planetary Rossby wave test case, the non-linear solutions have also been thoroughly examined. In our convergence analyses, aimed at verifying the spatial and temporal orders of accuracy, both the linear and non-linear versions of the

planetary Rossby wave were solved. As extensive simulation times are not required for these convergence studies, the activation of diffusion terms is optional for this purpose.

2.8 Test Case 4: Topographic Rossby Wave

The topographic Rossby wave arises because of variations of the bottom topography. Following the derivation in Cushman-Roisin and Beckers (2011), we only consider a bottom topography with a small slope of constant magnitude in the meridional direction. If α_0 denotes the bottom slope, the topography is $b(x, y) = -\alpha_0 y$. Using (2), the thickness of the shallow water layer at any point in time is

$$h(x, y, t) = H + \eta(x, y, t) - b(x, y) = H + \alpha_0 y + \eta(x, y, t). \tag{29}$$

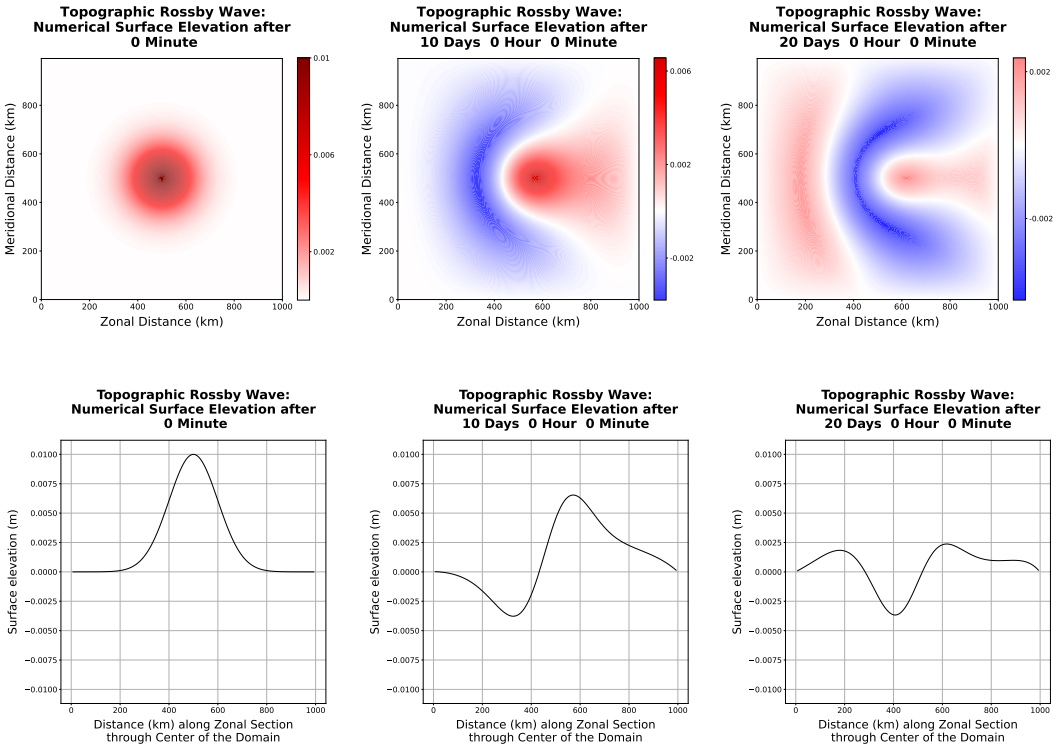

Figure 4. Same as Figure 3, but for TC4, the topographic Rossby wave.

The requirement of a gentle bottom slope implies $\alpha = \alpha_0 L/H \ll 1$, where α is a dimensionless parameter similar to the planetary number, and L is the horizontal length scale of motion. Just like the planetary Rossby waves, the velocity field of their topographic analogues consist of a leading-order geostrophic term, and a much smaller ageostrophic correction term. The ageostrophic terms, driving the motion of these waves, are $\mathcal{O}(\alpha)$ relative to the geostrophic ones, resulting in subinertial wave frequencies $\omega \sim \alpha f \ll f$.

Again, assuming the velocities to consist entirely of the geostrophic terms and inserting them into the momentum equations, we arrive at a first-order approximation of the velocities, which upon insertion into the continuity equation results in a constant-coefficient equation, the Fourier series solution of which results in the dispersion relation

$$\omega = \frac{\alpha_0 g k_x}{f\left\{1 + R^2\left(k_x^2 + k_y^2\right)\right\}}. \tag{30}$$

The zonal and meridional phase speeds, given by $c_x = \omega/k_x$ and $c_y = \omega/k_y$, depend on the wavenumber, rendering the topographic Rossby waves dispersive. Since c_x has the same sign as $\alpha_0 f$, in the northern hemisphere (where $f > 0$), the topographic Rossby waves propagate with the shallower side on their right. Similar to planetary Rossby waves, the potential vorticity increases towards the right of the direction of the zonal phase propagation.

Figure 4 illustrates high-resolution numerical solutions for the topographic Rossby wave, modeled using DGSEM and RK3. The horizontal domain extents, the spatial and temporal resolutions, as well as the initial and boundary conditions have been configured to match their counterparts for the planetary Rossby wave test case (Section 2.7). The bottom slope is chosen to be $\alpha_0 = \beta_0 H_0/f_0$, with $\beta_0 = 2 \times 10^{-11}$ m^{-1} s^{-1}, $f_0 = 10^{-4}$ s^{-1} and $H_0 = 1000$ m. As a result, the depth increases northward, and the different modes of the dispersive topographic Rossby wave, each associated with a unique wavenumber, exhibit the same phase speeds as their planetary analogues, though they travel in the opposite direction, i.e., eastward. Due to the variation of phase speed with wavenumber, the initial profile is no longer maintained, as evidenced by the plots in Figure 4. Just like the planetary Rossby wave test case, our presentation focuses on the linear solution. However, we have also explored the non-linear solution, which effectively tests every term in the homogeneous non-linear shallow water equations. During our convergence studies, we address both variants of the topographic Rossby wave.

2.9 Test Case 5: Barotropic Tide

Following the analysis of barotropic tides in Clarke and Battisti (1981) and Clarke (1991), we consider a simple model of the continental shelf, with constant depth h from the coast at $x = 0$ to the edge of the shelf at $x = L$, where the depth abruptly increases to H and remains so in the deep sea. By combining equations (10a), (10b) and (10c), we arrive at the single equation

$$\nabla^2 \eta_t - \frac{1}{c^2}\left(\eta_{ttt} + f^2 \eta_t\right) = 0, \tag{31}$$

for modeling sinusoidal barotropic tides with $c^2 = gh$ on the continental shelf and $c^2 = gH$ on the coast. Assuming the continental shelf is long and straight, and applying scaling analysis and no-normal flow boundary condition at the coast, we arrive at the complete solution

$$\eta = \hat{\eta}\cos(kx)\cos(\omega t), \tag{32}$$

$$u = \frac{\hat{\eta} g \omega k}{\omega^2 - f_0^2}\sin(kx)\sin(\omega t), \tag{33}$$

$$v = \frac{\hat{\eta} g f_0 k}{\omega^2 - f_0^2}\sin(kx)\cos(\omega t), \tag{34}$$

where $\omega = \sqrt{ghk^2 + f_0^2}$. Rewriting (32) as

$$\eta = \frac{1}{2}\hat{\eta}\cos(kx - \omega t) + \frac{1}{2}\hat{\eta}\cos(kx + \omega t), \tag{35}$$

we can interpret the surface elevation as the sum of two waves perpendicular to the coast but travelling in opposite directions. Tidal resonance occurs when the ratio of coastal to deep sea level is infinite, i.e. when

$$\frac{\eta(0)}{\eta(L)} = \frac{1}{\cos(kL)} = \pm\infty, \tag{36}$$

which occurs when

$$L = \left(m + \frac{1}{2}\right)\frac{\pi}{k} = \left(m + \frac{1}{2}\right)\pi\sqrt{\frac{gh}{\omega^2 - f^2}}, \tag{37}$$

for a non-negative integer m.

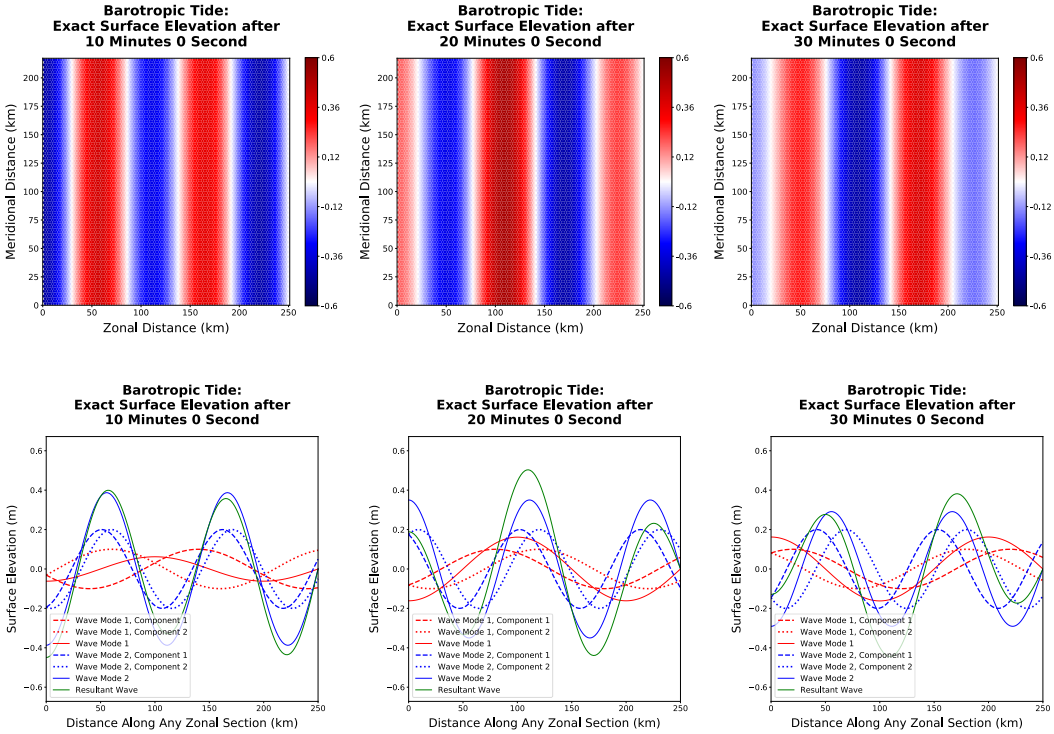

Figure 5. Time evolution of the exact surface elevation of TC5, the barotropic tide, in the entire domain (first row), and along any zonal section (second row).

Figure 5 depicts the time evolution of the barotropic tide in the entire domain (first row) with zonal extent $L_x = 2.5 \times 10^5$ m, and along any zonal section (second row). The exact surface elevation is chosen to be a superposition of two standing wave modes, each of which is the sum of two wave modes of equal amplitude and phase speed but traveling in opposite directions. Each of these component modes is uniform in the meridional direction. Their wavelengths, $\lambda^{(1)} = 2\pi/k^{(1)}$ and $\lambda^{(2)} = 2\pi/k^{(2)}$, amount to 4/5-th and 4/9-th of the zonal extents of the domain, which satisfy the conditions for tidal resonance. The surface elevation amplitudes are designated as $\hat{\eta}^{(1)} = 0.2$ m and $\hat{\eta}^{(2)} = 2\hat{\eta}^{(1)}$. The second row of Figure 5 shows the resultant barotropic tide as a solid green line, while its underlying standing wave modes are indicated by solid red and blue lines. The individual components of each standing wave mode are represented by dashed and dotted lines of the same color.

2.10 Test Case 6: Non-linear Manufactured Solution

The method of manufactured solutions (MMS) has been applied to a wide variety of scientific and engineering codes involving the numerical solution of linear and non-linear PDEs. MMS can be used to generate PDEs with exact solutions so that the order of accuracy of numerical methods can be investigated. The basic idea of MMS is to choose such an exact solution, $u = u_e$, and insert it in the left-hand side of the governing PDE $\mathcal{L}(u) = 0$, where u represents the dependent variable. This gives rise to a source term $f = \mathcal{L}(u_e)$, which is only a function of space and time, and the coefficients appearing in the PDE. The modified PDE $\mathcal{L}(u) = f$ is then discretized as $\mathcal{L}_\Delta(u_\Delta) = f_\Delta$, and solved to obtain the numerical solution u_Δ, where the subscript Δ represents the set of discretization parameters.

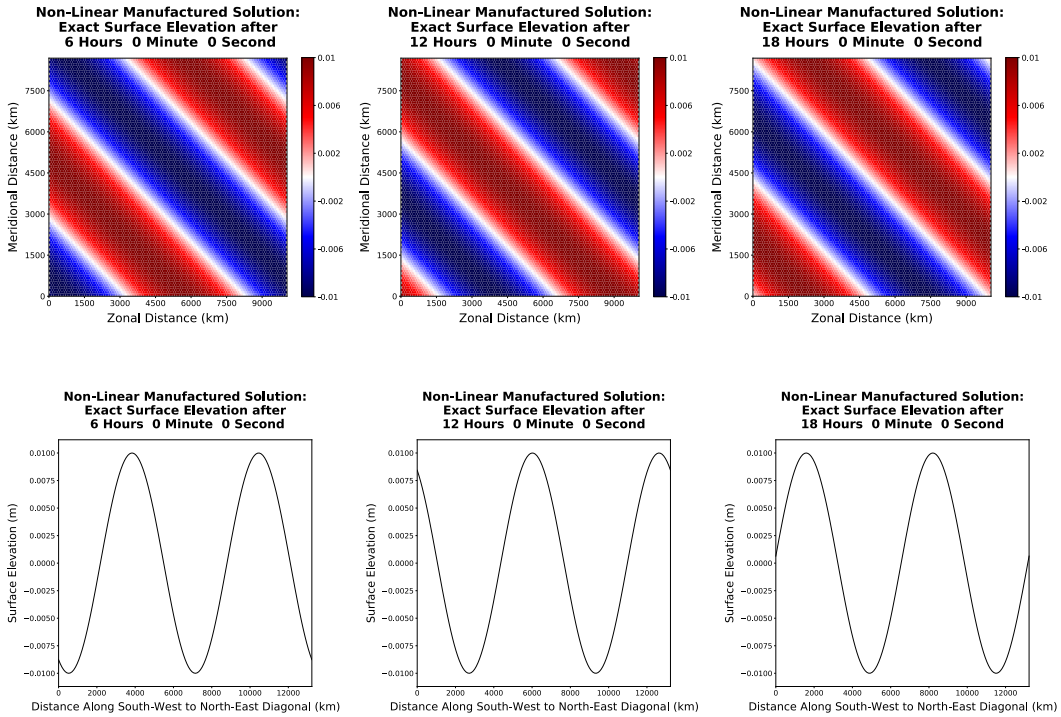

Figure 6. Same as Figure 5, but for TC6, the non-linear manufactured solution, with the second row depicting the time evolution of the exact surface elevation along the south-west to north-east diagonal of the domain.

Detailed investigations of MMS against benchmark solutions with sufficiently complex structure were conducted by Salari and Knupp (2000) and Roache (2002). Within the geophysical literature, test case (iv) of D. L. Williamson et al. (1992) belongs to the category of MMS. More recently, Kärnä et al. (2018) presented a steady-state baroclinic manufactured solution in one vertical and one horizontal dimension. In contrast, we propose a time-dependent barotropic manufactured solution in the horizontal plane,

$$u = \hat{\eta}\cos(k_x x + k_y y - \omega t), \tag{38a}$$
$$v = 0, \tag{38b}$$
$$\eta = \hat{\eta}\sin(k_x x + k_y y - \omega t), \tag{38c}$$

which solves the non-linear rotating inviscid shallow water equations

$$u_t + uu_x + vu_y - fv = -g\eta_x + s^u, \tag{39a}$$
$$v_t + uv_x + vv_y + fu = -g\eta_y + s^v, \tag{39b}$$
$$\eta_t + \{(H+\eta)u\}_x + \{(H+\eta)v\}_y = s^\eta. \tag{39c}$$

Inserting the exact solution (38) into the left-hand side of (39), we obtain the source terms

$$s^u = \hat{\eta}\left\{(-f + gk_x)\cos\phi + \omega\sin\phi - \hat{\eta}(k_x + k_y)\sin(2\phi)/2\right\}, \tag{40a}$$
$$s^v = \hat{\eta}\left\{(f + gk_y)\cos\phi + \omega\sin\phi - \hat{\eta}(k_x + k_y)\sin(2\phi)/2\right\}, \tag{40b}$$
$$s^\eta = \hat{\eta}\left\{-H(k_x + k_y)\sin\phi - \omega\cos\phi + \hat{\eta}(k_x + k_y)\cos(2\phi)\right\}, \tag{40c}$$

where the phase $\phi = k_x x + k_y y - \omega t$. As expected, the source terms undergo modification if the governing equations being discretized assume a different form. For instance, if we employ

the discontinuous Galerkin Spectral Element Method (DGSEM), outlined in Section 3.2, for spatial discretization, one option is to start out with the conservative form of the non-linear rotating shallow water equations. The conservative form can be obtained by adding the depth-multiplied momentum equations (7a) and (7b) to the continuity equation (7c). The resulting equations are

$$(hu)_t + (hu^2 + gh^2/2)_x + (huv)_y - fhv = -ghb_x, \tag{41a}$$
$$(hv)_t + (huv)_x + (hv^2 + gh^2/2)_y + fhu = -ghb_y, \tag{41b}$$
$$h_t + (hu)_x + (hv)_y = 0. \tag{41c}$$

The source terms transition to

$$\begin{aligned} s^{hu} &= \hat{\eta} H \left\{ (gk_x - f)\cos\phi + \omega \sin\phi \right\} \\ &\quad + \hat{\eta}^2 \left[\sin(2\phi) \left\{ -H(k_x + k_y) + (gk_x - f)/2 \right\} - \omega \cos(2\phi) \right] \\ &\quad + \hat{\eta}^3 (k_x + k_y) \left\{ -\sin(2\phi)\sin\phi + \cos^3\phi \right\}, \end{aligned} \tag{42a}$$
$$\begin{aligned} s^{hv} &= \hat{\eta} H \left\{ (gk_y + f)\cos\phi + \omega \sin\phi \right\} \\ &\quad + \hat{\eta}^2 \left[\sin(2\phi) \left\{ -H(k_x + k_y) + (gk_y + f)/2 \right\} - \omega \cos(2\phi) \right] \\ &\quad + \hat{\eta}^3 (k_x + k_y) \left\{ -\sin(2\phi)\sin\phi + \cos^3\phi \right\}, \end{aligned} \tag{42b}$$
$$s^h = \hat{\eta} \left\{ -H(k_x + k_y)\sin\phi - \omega\cos\phi + \hat{\eta}(k_x + k_y)\cos(2\phi) \right\}, \tag{42c}$$

where the water depth is simplified to $h(x, y, t) = H + \eta(x, y)$, and the right-hand side of (41a) and (41b) is reduced to zero due to the presence of a flat bottom ($b = 0$). Figure 6 depicts the time evolution of the manufactured solution across the entire domain (first row) and along the south-west to north-east diagonal (second row). The relevant parameters are $L_x = 10^7$ m and $\hat{\eta} = 0.01$ m. The wavenumbers are defined by $k_x = 2\pi/L_x$ and $k_y = 2\pi/L_y$. The angular frequency is $\omega = c\sqrt{k_x^2 + k_y^2}$, with $c = \sqrt{gH} = 100\ \mathrm{m\ s^{-1}}$ representing the speed of shallow water gravity waves.

While we have utilized (38) to 'manufacture' our solution for this non-linear test case, any smooth solution in space and time can serve the purpose, provided that the source terms are accurately defined. For instance, the exact solutions of the coastal Kelvin wave, inertia-gravity wave, and the barotropic tide, which solve the linearized homogeneous form of (39), can be employed to 'manufacture' our solution and verify the implementation of non-linear terms. In these cases, the source terms are essentially the non-linear terms of (39) computed with the exact solutions, and can be expressed as:

$$s^u = \left[uu_x + vu_y \right]_{\text{exact}}, \tag{43a}$$
$$s^v = \left[uv_x + vv_y \right]_{\text{exact}}, \tag{43b}$$
$$s^\eta = \left[(\eta u)_x + (\eta v)_y \right]_{\text{exact}}. \tag{43c}$$

3 Spatial and Temporal Discretizations

To generate the numerical solutions, we have developed a rotating shallow water solver in an object-oriented Python environment (Bishnu, 2024a). This tool employs two forms of spatial discretizations: first, a mimetic finite volume method based on the TRiSK framework (Thuburn et al., 2009; T. D. Ringler et al., 2010), and second, a high-order discontinuous Galerkin spectral element method (DGSEM). The primary motivation for selecting these two spatial discretization methods originates from their widespread application in operational ocean models. These models generally adopt

(a) finite volume methods (LeVeque, 2002; Eymard et al., 2003; Versteeg & Malalasekera, 2007; Patankar, 2018); or
(b) finite element (Zienkiewicz et al., 2005; Bathe, 2006; Hughes, 2012; D. L. Logan, 2022) or spectral element (Patera, 1984; Maday & Patera, 1989; Karniadakis & Sherwin, 2005; D. A. Kopriva, 2009) methods.

Finite volume methods (FVMs) serve as a highly efficient method for solving PDEs. By partitioning the computational domain into a finite set of control volumes, FVMs approximate the integral form of the governing equations over these volumes. This method's distinct advantage lies in its conservation of quantities of interest, making it a preferred choice for problems bound by conservation laws, typical in fields such as fluid dynamics and heat transfer. Many ocean models like Oceananigans (Ramadhan et al., 2020), MITgcm (Marshall et al., 1997), MOM (Griffies et al., 2005), ROMS (Shchepetkin & McWilliams, 2005), NEMO (Madec et al., 2023), FVCOM (C. Chen et al., 2006), and MPAS-Ocean (T. Ringler et al., 2013) utilize FVMs for spatial discretization.

The finite element method (FEM), on the other hand, offers a versatile solution to tackle complex problems, often formulated as PDEs in engineering and mathematical physics. The computational domain, divided into a mesh of simpler elements (like 2D triangles or 3D tetrahedra), forms the foundation of FEM. The methodology hinges on computing approximate solutions at the element nodes, thereby minimizing an associated error function. This results in highly accurate solutions within the approximations' constraints, making FEM particularly useful for problems involving structural analysis, heat transfer, fluid flow, mass transport, and electromagnetic fields.

A specialized class of the FEMs is the spectral element method (SEM), discussed in detail in Section 3.2. In contrast to the classical FEMs that predominantly use low, fixed order polynomials (typically linear or quadratic) as basis functions, SEMs leverage the flexibility of adjustable polynomial order, enabling exponential convergence rates in smooth problems. SEMs, typically using quadrilateral (2D) or hexahedral (3D) elements, are adept at managing complex geometries. The numerical solution derived using SEM parallels those produced by FEM, facilitating comparable methods for conducting convergence studies and interpreting the resulting plots. This is especially true if the underpinning method is a discontinuous Galerkin (DG) method (Hesthaven & Warburton, 2007). The DG method allows for the solution to be discontinuous between elements, thereby making it particularly effective for problems characterized by sharp gradients or shocks, as encountered in fluid dynamics or electromagnetism. Software based on SEM showcases excellent compatibility with GPU-accelerated hardware, a technology that is now dominant in the world's fastest supercomputers (Strohmaier & Dongarra, 2023). Therefore, we anticipate a surge in the development of high-order methods like SEMs in research software in the years to come. Currently, among functional ocean models, FESOM (Danilov et al., 2004; Q. Wang et al., 2014) and NUMO (Kopera et al., 2018, 2023) employ FEM and SEM respectively for spatial discretization.

We discuss in subsequent sections a few key considerations depending on the spatial discretization technique in use. For instance, in Section 6, we explore the significance of conducting self-refinement convergence tests only in space and only in time, the underlying reasons for which may vary between FVMs and SEMs. Moreover, we delve into numerical implementation details in Appendix C, some of which are pertinent to FVMs and some to SEMs. Regardless of these disparities, we demonstrate the robustness of our numerical recipe in verifying the spatial and temporal orders of accuracy across both types of spatial discretization.

We now provide a brief description of the TRiSK-based FVM and DGSEM used in our numerical experiments.

3.1 TRiSK-Based Mimetic Finite Volume Method

The mimetic finite volume spatial discretization based on the TRiSK scheme was first proposed by Thuburn et al. (2009) to ensure that geostropic modes remain stationary and Coriolis terms remain energy conserving on arbitrarily structured C-grids. It was then generalized by T. D. Ringler et al. (2010) to model the non-linear rotating shallow water equations while guaranteeing the evolution of mass, velocity, and potential vorticity in a

consistent and compatible manner, and the conservation of total energy within the time truncation error. This mimetic finite volume method was chosen to horizontally discretize the primitive equations of MPAS-Ocean while invoking the hydrostatic, incompressible, and Boussinesq approximations on a staggered C-grid. Even though the grid cells of MPAS-Ocean are near hexagons consisting of five or more sides, the MPAS framework supports cells with any number of sides with the algorithm and code remaining identical for cells of all shapes and sizes. Since this horizontal discretization guarantees conservation of mass, potential vorticity, and energy, it makes MPAS-Ocean a suitable candidate to simulate mesoscale eddies.

The spatial domain is assumed to be tessellated by two meshes, a primal mesh and a dual mesh. Each corner of a primary mesh cell is uniquely associated with a center of a dual mesh cell and vice versa. For a regular hexagonal mesh, each corner of a primary mesh cell coincides with a vertex of a dual mesh cell and vice versa. A line segment connecting two primal mesh cell centers is uniquely associated with a line segment connecting two dual mesh cell centers. In case of a regular hexagonal mesh, these two line segments are perpendicular bisectors of each other. In case of an irregular hexagonal mesh, these two line segments can still intersect orthogonally, but not necessarily at their midpoints. As mentioned before, the two prognostic variables for the rotating shallow water equations are the surface elevation, η, defined at the primal cell centers, and the normal velocity $\boldsymbol{u}_e$ defined at the primal cell edges. The divergence of a two-dimensional vector quantity is defined at the position of η, while the two-dimensional gradient of a scalar quantity is defined at the position of $\boldsymbol{u}_e$ and oriented along its direction. The curl of a vector quantity is defined at the vertices of the primal cells. Finally, the tangential velocity $\boldsymbol{u}_e^{\perp}$ along a primal cell edge is computed diagnostically using a flux mapping operator from primal to dual mesh, which essentially takes a weighted average of the normal velocities on the edges of the cells sharing that edge. Interested readers may refer to Thuburn et al. (2009) and T. D. Ringler et al. (2010) for an extensive discussion on the mesh specifications, the elements of the discrete system along with their positioning and their connectivities, and the formulation of the discrete spatial and flux-mapping operators.

3.2 Discontinuous Galerkin Spectral Element Method

Spectral element methods belong to the category of multidomain spectral methods. In spectral element methods, the physical domain is divided into smaller, non-overlapping elements, as illustrated in Figure 7. Within each element, functions are approximated by Lagrange interpolating polynomials. The interpolation knots are Gauss-type Quadrature, often Legendre-Gauss or Legendre-Gauss-Lobatto (D. A. Kopriva, 2009; D. Kopriva & Gassner, 2010; Gassner et al., 2016). Each element is mapped to a reference element, and the mapping and metric terms are also approximated by Lagrange interpolation.

With Discontinuous Galerkin Spectral Element Methods, the weak form of the equations are solved within each element. As explained in standard finite and spectral element textbooks like Donea and Huerta (2003), Hughes (2012), Zienkiewicz et al. (2005), Bathe (2006), Reddy (2019), D. L. Logan (2022), Karniadakis and Sherwin (2005), Canuto et al. (2007b), and D. A. Kopriva (2009), the weak form is obtained by multiplying the original "strong form" of the PDE by a test function and then integrating over the domain. In this context, a test function is a mathematical tool that facilitates the derivation of the weak form of the PDE. This weak form requires the solution to be differentiable to a lower order compared to the strong form, and is generally easier to solve numerically. The test function is chosen to have certain properties, such as being zero on the boundaries of the domain or being part of a certain function space. Integration by parts is subsequently applied to the product of the PDE and the test function to reduce the order of the derivatives. This process transitions the problem into an integral representation wherein the solution satisfies the PDE in an averaged "weak" sense rather than at every single point, as mandated by the strong form. In case of DGSEM, the test functions are specified as each of the Lagrange

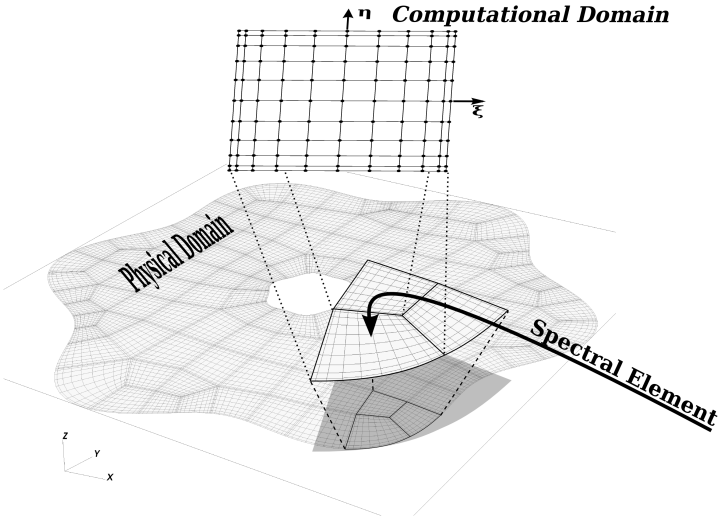

Figure 7. Depiction of a physical domain divided into elements that are then each mapped to a reference computational element. Within each element, solution variables and the coordinate mapping are approximated by Lagrange interpolating polynomials.

interpolating polynomials. Additionally, continuous integrals in the weak formulation are replaced by discrete quadrature. For computational efficiency, the quadrature points are chosen to match the interpolation points which also provides spectral accuracy. To couple neighboring elements, approximate Riemann solvers are used to exchange properties, such as mass and momentum. For hyperbolic systems, like the shallow water equations, the Riemann solver is chosen to be consistent with the underlying equations while also providing dissipation to stabilize the numerical method (Gassner et al., 2016; Ranocha, 2016). To exchange momentum and mass fluxes between neighboring elements and approximate the numerical flux at the element boundaries, we employ the upwind local Lax-Friedrichs Riemann solver of Rusanov (1961).

DGSEM allows for spatial refinement through two distinct approaches: increasing the polynomial order while keeping the number of elements constant, known as p-refinement, or alternatively, increasing the number of elements with a constant polynomial order, termed h-refinement. In Section 6.2, the leading order error terms of DGSEM are employed to illustrate how p-refinement achieves exponential convergence, while h-refinement effectively captures the spatial order of accuracy.

For the linear test cases, the weak form of the linear constant- or variable-coefficient shallow water equations (9c) is solved in Cartesian coordinates. However, for non-linear test cases, including the manufactured solution, and the non-linear planetary and topographic Rossby waves, we start with the conservative form (41) of the non-linear shallow water equations (7), and then solve the weak form of these equations.

3.3 Time-Stepping Methods

We advance the numerical solution using the following set of time-stepping methods:

List 1. *Standard predictor-corrector and multistep time-stepping methods*

RK2: explicit midpoint method, belonging to the second-order Runge-Kutta family
RK3: low-storage third-order Runge-Kutta method of J. Williamson (1980)
RK4: low-storage fourth-order Runge-Kutta method of Carpenter and Kennedy (1994)

AB2: second-order Adams-Bashforth method
AB3: third-order Adams-Bashforth method
AB4: fourth-order Adams-Bashforth method

List 2. *Time-stepping methods popular in ocean modeling*

FB: forward-backward or Implicit Euler method
LF_TR: leapfrog trapezoidal method
LF_AM3: leapfrog Adams-Moulton method
FB_RK2: forward-backward method with RK2 feedback
GenFB_AB2–AM3: generalized forward-backward method with AB2–AM3 step
GenFB_AB3–AM4: generalized forward-backward method with AB3–AM4 step

Shchepetkin and McWilliams (2005) perform a detailed stability analysis of each of the time-stepping methods of List 2. The parameters of all of these methods can be optimized to attain a specific order of accuracy, maximize the stability range, and minimize the magnitude of the local truncation error. By considering all variations of these parameters discussed in Shchepetkin and McWilliams (2005), the total number of time-stepping methods of List 2 exceeds 20. Even though we have tested the numerical solution against all of these methods, we present the convergence plots for only the methods of List 1.

4 A Primer on Truncation Error and Order of Accuracy

We furnish the necessary background on truncation error and how it is related to the numerical solution's spatial and temporal orders of accuracy. We consider situations where the orders of accuracy of the local truncation error and the global error agree, as encountered in a wide variety of computational physics domains including atmosphere and ocean models.

When solving PDEs, especially in the context of physics and engineering, it is often impossible or highly impractical to obtain an analytical solution. Instead, numerical methods are employed, and this involves discretizing the domain of the problem, i.e., breaking it down into small discrete segments or elements. The process of discretization inherently introduces approximations, primarily due to the omission of higher-order derivative terms, culminating in truncation errors. For time-dependent PDEs that model transient phenomena, like the unsteady heat conduction or fluid flow, both spatial and temporal discretizations are used, resulting in truncation errors associated with both space and time approximations. As the simulation progresses, these errors accumulate, leading to an increasingly pronounced divergence between the numerical and exact solutions.

The order of accuracy of the truncation error corresponds to the rate at which this error diminishes relative to the size of the discretization. A higher order signifies a more rapid shrinkage of error with finer discretization. For example, a second-order accurate method in space anticipates an error reduction by n^2 for every refinement of the spatial grid by a factor of n.

Truncation errors play a pivotal role in determining the accuracy of a numerical solution. Striking the right balance is essential: one must pick a method or grid resolution that offers adequate accuracy without overburdening computational resources. While refining the grid often curtails truncation errors, it simultaneously escalates the computational demands and may exacerbate other anomalies, such as round-off errors. In the world of numerical PDE solutions, a deep comprehension of truncation errors, their origins, and their ramifications is indispensable. This knowledge guides the choice of optimal methods, grid scales, and bolsters confidence in the accuracy of derived solutions.

4.1 Truncation Error, Consistency, Stability, and Convergence

The local truncation error, τ, is the residual after substituting the exact solution into the difference equation, obtained by discretizing the original differential equation. For time-marching or initial value problems involving ordinary differential equations (ODEs), hyperbolic and parabolic PDEs, some textbooks define the local truncation error as the error incurred in a single time step Δt starting with the exact solution at the beginning of the time step. If $\hat{\tau}$ represents the local truncation error based on this definition, it is straightforward to demonstrate that $\tau = \hat{\tau}/\Delta t$ (Bishnu, 2021).

A numerical method is called consistent if the local truncation error, τ, over a single time step, reduces to zero with the refinement of the spatial and temporal grids, sometimes under additional constraints. Mathematically,

$$\lim_{\Delta \to 0} \tau = \lim_{\Delta \to 0} \frac{\hat{\tau}}{\Delta t} = 0, \tag{44}$$

where Δ represents the set of discretization parameters for the spatial and temporal grids.

Numerical stability in the context of solving time-marching ODEs and PDEs involves analyzing how various types of errors—those from initial conditions, boundary conditions, round-off errors, and notably discretization or truncation errors—propagate in space and time as the numerical method is employed. In the realm of ODEs, the stability of a method largely depends on the chosen time step size, with the objective being to prevent errors from growing exponentially or becoming unbounded as time progresses. This concept extends to PDEs as well, but with an added layer of complexity. Here, stability is influenced not just by the time step size, but also by its relationship with spatial step sizes. This relationship is often scrutinized using the Courant-Friedrichs-Lewy (CFL) condition, a crucial criterion in the stability analysis of numerical methods for hyperbolic PDEs. The Von Neumann stability analysis emerges as another pivotal technique, particularly adept at determining the stability of numerical schemes applied to linear PDEs. By assessing the growth of Fourier modes in the numerical solution, this method provides a deeper understanding of how errors might amplify over iterations. The stability of a numerical method is crucial to ensure that the computed solution remains reliable and bounded over time. An unstable method can lead to solutions that diverge dramatically from the exact solution, even if the method is consistent, rendering the numerical approach ineffective for practical applications.

The numerical solution is said to converge to the exact solution if the global truncation error, or simply the global error, $\hat{\tau}_G$, defined as the difference between the exact and numerical solutions at a time horizon, reduces to zero with the refinement of the spatial and temporal grids. If the time horizon is specified as $T = n\Delta t$, $\hat{\tau}_G$ encapsulates the cumulative effect of $\hat{\tau}$ over n time steps. For a broad spectrum of numerically stable methods, barring exceptions like superconvergent and subconvergent ones (Levine, 1985; Ferreira & Grigorieff, 1998; Barbeiro et al., 2005), $\hat{\tau}_G$ is typically one order of Δt smaller than $\hat{\tau}$ and of the same order of accuracy as τ. So, if (44) holds for a stable numerical scheme, it is indicative of convergence. This concept aligns with the first half of the Lax Equivalence Theorem (Lax & Richtmyer, 1956), asserting that a consistent finite difference method for a linear initial value problem converges if and only if it is stable. For numerical methods such as finite volume, finite and spectral element methods, the Lax Equivalence Theorem does not directly apply in its classical form, as these methods have different formulations compared to finite difference methods. However, the underlying principles of consistency, stability, and convergence are still crucial in these methods.

4.2 Truncation Error of Hyperbolic and Parabolic PDEs

In Bishnu (2021), we determined the full expression for the local truncation error of numerical solutions of hyperbolic and parabolic PDEs advanced with Method of Lines time integrators. These integrators are characterized by their separate treatment of space and

time discretizations: they initially discretize the spatial variables to reduce the PDE to a system of ODEs, which are then solved using standard ODE integration techniques. By employing theoretical analysis and symbolic algebra computations, we obtained exact expressions for the coefficients of the generic local truncation error

$$\tau = \mathcal{O}\left(\Delta x^{\alpha}\right) + \Delta t \mathcal{O}\left(\Delta x^{\alpha}\right) + \Delta t^{2} \mathcal{O}\left(\Delta x^{\alpha}\right) + \cdots + \Delta t^{\beta-1} \mathcal{O}\left(\Delta x^{\alpha}\right) + \mathcal{O}\left(\Delta t^{\beta}\right), \tag{45}$$

where Δx and Δt denote the cell width and time step size, and α and β represent the spatial and temporal orders of accuracy. The right-hand side of (45) is applicable not only to the numerical solution of hyperbolic and parabolic PDEs in one spatial dimension, but also extends to higher-dimensional cases, provided a uniform grid is employed. This is exemplified in Section 6.2, where, in the context of a two-dimensional hexagonal mesh, the two primary grid scales are identified: the distance Δx between adjacent cell centers, and the side length Δy of a hexagonal cell. In a uniform hexagonal mesh, Δx and Δy remain constant, and exhibit a proportional relationship, which paves the way for the local truncation error to assume the form (45).

The derivation of (45) is replete with mathematical complexities. While we forgo a detailed breakdown here, interested readers can refer to Bishnu (2021) which provides thorough explanations and numerous illustrative examples. Nevertheless, we will touch upon the core rationale behind this specific form of the local truncation error. Delving into the steps of any Method of Lines time integrator, we note that time derivatives or tendency terms are evaluated either at fractional time steps in the case of predictor-corrector methods or at prior time levels for multistep methods. For an ODE (or a PDE with no spatial discretization error), these tendencies are exact. However, for a general PDE, these tendencies accrue spatial discretization errors of $\mathcal{O}\left(\Delta x^{\alpha}\right)$, which manifest as coefficients of the various powers of Δt.

The coefficients of Δx^{α} in the terms $\Delta t \mathcal{O}\left(\Delta x^{\alpha}\right)$, $\Delta t^{2} \mathcal{O}\left(\Delta x^{\alpha}\right)$, …, $\Delta t^{\beta-1} \mathcal{O}\left(\Delta x^{\alpha}\right)$ of (45) contain higher order spatial derivatives of the solution, coefficients of the PDE and source terms (Bishnu, 2021). Consequently, the terms $\Delta t^{k} \mathcal{O}\left(\Delta x^{\alpha}\right)$ for $k = 1, 2, \ldots, \beta - 1$ are typically much smaller in magnitude compared to the first and last terms of (45), assuming forms $\mathcal{O}\left(\Delta x^{\alpha}\right)$ and $\mathcal{O}\left(\Delta t^{\beta}\right)$, and representing the leading-order spatial and temporal discretization errors. This disparity enables us to succinctly approximate (45) as

$$\tau = \mathcal{O}\left(\Delta x^{\alpha}\right) + \mathcal{O}\left(\Delta t^{\beta}\right). \tag{46}$$

It is worth emphasizing that (45) and (46) hold true for a broad spectrum of hyperbolic or parabolic PDEs, irrespective of whether they are linear or non-linear. This applicability spans various spatial discretizations and time-stepping techniques within the Method of Lines framework. To bring these theoretical assertions to life, we undertook convergence studies on both linear and non-linear advection equations, as well as diffusion equations, detailed in Bishnu (2021). These studies employed finite difference and finite volume spatial discretizations, coupled with predictor-corrector and multistep time-stepping methods. In the present paper, we solidify our findings, showcasing convergence plots for linear and non-linear shallow water test cases using the TRiSK-based mimetic finite volume and high-order discontinuous Galerkin spectral element methods.

4.3 Convergence at Constant Ratio of Time Step to Cell Width

Assume that our numerical scheme is stable, and the global error, $\hat{\tau}_G$, is of the same order of accuracy as the local truncation error, τ, conforming to the form (46). Then a simultaneous refinement in space and time, maintaining a constant ratio of $\gamma = \Delta t / \Delta x$, simplifies the global error to

$$\hat{\tau}_G = \mathcal{O}\left(\Delta x^{\alpha}\right) + \mathcal{O}\left(\gamma^{\beta} \Delta x^{\beta}\right) = \mathcal{O}\left(\Delta x^{\alpha}\right) + \mathcal{O}\left(\Delta x^{\beta}\right) \approx \mathcal{O}\left(\Delta x^{\min(\alpha,\beta)}\right), \tag{47}$$

in the asymptotic regime, where the error is dominated by the larger of Δx^α and Δt^β, rather than their coefficients. Given a spatial discretization of order α, the asymptotic convergence rate clearly cannot exceed α. To attain this convergence rate, we need a time-stepping method of order β such that $\beta \geq \alpha$. For optimal computational efficiency within a given family of time-stepping methods, the preferred choice would be $\beta = \alpha$.

4.4 Refinement Only in Space or Only in Time

If refinement is performed only in space while employing a stable numerical scheme, convergence of the global error cannot be guaranteed due to the presence of the $\mathcal{O}\left(\Delta t^\beta\right)$ term. A similar situation arises with refinement only in time, where the $\mathcal{O}\left(\Delta x^\alpha\right)$ term acts as an impediment to the convergence of the global error. In other words, under only spatial or temporal refinement, the local truncation error does not necessarily reduce to zero. As a result, our numerical solution may not even be consistent. In such situations, in light of the Lax Equivalence Theorem (Lax & Richtmyer, 1956), convergence becomes impossible.

4.5 Verification of the Spatial or Temporal Order of Accuracy

While asymptotic convergence may not be achievable with only spatial or temporal refinement, we can still verify the spatial and temporal orders of accuracy. For refinement only in space at constant Δt, the global error at a specific time horizon and a spatial location x_j can be expressed as

$$\left(\hat{\tau}_G\right)_j = \mathcal{O}\left(\Delta x^\alpha\right) + \mathcal{O}\left(\Delta t^\beta\right) = \zeta \Delta x^\alpha + \zeta_{\beta+1} \Delta t^\beta, \tag{48}$$

where the coefficients ζ and $\zeta_{\beta+1}$ are independent of Δx. If $\zeta \Delta x^\alpha \gg \zeta_{\beta+1} \Delta t^\beta$, we can calculate the spatial order of convergence by refining Δx with Δt held constant. For a general setting, however, we need to use an alternate method. This is achieved by comparing two uniform meshes with cell widths Δx_i and Δx_{i+1}, with $\Delta x_{i+1} < \Delta x_i$. Then we can write

$$\left(\hat{\tau}_{G_i^x}\right)_j \approx \zeta \Delta x_i^\alpha + \zeta_{\beta+1} \Delta t^\beta, \tag{49a}$$

$$\left(\hat{\tau}_{G_{i+1}^x}\right)_j \approx \zeta \Delta x_{i+1}^\alpha + \zeta_{\beta+1} \Delta t^\beta. \tag{49b}$$

Assuming $\left(\hat{\tau}_{G_{i+1}^x}\right)_j < \left(\hat{\tau}_{G_i^x}\right)_j$, we define

$$\begin{aligned} \left(\Delta \hat{\tau}_{G_{i,i+1}^x}\right)_j \equiv \left(\hat{\tau}_{G_i^x}\right)_j - \left(\hat{\tau}_{G_{i+1}^x}\right)_j &= \zeta \left(\Delta x_i^\alpha - \Delta x_{i+1}^\alpha\right) \\ &= \zeta \Delta x_{i+1}^\alpha \left\{ \left(\frac{\Delta x_i}{\Delta x_{i+1}} \right)^\alpha - 1 \right\} > 0. \end{aligned} \tag{50}$$

Defining $p = \Delta x_{i+1} / \Delta x_i < 1$ to be the ratio between the two mesh sizes, we can write

$$\left(\Delta \hat{\tau}_{G_{i,i+1}^x}\right)_j = \zeta \Delta x_{i+1}^\alpha \left(p^{-\alpha} - 1\right). \tag{51}$$

Upon taking the logarithm of both sides, we obtain

$$\log\left(\Delta \hat{\tau}_{G_{i,i+1}^x}\right)_j = \theta + \alpha \log\left(\Delta x_{i+1}\right), \tag{52}$$

where $\theta = \log\left\{\zeta\left(p^{-\alpha} - 1\right)\right\}$ is constant. To compute the spatial order of accuracy, we first choose a sequence of M grids with $\Delta x_{i+1} / \Delta x_i = p$ for $i = 1, 2, \ldots, M-1$, and all satisfying a CFL condition. After interpolating the error to the coarsest mesh with spacing Δx_1, we plot the norm of the difference between successive global errors $\left(\Delta \hat{\tau}_{G_{i,i+1}^x}\right)_{\text{norm}}$ against the cell width Δx_{i+1} on a log-log scale, for $i = 1, 2, \ldots, M-1$. The slope of the best-fit line gives us the spatial order of accuracy.

Proceeding in a similar fashion, we can ascertain the temporal order of accuracy. Specifically, we refine the time step while preserving the spatial resolution and plot the norm of the difference between successive global errors. Since the spatial resolution remains unchanged, there is no need for the interpolation step.

It is worth noting that the exact solution is independent of both the spatial resolution and the time step. So, for refinement only in time, if u_j^{n+1} represents the solutions at time level t^{n+1}, and $(\hat{u}_i)_j^{n+1}$ represents its numerical counterpart obtained with time step Δt_i, we can write

$$\begin{aligned}\left(\Delta\hat{\tau}_{G^t_{i,i+1}}\right)_j^{n+1} \equiv \left(\hat{\tau}_{G^t_i}\right)_j^{n+1} - \left(\hat{\tau}_{G^t_{i+1}}\right)_j^{n+1} &= \left\{u_j^{n+1} - (\hat{u}_i)_j^{n+1}\right\} - \left\{u_j^{n+1} - (\hat{u}_{i+1})_j^{n+1}\right\} \\ &= (\hat{u}_{i+1})_j^{n+1} - (\hat{u}_i)_j^{n+1} \equiv (\Delta\hat{u}_{i,i+1})_j^{n+1}\,. \quad (53)\end{aligned}$$

Therefore, if we calculate the difference $(\Delta\hat{u}_{i,i+1})_j^{n+1}$ between numerical solutions $(\hat{u}_i)_j^{n+1}$ and $(\hat{u}_{i+1})_j^{n+1}$ obtained with time steps Δt_i and Δt_{i+1} for $i = 1, 2, \ldots, M-1$, at every mesh point x_j and time level t^{n+1}, and then compute its norm $\left(\Delta\hat{u}G^t_{i,i+1}\right)_{\text{norm}}^{n+1}$ and plot it against Δt_{i+1}, we can achieve convergence at a rate matching the temporal order of accuracy. In the event of performing only a spatial refinement, it is necessary to first interpolate the numerical solution to the coarsest mesh. Subsequently, the same steps can be followed to achieve convergence aligned with the spatial order of accuracy. This methodology offers a practical advantage by eliminating the need to engage with exact or manufactured solutions, thereby streamlining the process and enhancing its applicability. In our own numerical experiments, we adopt this approach for verifying the spatial and temporal orders of accuracy for the planetary and topographic Rossby wave test cases, which are not equipped with exact solutions.

One should recognize that these unconventional convergence exercises primarily aim to verify the correct implementation of the spatial and temporal discretizations. The error norm of the numerical solution under only spatial or temporal refinement is not expected to converge in the asymptotic regime. It is only when the time step and the cell width undergo simultaneous refinement, while maintaining their ratio, that we can expect convergence of the global error norm.

4.6 Beyond Method of Lines Time Integrators

We reiterate that the full expression (45) for the local truncation error was specifically derived for Method of Lines time integrators in Bishnu (2021). This formulation does not universally apply to time integrators that concurrently handle spatial and temporal discretizations, and are applicable exclusively to PDEs. Notable exceptions, such as the Lax-Wendroff method, do exist. Nevertheless, if the specific form of the local truncation error is known beforehand, the principles, methodologies, and anticipated outcomes for performing space-time, space-only, or time-only convergence studies, as discussed in Sections 4.3 to 4.5, may be extended to time integrators beyond Method of Lines, with appropriate adjustments.

5 Numerical Dispersion, Numerical Dissipation, and Spurious Oscillations

Numerical dispersion and numerical dissipation are intrinsic challenges that arise when approximating PDEs using numerical methods. These phenomena are particularly impactful in wave-propagation problems, with dispersion errors influencing the propagation speed of disturbances and dissipation errors impacting the strength.

Numerical dispersion commonly manifest in conservation laws when the dominant truncation error stems from odd-order derivatives, causing a misrepresentation of the wave's phase speed. Dispersion errors are observed not only in finite difference and finite volume

methods, but also in high-order methods like single- and multi-domain SEMs. It is crucial to underscore that even though high-order methods like DGSEM boast increased accuracy, they are not immune to dispersion, especially at element boundaries with discontinuous solutions. Here, the choice of basis functions and the employed Riemann solver play pivotal roles. Even with high-order polynomial approximations, phase errors may arise as waves cross multiple elements.

Numerical dissipation or diffusion, usually linked with even-order derivatives in the truncation error, signifies the artificial attenuation of the solution introduced by numerical methods. For example, first-order upwind schemes inherently dampen waves. So, while physically a wave might maintain its amplitude, numerically it could wane over time due to this effect. In the context of DGSEM, the primary source of artificial damping is the Riemann solvers at element boundaries. While the polynomial representation within an element may be non-dissipative, the Riemann solvers, which facilitate information exchange between elements, can introduce dissipation. This can lead to a slight reduction in amplitude over extended simulation times. As detailed in Section 5.1 with the local Lax-Friedrichs Riemann solver as an example, such damping effects, although vital for maintaining numerical stability, do not necessarily compromise the spatial order of accuracy. The terms "numerical dissipation" and "numerical diffusion" are often used interchangeably to address this damping effect, especially when dealing with sharp gradients or discontinuities. However, "numerical dissipation" typically emphasizes the removal of high-frequency components, especially in the context of stabilizing a numerical solution. In contrast, "numerical diffusion" underscores the artificial smoothing of particular features in the solution.

Spurious oscillations represent another significant challenge in the numerical simulation of physical phenomena, particularly when the mathematical models involve discontinuities or steep gradients. These non-physical oscillations are most noticeable as "wiggles" or "overshoots" in the vicinity of abrupt changes, such as shock waves or material interfaces, and are indicative of the numerical method struggling to reconcile the sharp variations in the solution's profile. High-order numerical methods like SEMs, while offering enhanced accuracy over smoother parts of the solution, are particularly susceptible to this phenomenon, a manifestation of the well-documented "Gibbs phenomenon". Spurious oscillations are especially troublesome as they do not dissipate over time. Instead, they may intensify if the numerical scheme lacks the necessary stability features, potentially compromising the entire solution. However, the numerical community has developed several strategies to suppress these oscillations, thus enhancing the fidelity of simulations. The introduction of numerical dissipation, for example, can help to damp out these oscillations by smoothing the solution in a controlled manner. Artificial viscosity is another effective tool, subtly altering the equations to increase the physical diffusion, which helps to eliminate non-physical fluctuations. Moreover, the implementation of carefully designed limiters can specifically target and neutralize spurious oscillations without significantly distorting the true solution.

5.1 The Dissipative Local Lax-Friedrichs Riemann Solver and the Spatial Order of Accuracy of DGSEM

The numerical flux obtained using the local Lax-Friedrichs (LLF) Riemann solver can be expressed as

$$F_{LLF} = \frac{1}{2}\left\{f\left(U_L\right) + f\left(U_R\right)\right\} - \frac{|\lambda|}{2}\left(U_L - U_R\right). \tag{54}$$

Here, U_L and U_R represent the left and right states, respectively. The parameter $|\lambda|$ signifies the maximum characteristic speed of the Riemann problem, commonly estimated as the magnitude of the maximum eigenvalue or wave speed across U_L and U_R. The central flux $\frac{1}{2}\left\{f\left(U_L\right) + f\left(U_R\right)\right\}$ is essentially the average of the fluxes from the left and right. On its own, it is a second-order central scheme, prone to spurious oscillations near discontinuities. The dissipative term $\frac{|\lambda|}{2}\left(U_L - U_R\right)$ acts to dampen those oscillations. It is proportional to

the jump in the solution, so it is stronger (more dissipative) where the solution has steep gradients or discontinuities.

In spectral element methods including DGSEM, the solution within each element is approximated by high-order polynomials. Hence, flux computation at boundaries does not solely rely on boundary values, as seen in many lower-order finite volume methods. Instead, the polynomial approximation of the internal solution is interpolated to the boundaries, ensuring high-order accuracy right upto the edge. Fluxes are then computed using these interpolated values from neighboring elements, with the LLF Riemann solver subsequently applied. It is crucial to note that the LLF solver's primary role in this context is not flux computation but determining the upwind direction based on eigenvalues and introducing the necessary dissipation for numerical stability. The high-order accuracy of the spectral element method stems from its polynomial representation, not the Riemann solver. In simpler terms, the LLF Riemann solver does not cause first-order accuracy in finite volume methods. It is the low-order approximations of the left and right states, U_L and U_R, used as inputs. With DGSEM, both U_L and U_R are spectrally accurate, resulting in much smaller jumps. As such, while the Lax-Friedrichs method is intrinsically first order, the LLF Riemann solver does not degrade the DGSEM's overall accuracy.

Numerous works, such as Hussaini and Zang (1987), Boyd (1988), Cockburn and Shu (1989), Cockburn and Shu (1998), Hesthaven and Warburton (2007), Canuto et al. (2007b), Canuto et al. (2007a), and D. A. Kopriva et al. (2017) extensively explore spectral methods and their synergy with Riemann solvers. These studies imply that various Riemann solvers can integrate with spectral methods without compromising their inherent accuracy. Our convergence plots demonstrate that even with the LLF Riemann solver, we achieve the anticipated high-order accuracy typical of spectral element methods. Nonetheless, while the LLF Riemann solver might not diminish the accuracy order, it is known to introduce more dissipation than other Riemann solvers, potentially impacting the quality of the solution in terms of sharpness of features or the preservation of certain scales.

6 Numerical Experiments

We first outline the experimental procedure used to conduct these numerical experiments and verify the spatial and temporal orders of accuracy of the barotropic solver or the dynamical core of ocean models. We believe that this recipe will serve as a valuable resource to ocean modelers by ensuring that their respective ocean models actually converge at the expected order of accuracy. We proceed by plotting the time evolution of numerical errors, studying their nature, and creating convergence plots for each test case, with refinement in both space and time, only in space, and only in time.

This comprehensive approach, involving three flavors of convergence tests, may seem overly detailed at first glance. However, it is chosen for a number of reasons. Consider an ocean model employing a low-order finite volume method for spatial discretization. The standard practice in ocean modeling is to conduct convergence studies by refining in both space and time, i.e., by simultaneously reducing the time step and cell width while maintaining their ratio (and the Courant number) constant. However, if a time-stepping method of order higher than the spatial discretization is used, a convergence plot with refinement in both space and time will always converge at the spatial order of accuracy in the asymptotic regime, thereby hindering the verification of the temporal order of accuracy. This is further compounded by the fact that the leading-order spatial error term's coefficient is typically a few orders of magnitude larger than that of the leading-order temporal error term, a phenomenon we will refer to as leading-order coefficient discrepancy from here onward. Consequently, order reduction is seldom observed before reaching the asymptotic regime, and the convergence rate invariably mirrors the (low) spatial order of accuracy. Moreover, ocean models being typically characterized by their spatial discretization, may allow users to choose from multiple time-stepping methods. During the integration of a

novel time-stepping method into a fully functional ocean model, a developer might want to verify solely its order of accuracy, underscoring the necessity for self-refinement tests only in time.

In contrast, consider an ocean model where the spatial order of accuracy far surpasses its temporal counterpart. With refinement in both space and time, order reduction may be observed as the numerical solution error is expected to progress through three distinct regimes: spatial discretization error dominance (first regime), temporal discretization error dominance (second regime which overlaps with the beginning of the asymptotic regime where Δx^α and Δt^β in (46) exert dominance over their respective coefficients), and finally, round-off error dominance (third regime). However, in practice, for the selected sets of discretization parameters Δx and Δt, the error might not traverse all three regimes. If the round-off error takes over before the time integration error, verification of the temporal accuracy order becomes impossible. Similarly, if the leading-order coefficient discrepancy is insufficient, the first regime may be bypassed in favor of the second and third regimes even at relatively low resolutions, preventing the verification of the spatial order of accuracy. This demonstrates the necessity for self-refinement tests in both space and time. To mitigate the impact of round-off errors in spectral element discretizations, it is crucial to avoid excessively high polynomial orders during convergence studies. Last but not the least, self-refinement tests in space can ensure that code modifications, such as incorporating a new time-stepping method, do not inadvertently introduce bugs that detrimentally affect the spatial order of accuracy.

We now outline the experimental procedure for numerical experiments and convergence studies below. After addressing the initial steps for spatial operators and their convergence, which are common to all test cases, the procedure for individual test cases remains consistent.

6.1 Experimental Procedure

1. Construct the mesh for discretizing the numerical solution. This mesh will also be used for visualization of the exact and numerical solutions, and the associated error. Create a set of meshes with different spatial resolutions for conducting convergence studies in both space and time, and only in space. For convergence studies only in time, a single spatial mesh suffices.
2. Specify a smooth function in space, which can be selected from the initial condition of a test case. Evaluate both the exact and numerical spatial operators of this function on the mesh, then plot these operators alongside their error. Ensure that the error norm is considerably smaller than the operator norm, by at least several orders of magnitude for high-order spectral element methods and a few orders for low-order finite volume methods. Conduct convergence tests of these spatial operators with spatial refinement to confirm that their convergence slopes align with the expected spatial order of accuracy.
3. Identify an exact or manufactured solution if applicable, keeping in mind that for finite volume methods, the exact solutions pertain to cell- and edge-averaged quantities rather than cell- or edge-centered ones. Consult Section C1 in Appendix C for an insightful explanation on initializing these quantities on non-rectilinear meshes, utilizing the hexagonal meshes of MPAS-Ocean as an illustrative example.
4. Given a characteristic wave speed, choose an appropriate Courant number that is consistent with the CFL condition for both the spatial and temporal discretizations. Regarding the specification of the characteristic wave speed, consider the following examples. For the coastal Kelvin and inertia-gravity wave test cases, define the characteristic wave speed as the phase speed of the faster wave mode. For the Rossby wave test cases, set the characteristic wave speed as the phase speed of the fastest gravity waves emitted by the initially Gaussian monopole. For explicit time integration methods, the CFL condition mandates that the Courant number must be less than one to ensure stability. This requirement becomes even more stringent with

explicit multistep time-integration methods, such as Adams-Bashforth, where the region of absolute stability narrows with higher orders, necessitating an even smaller Courant number. Based on this choice, determine the time step. Initialize the model using the exact solution at $t = 0$. Implement boundary conditions that mirror the exact solution over time. Likewise, define space- and time-dependent source terms for manufactured solutions. For detailed guidelines on setting boundary conditions and source terms on non-rectilinear meshes, refer to Sections C1 and C2 in Appendix C, again using the hexagonal meshes of MPAS-Ocean as a reference. Run the model forward in time to obtain the numerical solution. At intervals equivalent to integral multiples of the time step, print and plot both the exact and numerical solutions, along with the associated error, to study their temporal evolution.

5. Employ visual inspection (sometimes humorously referred to as the 'eyeball norm') to assess the numerical solution for approximate physical and numerical accuracy, examining, for instance, whether geophysical waves propagate at their theoretically expected phase speeds. If errors significantly amplify along the boundaries compared to the domain's interior, reevaluate the implementation of boundary conditions or the plotting of boundary values. As with the spatial operators, the error norm should be substantially smaller than the solution norm, with the difference being more pronounced for high-order spectral element methods than low-order finite volume methods.
6. After achieving satisfactory preliminary results, initiate comprehensive convergence studies, with refinements in both space and time, only in space, and only in time. Revisit the beginning of this section for the underlying reasoning behind these different flavors of convergence tests and specific strategies tailored for low- and high-order spatial discretizations. For refinement in both space and time, adjust the time step in direct proportion to the cell width, ensuring that their ratio and the Courant number remain constant. When refining only in space, determine the time step for the finest mesh using the Courant number. Employ this stringent time step across all spatial resolutions. For convergence tests with refinement only in time, calculate the largest time step based on the Courant number for the singular spatial mesh in use.
7. The refinement ratio between successive pairs of spatial or temporal resolutions does not necessarily need to be an integer. This flexibility is particularly advantageous for convergence tests only in space, the most computationally intensive type. Following that in computational demand is the convergence test in both space and time, and finally the convergence test only in time. The error norm in a convergence test is calculated at a specific time horizon. This horizon is always reached if:
   (a) refinement is performed only in space, implying a constant time step value;
   (b) the time horizon equates to an integral number of the largest time step, and the refinement ratio is integral e.g doubling each time.

   This may not hold true for convergence tests with refinement in both space and time or only in time when the refinement ratio is not an integer. Nonetheless, a clever approach can circumvent this issue. By selecting a rational refinement ratio, $r = p/q$ for $p > q$ and $p, q \in \mathbb{Z}^+$, and denoting s as the number of different resolution sets, we can define the time horizon as $T = N\Delta t_{\text{largest}}$, with $N = q^t$, $t \in \mathbb{Z}^+$ and $t \geq s$. As lengthy simulation times are generally unnecessary for convergence tests, t does not need to greatly exceed s. For example, with $r = 3/2$ and $s = 5$, we can choose N to be powers of 2 equal to or greater than 32. This ensures that the time horizon aligns with integral multiples of every time step used in the study, obviating the need for adjustments that could lead to errors.
8. For refinement in both space and time, employ a test case with either an exact or a manufactured solution, and plot the actual error norm at a designated time horizon against either the cell width or the total number of cells. For refinement only in space or only in time, plot the norm of the difference between
   (a) the numerical solutions; or
   (b) the error (for test cases equipped with exact solutions);

against the cell width (or number of cells) or the time step (or number of time steps) for successive pairs of spatial and temporal resolutions.

9. Analyze whether the convergence slope:

   (a) aligns with the spatial or temporal order of accuracy when refining only in space or only in time;
   (b) corresponds to the lesser of the spatial and temporal orders of accuracy when refining in both space and time.

   If the above observations hold true, our results are satisfactory. However, deviations from these patterns may point to issues such as:

   (a) a bug within the numerical implementation of spatial or temporal discretizations;
   (b) the asymptotic regime not yet reached by the spatial and temporal resolutions, suggesting a need for broader resolution sets in convergence studies.
   (c) the dominance of round-off errors, a common issue in high-order spectral element methods, which can be remedied by reducing the polynomial order.

10. In scenarios where machine precision constraints may preclude reaching the asymptotic regime, separate spatial and temporal convergence tests are crucial. It is also vital to diversify test cases, given that error magnitudes can vary based on the exact solution and its gradients.

The above procedure sets the stage for a rigorous numerical study that can adapt to different scenarios, accounting for the particularities and complexities inherent to both finite volume and spectral element methods, and offering flexibility in convergence testing and verification.

6.2 Numerical Solutions and Convergence Plots

Based on our experimental procedure, we begin by testing the convergence of the various spatial operators. For the TRiSK-based mimetic finite volume method, these encompass the gradient, divergence, curl, kinetic energy, and Laplacian operators as well as the interpolation or flux-mapping operator. This last operator is used to obtain the tangential velocity on an edge from the normal velocities on the edges of the cells sharing that edge. In contrast, for DGSEM, the only pertinent spatial operators are the zonal and meridional gradient operators.

We opt for a smooth spatial test function, which, along with its gradient and Laplacian, is expressed as:

$$\eta = \hat{\eta} \sin\left(\frac{2\pi x}{L_x}\right) \sin\left(\frac{2\pi y}{L_y}\right), \tag{55a}$$

$$\begin{aligned}\nabla\eta &= \eta_x \boldsymbol{i} + \eta_y \boldsymbol{j} \\ &= 2\pi\hat{\eta}\left\{\frac{1}{L_x}\cos\left(\frac{2\pi x}{L_x}\right)\sin\left(\frac{2\pi y}{L_y}\right)\boldsymbol{i} + \frac{1}{L_y}\sin\left(\frac{2\pi x}{L_x}\right)\cos\left(\frac{2\pi y}{L_y}\right)\boldsymbol{j}\right\},\end{aligned} \tag{55b}$$

$$\nabla^2\eta = \nabla\cdot\nabla\eta = -\left\{\left(\frac{2\pi}{L_x}\right)^2 + \left(\frac{2\pi}{L_y}\right)^2\right\}\eta. \tag{55c}$$

By defining the surface elevation via (55a), the components of the geostrophic velocity field emerge as $u = -g/f\eta_y$ and $v = g/f\eta_x$, where $g = 10$ m s^{-2} and $f = 10^{-4}$ s^{-1}. If an edge's normal forms an angle θ with the positive direction of the zonal axis, the velocity field components in the normal ($\boldsymbol{n}$) and tangential ($\boldsymbol{t} = \boldsymbol{k} \times \boldsymbol{n}$) directions are represented as $\boldsymbol{u}^n = \mathcal{N}\boldsymbol{u} = u\cos\theta + v\sin\theta$ and $\boldsymbol{u}^t = \mathcal{T}\boldsymbol{u} = v\cos\theta - u\sin\theta$. The vertical component of the curl of the velocity field, the kinetic energy, and the Laplacian of the normal velocity at

the edges are defined as

$$\zeta = \boldsymbol{k} \cdot \nabla \times \boldsymbol{u} = \boldsymbol{k} \cdot \nabla \times (u\boldsymbol{i} + v\boldsymbol{j}) = v_x - u_y = \frac{g}{f}\nabla^2 \eta, \tag{56a}$$

$$K = \frac{1}{2}|\boldsymbol{u}|^2 = \frac{1}{2}(u^2 + v^2) = \frac{g^2}{2f^2}\left(\eta_x^2 + \eta_y^2\right), \tag{56b}$$

$$\nabla^2 \boldsymbol{u}^n = \frac{g}{f}\nabla^2\left(-\eta_y \cos\theta + \eta_x \sin\theta\right) = -\frac{g}{f}\nabla^2 \mathcal{T}\nabla\eta = \frac{g}{f}\left\{\left(\frac{2\pi}{L_x}\right)^2 + \left(\frac{2\pi}{L_y}\right)^2\right\}\mathcal{T}\nabla\eta. \tag{56c}$$

It is worth noting that although our test function was defined by (55), any function exhibiting smooth spatial variation in both zonal and meridional directions, such as the initial conditions for the geophysical waves or the manufactured solution, would have served the purpose.

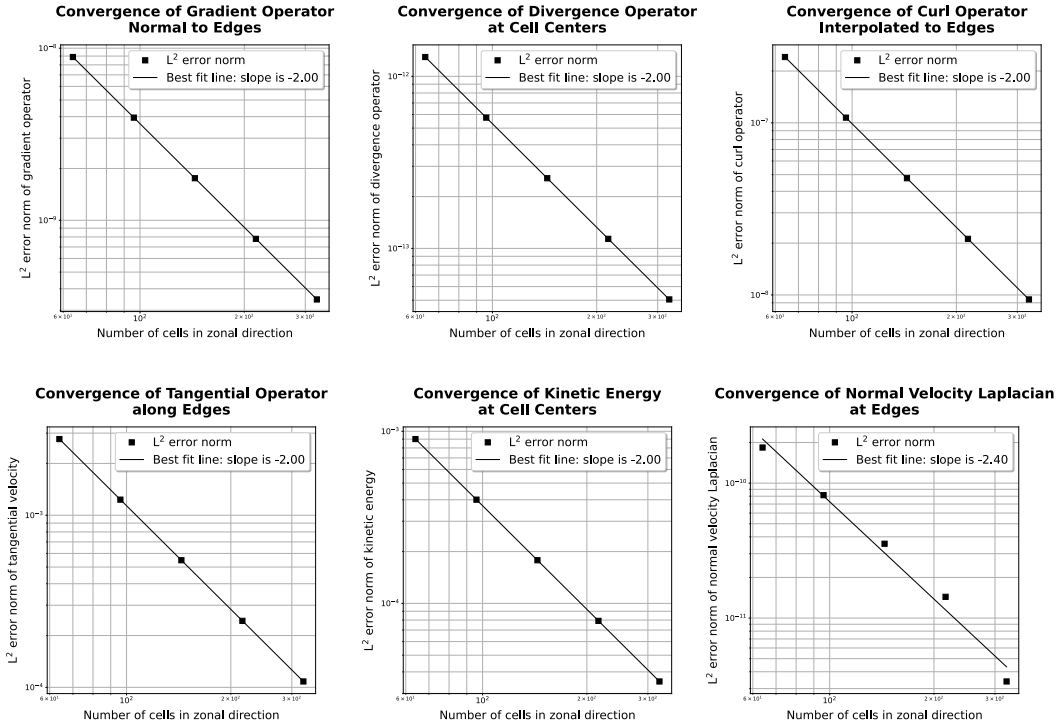

Figure 8. Convergence of TRiSK-based spatial and flux-mapping operators applied to the test function (55) on a uniform MPAS-Ocean mesh.

Figure 8 displays the convergence plots for the TRiSK-based spatial operators, which are all second-order accurate as expected. These studies were carried out on uniform planar hexagonal MPAS-Ocean meshes. These meshes have an equal number of cells, say N, in both zonal and meridional directions. Each row is offset by half a cell width, and the configuration ensures that the regular hexagons' parallel sides align with the meridional direction. Given that Δx denotes the distance between cell centers, the side length of these hexagonal cells is $1/\sqrt{3}\Delta x$. Consequently, the leading-order spatial discretization error term for the second-order TRiSK scheme can be represented as $\mathcal{O}\left(\Delta x^2\right)$. With the zonal domain extent set to $L_x = N\Delta x$, maintaining a constant L_x while increasing N means a log-log plot of the error norm against N will display a slope identical in magnitude to that against Δx. Hence, in our plots, we designate the x-axis as the cell count N, a choice enhancing visualization as refinement progresses in the positive x-direction.

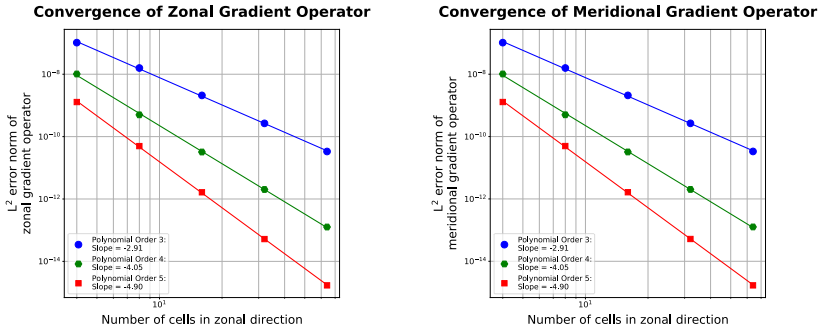

Figure 9. Convergence of weak forms of the zonal and meridional gradient operators of DGSEM applied to the test function (55) for polynomial orders 3, 4, and 5.

Figure 9 displays the convergence plots for the weak forms of DGSEM's zonal and meridional gradient operators, utilizing the Bassi-Rebay method (Bassi & Rebay, 1997) to approximate functions at the element boundaries. Notably, the convergence slopes align with the orders of the polynomial basis functions. Although not depicted here, additional convergence tests were performed on the strong form of these gradient operators, yielding identical results. In our spectral element meshes, we specified the number of elements N, the length of each element Δx, and the order of the polynomial basis functions p to be the same in both the zonal and meridional directions. For complete functions, the leading-order spatial error term for our DGSEM solution takes the form

$$\varepsilon = k_1 \exp\left(-k_2 p\right) \Delta x^p, \tag{57}$$

where k_1 and k_2 are constants. Equation (57) follows from the in-depth error analysis of DGSEMs in spectral element textbooks by Karniadakis and Sherwin (2005), Hesthaven and Warburton (2007), and Canuto et al. (2007b). Taking the logarithm of both sides of (57) gives

$$\ln \varepsilon = \ln k_1 - k_2 p + p \ln \Delta x = k_3 - p\left(k_2 - \ln \Delta x\right). \tag{58}$$

We recall from Section 3.2 that a spatial refinement in DGSEM can be performed in two ways: by increasing p while maintaining a constant N (p-refinement), or vice versa (h-refinement, where h denotes the cell width Δx). Equation (58) shows that p-refinement is expected to yield a straight line with negative slope of magnitude $k_2 - \ln \Delta x$ on a log-log graph, demonstrating exponential convergence. In contrast, an h-refinement should render a straight line with a slope of magnitude p, akin to finite difference or finite volume methods. Moreover, p-refinement is not applicable in the context of the TRiSK-based finite volume method, for which the effective polynomial order remains fixed at second order. To ensure a consistent and clear presentation, we have chosen to display the spatial convergence plots, employing h-refinement, for both DGSEM and TRiSK in a sequential and organized manner.

The Courant number, critical for the stability of numerical simulations, can be defined for two-dimensional advective problems as

$$C = \Delta t \left(\frac{c_x}{\Delta x} + \frac{c_y}{\Delta y} \right), \tag{59}$$

where c_x and c_y are wave speeds, while Δx and Δy denote grid scales in the zonal and meridional directions respectively. For DGSEM, employing rectangular elements with side lengths Δx and Δy, the Courant number modifies to

$$C = \Delta t \left(\frac{c_x}{\frac{\Delta x}{P_x^2}} + \frac{c_y}{\frac{\Delta y}{P_y^2}} \right) = \Delta t \left(P_x^2 \frac{c_x}{\Delta x} + P_y^2 \frac{c_y}{\Delta y} \right), \tag{60}$$

where P_x and P_y represent the orders of the polynomial basis function in the zonal and meridional directions respectively. Given that the internal grid of each spectral element has higher density towards the edges, the measures $\Delta x/P_x^2$ and $\Delta y/P_y^2$ offer close estimates for the smallest internal grid spacings adjacent to these edges. In uniform planar hexagonal MPAS-Ocean meshes, where Δx indicates the distance between neighboring cell centers, and in DGSEM meshes using spectral elements with side lengths Δx and polynomial order P in both horizontal directions, the CFL condition can be concisely represented as

$$C = \lambda \Delta t/\Delta x, \text{ where } \lambda = \begin{cases} c_x + \frac{2}{\sqrt{3}} c_y & \text{for TRiSK,} \\ c_x + c_y & \text{for DGSEM.} \end{cases} \tag{61}$$

In our simulations, we specify c_x and c_y to be the zonal and meridional components of the phase speed for the manufactured wave solution; the phase speed of the faster wave mode for the coastal Kelvin and inertia-gravity waves; and the phase speed of the component waves of the standing wave mode with faster components for the barotropic tide.

In each horizontal direction, let N represent the number of hexagonal cells for TRiSK and the count of spectral elements for DGSEM. Additionally, let P symbolize the polynomial order in each direction for DGSEM. For the TRiSK-based approach, we utilize a structured planar hexagonal MPAS-Ocean mesh with $N = 100$. The spectral element mesh for DGSEM is defined by $N = 5$ and $P = 10$ in all test cases except for the Rossby waves, resulting in 10^{th} order spatial accuracy. For the Rossby wave test cases, we specify $N = 10$ and $P = 7$, yielding a 7^{th} order spatial accuracy. The zonal domain extent, L_x is specified as 5×10^6 m, 10^7 m, 10^6 m, 2.5×10^5 m, and 10^7 m for the coastal Kelvin wave, the inertia-gravity wave, the Rossby waves, the barotropic tide and the manufactured solution test cases respectively. The distance between the adjacent hexagonal cell centers for TRiSK, as well as the side lengths of the spectral elements for DGSEM are given by $\Delta x = L_x/N$. For DGSEM, the smallest grid spacings near element boundaries are approximately $\Delta x/P^2$. The meridional domain extent L_y is set to $\sqrt{3}/2 L_x$ for TRiSK, resulting in a "measure" for the meridional grid scale $\Delta y = L_y/N = \sqrt{3}/2 \Delta x$. For DGSEM, L_y, Δy, and the meridional grid spacings mirror their zonal counterparts. By leveraging (61) to maintain the Courant number, C, near 0.5, we specify the time step, Δt, in the coastal Kelvin wave, inertia-gravity wave, barotropic tide, and manufactured solution test cases to be 200 s, 100 s, 10 s, and 180 s respectively for TRiSK, and 50 s, 25 s, 2.5 s, and 30 s respectively for DGSEM. For the Rossby wave test cases, a particularly small $\Delta t = 0.5$ s is selected for both TRiSK and DGSEM to meet the CFL condition for the fastest gravity waves, ensuring numerical stability.

The numerical solutions being visually indistinguishable from their exact counterparts, we limit our presentation to the time evolution of surface elevation errors for the coastal Kelvin wave, inertia-gravity wave, barotropic tide, and the non-linear manufactured solution, as shown in Figures 10, 11, 12, and 13. These solutions are advanced with Williamson's low-storage third-order Runge-Kutta time-stepping method, and spatially discretized with TRiSK and DGSEM. The error stemming from these two types of spatial discretizations is depicted in the first and second rows of Figures 10—13. At first glance, we notice that the TRiSK error is three orders of magnitude less than the solution magnitude for the linear coastal Kelvin wave, inertia-gravity wave, and barotropic tide test cases. It is two orders of magnitude less for the non-linear manufactured solution test case. Conversely, the DGSEM error is six orders of magnitude less than the solution error for the coastal Kelvin wave and barotropic tide test cases, and eight orders of magnitude less for the inertia-gravity wave and manufactured solution test cases.

In our analysis of the temporal evolution of the coastal Kelvin wave error for both TRiSK and DGSEM (Figure 10), it is evident that the error modes propagate not only meridionally from north to south in line with the wave direction, but also zonally from west to east. Even though the exact tendency of the zonal velocity in the linear rotating shallow water equations (10) is zero, due to a balance between the exact Coriolis and pressure

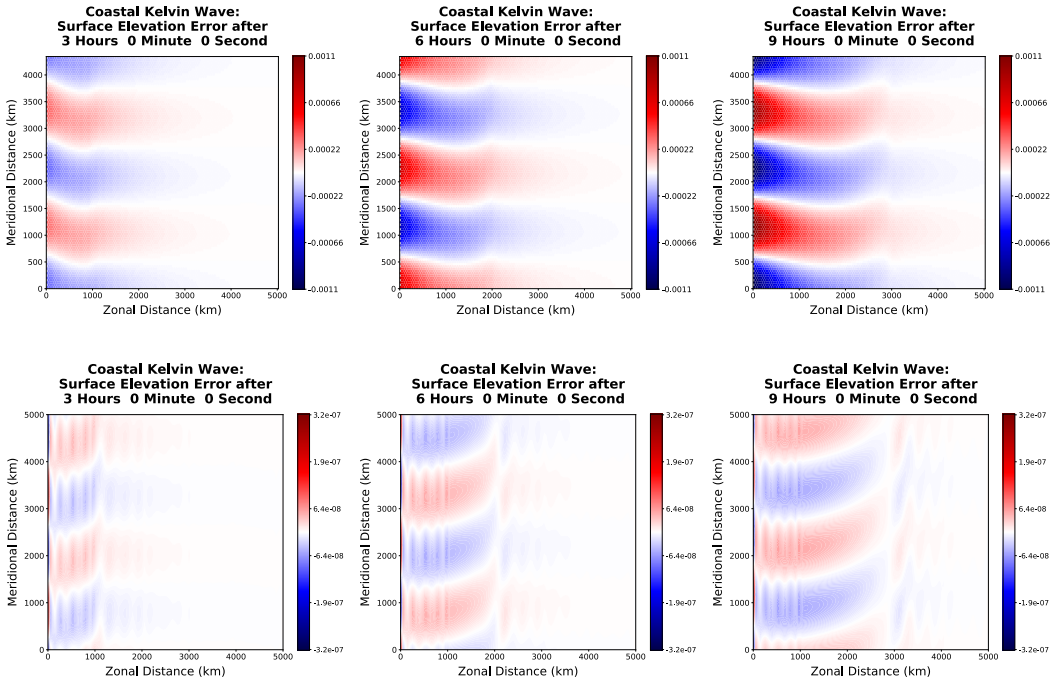

Figure 10. Time evolution of the surface elevation error of TC1, the coastal Kelvin wave, spatially discretized with the TRiSK-based mimetic finite volume method (first row), and DGSEM using 5 elements and polynomial basis functions of order 10 in each horizontal direction (second row).

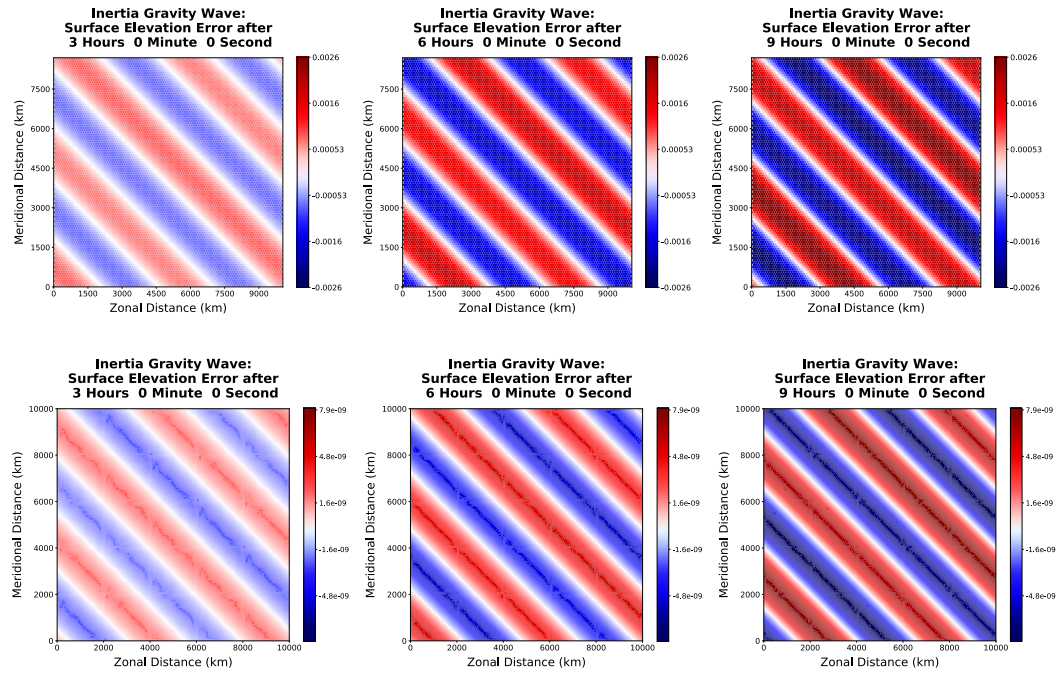

Figure 11. Same as Figure 10, but for TC2, the high-frequency dispersive inertia-gravity wave, showing error for TRiSK (first row), and DGSEM (second row).

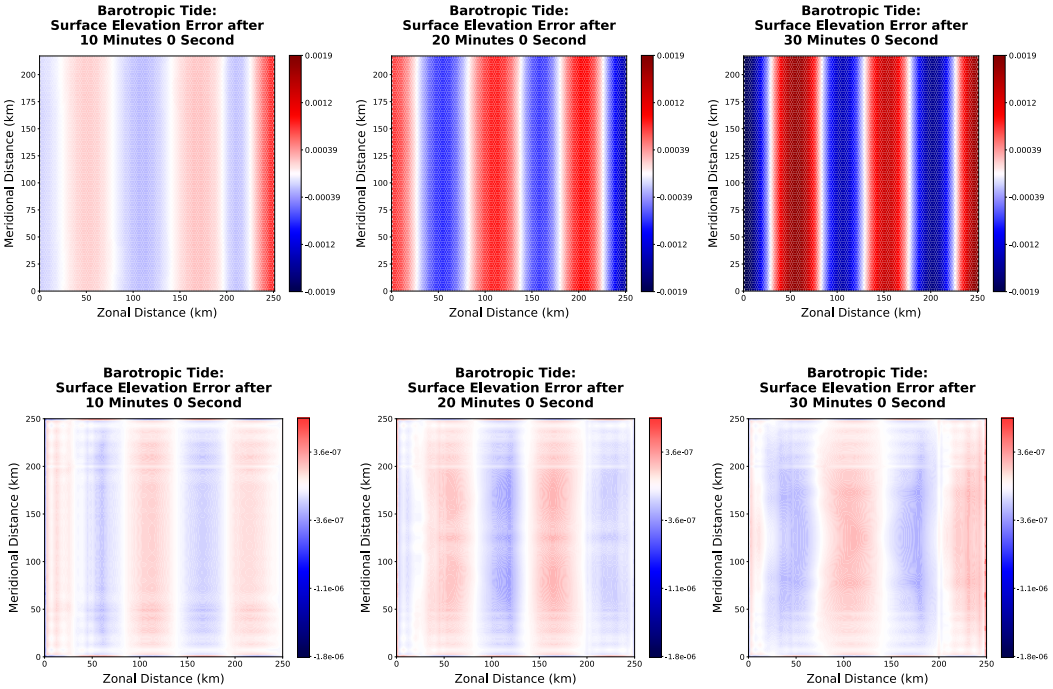

Figure 12. Same as Figure 10, but for TC5, the barotropic tide test case, showing error for TRiSK (first row), and DGSEM (second row).

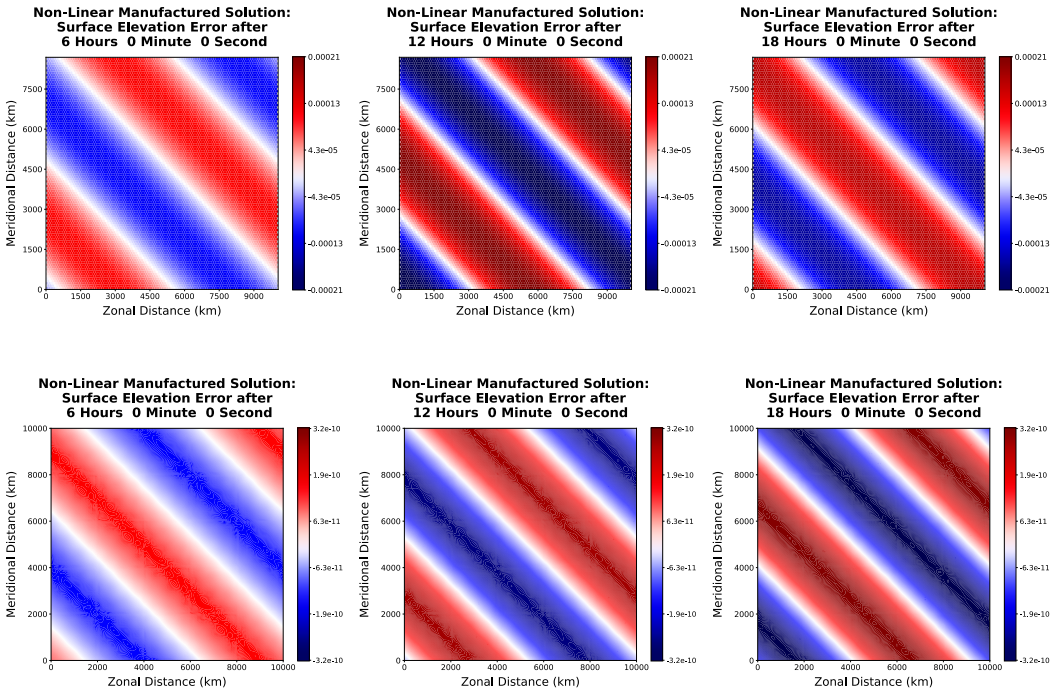

Figure 13. Same as Figure 10, but for TC6, the non-linear manufactured solution test case, showing error for TRiSK (first row), and DGSEM (second row).

gradient terms in (10a), its numerical counterpart is not. Referring to our discussion in Section 4.2, the spatial discretization error in the pressure gradient term of (10a) is of order $\mathcal{O}(\Delta x^{\alpha})$. This non-zero error gives rise to a discernible numerical zonal velocity, serving as a catalyst for the error modes to propagate in both zonal and meridional directions. Moreover, the western boundary, characterized by high gradients and the imposition of a no-normal flow condition, act as an incubator for error. As the simulation progresses, the errors originating from this boundary permeate the interior domain. Notably, these error modes propagate at speeds identical to the shallow water gravity wave speed, a reflection of the system's inherent physics. Interested readers may consult Figure A1 in Appendix A, which depicts the exact solution plots for a plane wave test case traveling at the gravity wave speed. They will observe a notable similarity between these plots and the aforementioned error modes. Such behavior underscores the principle that errors in numerical simulations tend to mirror the dynamics of the governing equations. This, in conjunction with the zonal error propagation, may account for the prominent west-to-east movement of errors observed. A distinctive front-like feature is observed migrating from west to east. Our interpretation suggests that this front represents the initial "boundary layer" of error, emanating from the western boundary. As this layer advances eastward, it collides with the pre-existing errors, predominantly moving southward. This intricate dance between the boundary-induced and interior error modes gives birth to the observed "front".

We recall that the prescribed exact solutions for both the coastal and inertia-gravity waves are constructed as a superposition of two wave modes. The second mode possesses twice the amplitude and wavenumber relative to the first. Owing to the inherently dispersive nature of the inertia-gravity wave, these modes propagate with different phase speeds. This disparity in propagation speeds is manifested by the temporal variation of the solution's amplitude and the width of its positive and negative "bands" (Figure 2). Intriguingly, the error exhibits analogous behavior. Given the absence of physical boundaries combined with the imposition of periodic boundary conditions, the error advances coherently in the direction of the solution (Figure 11). This observation again underscores that the system's underlying physics significantly shapes the error's dynamics, mirroring the solutions of the governing equations.

The barotropic tide test case serves as a benchmark for evaluating an ocean model's proficiency in simulating standing waves, a critical feature for coastal applications. While an initial assessment based on error magnitude (Figure 12) and convergence rate (Figure 18) suggests promising results for both TRiSK and DGSEM, a closer examination of the DGSEM error plots uncovers patterns that could be attributed to either spurious oscillations or numerical dispersion. On the other hand, the inherent dissipation of TRiSK damp outs potential oscillations and dispersive errors that the more accurate DGSEM tends to pick up. It is worth noting that despite these subtle numerical artifacts observed in DGSEM, which were discernible only upon meticulous examination, the error magnitude for DGSEM remains significantly lower than that of TRiSK at equivalent or even lower spatial resolution.

Finally, interpreting the error dynamics of the non-linear manufactured solution test case (Figure 13) can be notably challenging. Nonlinearities inherently introduce a range of complex interactions and dependencies between different solution features. While in linear settings numerical artifacts like dispersion and oscillations may have predictable patterns, in non-linear contexts these patterns can be distorted, merged, or even amplified in unexpected ways. The intricacies of non-linear interactions can often cloak or overshadow the typical behaviors we associate with numerical errors. As a result, even when we observe smooth error fields as in Figure 13, these might be the consequence of numerous intertwined effects which, in isolation, would appear differently. This complexity not only complicates our ability to decipher the source or nature of errors but also underscores the importance of supplementing visual error assessments with quantitative tools like convergence plots (Figure 19) in non-linear scenarios.

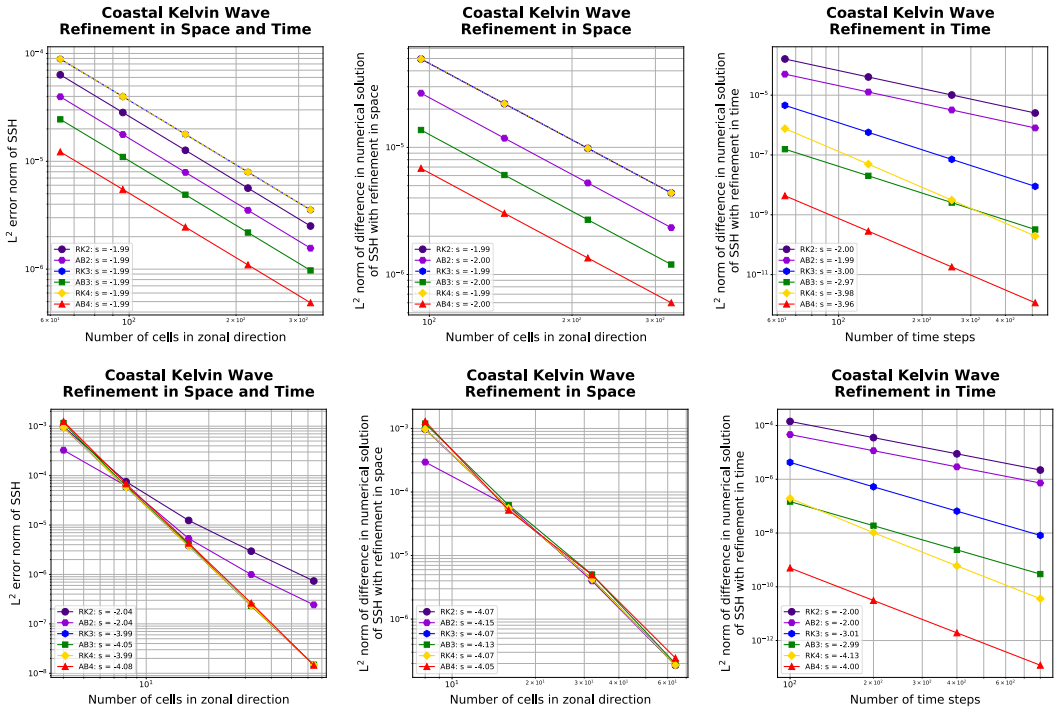

Figure 14. Convergence plots of TC1, the non-dispersive coastal Kelvin wave, discretized with TRiSK (first row) and DGSEM (second row), for refinement in space and time (first column), refinement in space (second column), and refinement in time (third column). The slope of the best-fit line, s, is shown in each legend.

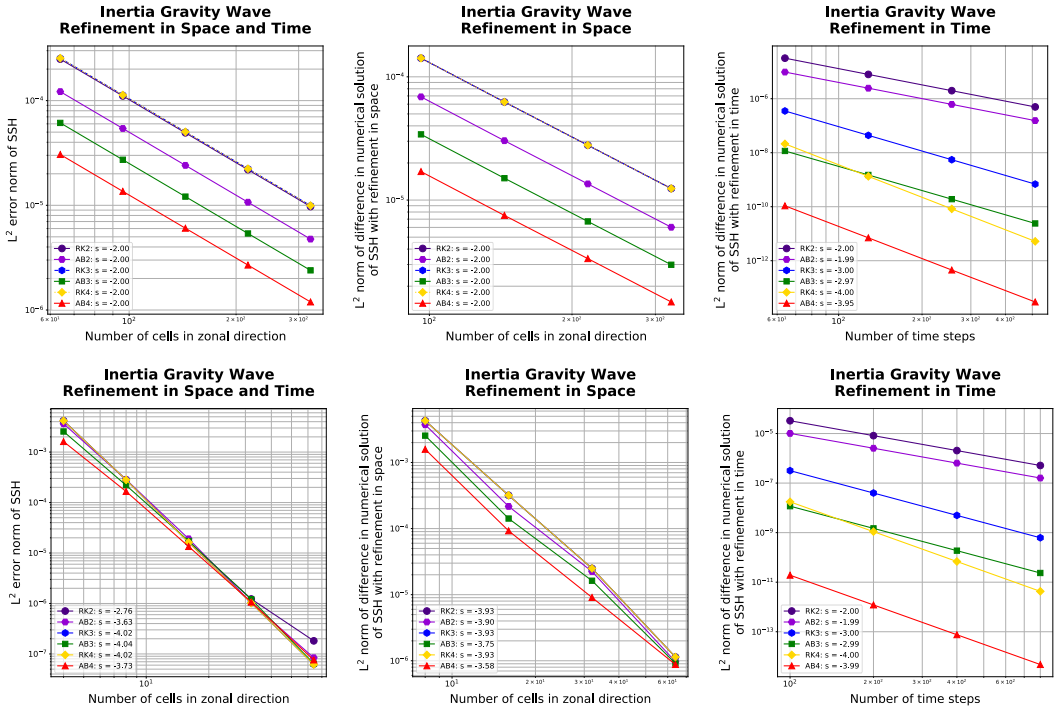

Figure 15. Same as Figure 14, but for TC2, the dispersive inertia-gravity wave.

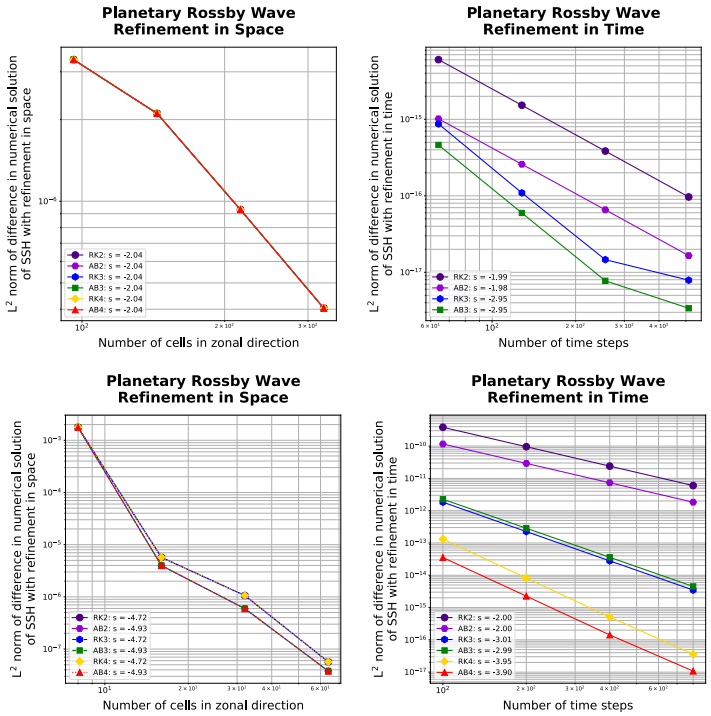

Figure 16. Convergence plots of the solution difference norm of TC3a, the linear dispersive planetary Rossby wave, discretized with TRiSK (first row) and DGSEM (second row), for refinement in space (first column), and refinement in time (second column). The slope of the best-fit line, s, is shown in each legend.

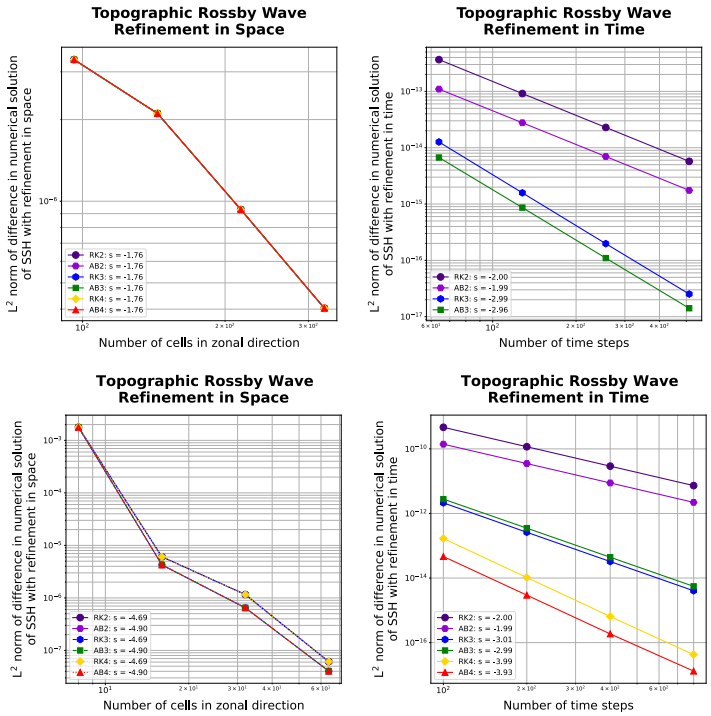

Figure 17. Same as Figure 16, but for TC4a, the linear dispersive topographic Rossby wave.

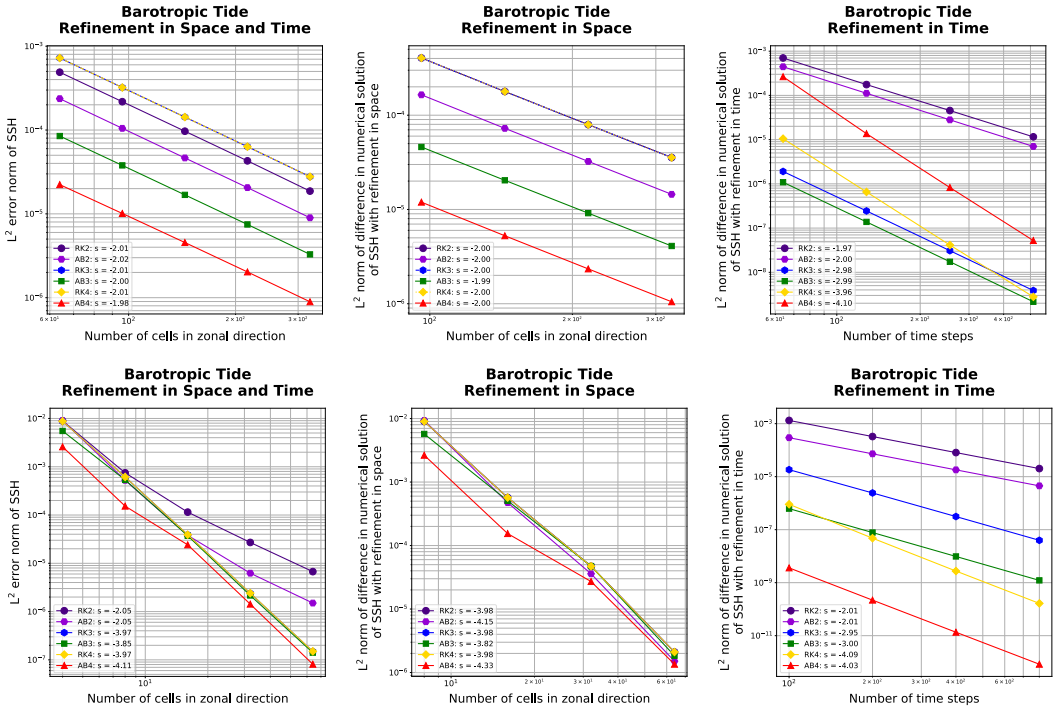

Figure 18. Convergence plots of TC5, the barotropic tide, discretized with TRiSK (first row) and DGSEM (second row), for refinement in space and time (first column), refinement in space (second column), and refinement in time (third column).

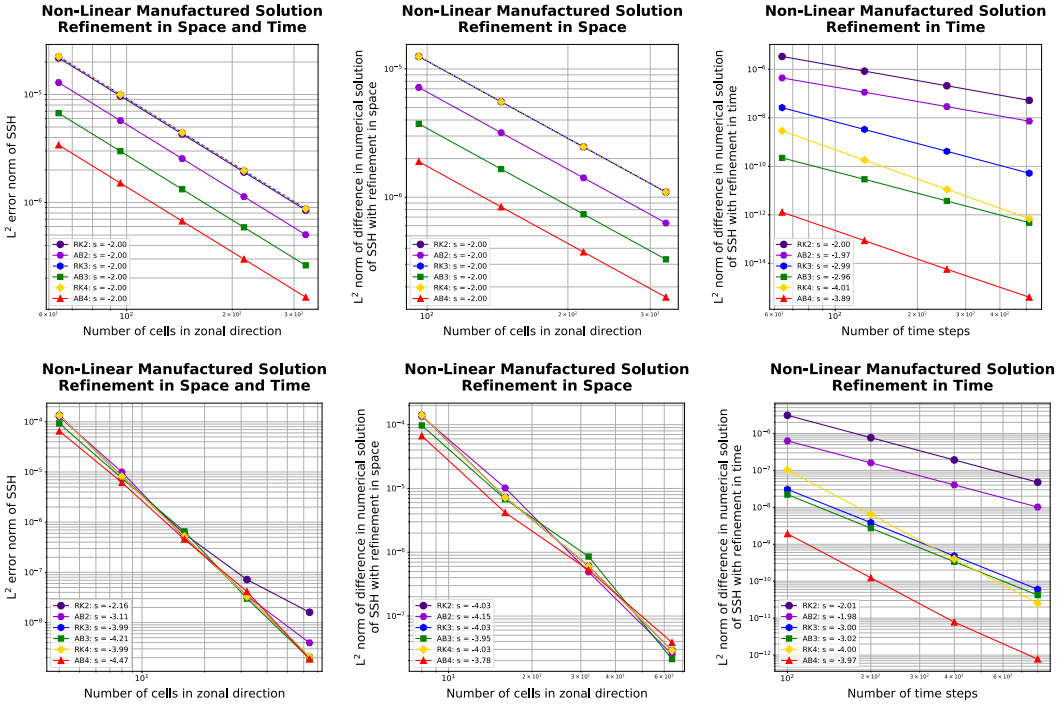

Figure 19. Same as Figure 18, but for TC6, the non-linear manufactured solution.

We have examined the plots produced by DGSEM on low-resolution spectral element meshes. Coarsening was executed by diminishing the polynomial order (p-coarsening) as well as the number of elements (h-coarsening). To maintain brevity, we have opted not to include these results in this paper. However, interested readers can download the output files for each test case detailed in the main paper and in Appendix A from Bishnu (2024a), and review the low p- and h-resolution plots in the designated subdirectories of the DGSEM output directory. These subdirectories exist for all test cases equipped with exact solutions, and contain the numerical solution and error plots. The spectral element mesh used in the low p-resolution simulations was configured with 5 elements and polynomial basis functions of order 4 in each horizontal direction. In contrast, the mesh for the low h-resolution simulations was designed with 2 elements and polynomial basis functions of order 10 in each direction. The low-resolution plots reveal an increase in numerical dispersion and dissipation effects (Section 5). Notably, numerical dispersion often becomes more pronounced in coarser meshes, where the fidelity of the physical phenomena's representation is compromised due to the lower resolution. This manifests as significant alterations in wave speeds and wave shapes, leading to attenuation of the signal in some parts of the domain and amplification in others. While these dispersive effects are imperceptible in the high-resolution DGSEM solution of the physically non-dispersive Kelvin wave, they become conspicuous in the low resolution solution, particularly with lower than three elements and third-order polynomial basis functions in each direction. It alters the phase speed of the component waves of different wavelengths, thereby distorting the resultant wave's initial profile as the simulation progresses. Concurrently, the utilization of the LLF Riemann solver—implemented to dampen spurious oscillations at the spectral elements' boundaries—introduces its own brand of error, that of a dissipative nature. A coarser mesh exacerbates this error, as there are fewer elements to absorb the impact of these dissipative effects. It is manifested by the errors assuming predominantly higher magnitudes along the element boundaries.

Figures 14, 15, 18, and 19 show the convergence plots of the surface elevation error for the coastal Kelvin wave, the inertia-gravity wave, the barotropic tide, and the non-linear manufactured solution, respectively. The refinement is performed by keeping $\Delta t \propto \Delta x$ (first column), only refining in space (second column), and only refining in time (third column). The numerical solutions in the first rows of these figures have been discretized with the TRiSK-based mimetic finite volume method, while the ones in the second row have been discretized with DGSEM. Given the absence of exact solutions for the planetary and topographic Rossby wave test cases, we cannot ascertain their error, which is essential for convergence studies with both spatial and temporal refinement. Consequently, we plot the norm of the differences between numerical solutions over successive pairs of spatial and temporal resolutions, refined at a constant ratio, to verify the spatial and temporal orders of accuracy (Section 4.5). Figures 16 and 17 showcase these convergence plots for the planetary and topographic Rossby waves respectively, discretized with TRiSK (first row) and DGSEM (second row), for refinement only in space (first column) and only in time (second column). For refinement in both space and time, we utilize the Courant number formulation in (61) to first determine the time step Δt on the coarsest mesh, and then reduce this maximum Δt proportional to Δx for the remaining meshes. Similarly, by leveraging (61), we determine (a) the largest Δt at a fixed spatial resolution for refinement only in time, and (b) the Δt on the finest mesh for refinement only in space, ensuring it meets the CFL condition for the remaining meshes where it is also implemented. The time horizon is specified using the largest Δt as stipulated in point 7 of the experimental procedure of Section 6.1. The actual time-stepping methods corresponding to their abbreviated notations in the legends of the convergence plots can be obtained from List 1. The slope of the best fit line for each time-stepping method is denoted by s.

The convergence slopes agree with the theoretical predictions in Bishnu (2021). As highlighted in point 9(c) of the experimental procedure outlined in Section 6.1, employing an exceedingly high-order DGSEM for convergence studies may not be optimal. This is attributed to the prevalence of round-off errors during spatial refinement, which manifest

before the resolutions attain the asymptotic regime. To mitigate this, we only utilize fourth-order polynomial basis functions. The observed convergence slopes of approximately four in the spatial-only refinement plots for DGSEM confirm their fourth-order spatial accuracy. When refining in both space and time, we note that the asymptotic order of convergence matches the minimum of the spatial and temporal orders of accuracy. Since asymptotic convergence is observed with the second-order TRiSK scheme for refinement in both space and time, third- and fourth-order Runge-Kutta and Adams-Bashforth time integrators do not result in higher than second-order convergence rates. For this reason, it is imperative to perform convergence studies only in space and only in time, and plot the differences in the numerical solution or the error between successive pairs of spatial and temporal resolutions to capture the true spatial and temporal orders of accuracy. The second and third columns of Figures 14, 15, 18, and 19 can attest to this statement. The slope s is reported at resolutions where asymptotic convergence is observed. For example, for the coastal Kelvin wave test case discretized in space with a fourth-order DGSEM and advanced with the second-order accurate time stepping methods RK2 and AB2, only second-order accuracy is observed in the asymptotic regime. Similarly, as errors approach machine precision, which often happens with high-order methods, these errors near machine epsilon are excluded from the slope calculations. Finally, we note that when refining in both space and time, the convergence often appears faster than the theoretical asymptotic convergence rate—this occurs, for example, with the coastal Kelvin wave test. In these examples, even though the time stepping methods RK3 and AB3 are third-order accurate, the fourth-order accuracy is observed because the resolutions do not reach the asymptotic regime, and the spatial error dominates at the chosen time step sizes. This underscores yet another important reason for conducting the self-refinement convergence tests only in space and only in time to verify the spatial and temporal orders of accuracy. It is worth noting that for temporal refinement using TRiSK and fourth-order Runge-Kutta and Adams-Bashforth methods, round-off errors overshadow the norm of the solution difference. As such, we have excluded these particular convergence plots from our presentation. Finally, we obtain expected convergence rates with the non-linear planetary and topographic Rossby waves (test cases 3b and 4b), so we do not present these results here.

7 Conclusion and Future Work

We have designed a verification suite of shallow water test cases for ocean model development. Each of these test cases verifies the implementation of a subset of terms in the prognostic momentum and continuity equations e.g. the linear pressure gradient term, the linear constant- or variable-coefficient Coriolis and bathymetry terms, and the non-linear advection terms. The test cases constitute standard geophysical waves including the non-dispersive coastal Kelvin wave, the high-frequency dispersive inertia-gravity wave, the low-frequency dispersive planetary and topographic Rossby waves, the barotropic tide, and a non-linear manufactured solution. Appendix A includes the non-dispersive equatorial Kelvin wave and the dispersive equatorial Yanai, Rossby and inertia-gravity waves, as well as four non-geophysical test cases: the plane Gaussian wave, the diffusion equation, the advection-diffusion equation, and the viscous Burgers' equation.

We have developed a shallow water solver in object-oriented Python (Bishnu, 2024a), employing two types of spatial discretizations—TRiSK representing low-order mimetic finite volume methods (FVMs), and DGSEM epitomizing high-order finite or spectral element methods (SEMs)—and numerous time-stepping methods. It was used as a platform to run the shallow water test cases, and conduct convergence studies for each test case with refinement in both space and time, only in space, and only in time. The observed convergence rates align with the theoretical predictions in Bishnu (2021).

We utilized TRiSK and DGSEM, representing the finite volume and high-order spectral element methods, based on their prevalence in operational ocean models. In our discussion, we highlight key considerations associated with each spatial discretization technique. For

example, we investigate the importance of conducting self-refinement convergence tests only in space and only in time, noting that the rationale might differ between FVMs and SEMs. We further delve into the nuances of numerical implementation, with certain details specific to either FVMs or SEMs. Despite the differences between TRiSK and DGSEM, our study underscores the robustness of our numerical approach in verifying the spatial and temporal orders of accuracy across both discretization methods.

In our analysis of numerical solutions, we discerned that the temporal evolution of errors in both TRiSK and DGSEM closely mirrors the intrinsic physics of the system being modeled. The DGSEM approach, characterized by its use of high-order polynomial basis functions, is more prone to spurious oscillations near steep gradients or discontinuities, a trait commonly dubbed as the "Gibbs phenomenon". Employing Legendre-Gauss nodes in conjunction with the local Lax Friedrichs (LLF) Riemann solver significantly alleviates these oscillations. However, the LLF solver is not without its trade-offs, as it introduces its own flavor of dissipative error. In coarser meshes with fewer elements to absorb these errors, their impact becomes more pronounced, especially at element boundaries. Additionally, DGSEM's susceptibility to numerical dispersion errors is heightened in these coarser meshes due to the physical phenomena being represented with less fidelity. In contrast, the TRiSK scheme, with its inherent dissipation properties, effectively dampens both spurious oscillations and dispersion errors. However, this comes at the expense of overall solution accuracy. In fact, TRiSK's error turns out to be several orders of magnitude larger than DGSEM's at comparable spatial resolution. This is despite the presence of the aforementioned numerical artifacts in DGSEM, which become evident only upon close scrutiny.

It is our hope that the exact solutions and numerical results presented here will be useful to other developers of atmosphere and ocean dynamical cores. Shallow water equation test cases may be applied to ocean layered primitive equation models with the vertical advection and diffusion terms turned off, as well as the barotropic mode in split time-stepping schemes. The suite was designed to include a progressive sequence of added complexity in the terms tested, topography, and boundary conditions. Test cases with exact or manufactured solutions can verify model functionality without resorting to high resolutions and a large number time steps common in global simulations. Moreover, for convergence studies aimed at verifying the spatial and temporal orders of accuracy, the simulation time can be further reduced, leading to an even smaller number of time steps. Such attributes render these test cases ideal for automated nightly regression testing and as a prerequisite for code pull requests. Verification suites with thorough coverage of code functionality have proven to be indispensable in our own development work. In E3SM, we have developed an automated test harness called Polaris that creates the initial conditions, runs the ocean model, and then reports the error and order of convergence for verification test cases (Asay-Davis & Begeman, 2024). Our ongoing and future work include designing further verification exercises with complexity in between the barotropic equations and the primitive equations; stratification and complex bathymetry; the ability to test both the barotropic and baroclinic components separately, and the coupling between these modes.

Appendix A An Additional Suite of Test Cases

We present an additional suite of test cases with exact solutions, summarized in Table A1. Test cases 1–6 in the main text encompass the largest variety of configurations—from linear to non-linear, solid and periodic boundaries, flat and sloping bathymetries, and *f*- and *beta-plane* domains. Though test cases 7–14 expand the suite, they exhibit more repetition in their configurations. The plane wave test case examines the most basic form of the linear shallow water equations, excluding the Coriolis terms. The diffusion, advection-diffusion, and viscous Burgers test cases do not offer solutions to the shallow water equations used to simulate geophysical fluid dynamics. However, the advection-diffusion test case verifies the implementation of the linear advection term, and in conjunction with the diffusion test case, it verifies the implementation of the diffusion term ensuring the numerical stability

of the non-linear shallow water equations. The viscous Burgers test case not only verifies the implementations of the non-linear advection and diffusion terms, it also assesses the resilience of numerical methods against problems with low regularity. Lastly, the equatorial wave test cases (TC 10–13) may appear repetitive in their testing scope, but they hold merit for pedagogical purposes, elucidating the dynamics and visualization of equatorial waves in simplified configurations.

Table A1. Summary of test cases in Appendix A, continuing the case numbering from Table 1 in the main text. The last column refers to terms in the shallow water equations (6).

	Coriolis Parameter	Bottom Topography	Numerical PDE	Boundary Conditions	Terms Verified in Equation (6)
7. Plane Gaussian Wave	Zero (no Coriolis)	Flat Bottom	Linear, Homogeneous, Constant-Coefficient	Non-Periodic in x Non-Periodic in y	(5), (8)
8. Diffusion Eqn	Zero (no Coriolis)	Flat Bottom	Linear, Homogeneous, Constant-Coefficient	Periodic in x Periodic in y	(6)
9. Advection Diffusion Eqn	Zero (no Coriolis)	Flat Bottom	Linear, Homogeneous, Constant-Coefficient	Non-Periodic in x Non-Periodic in y	(6), (8)
10. Viscous Burgers Equation	Zero (no Coriolis)	Flat Bottom	Non-Linear, Homogeneous, Constant-Coefficient	Non-Periodic in x Non-Periodic in y	(1), (2), (6)
11. Equatorial Kelvin Wave	Linear in y (*beta-plane*)	Flat Bottom	Linear, Homogeneous, Variable-Coefficient	Periodic in x Non-Periodic in y	(4), (5), (8)
12. Equatorial Yanai Wave	Linear in y (*beta-plane*)	Flat Bottom	Linear, Homogeneous, Variable-Coefficient	Periodic in x Non-Periodic in y	(4), (5), (8)
13. Equatorial Rossby Wave	Linear in y (*beta-plane*)	Flat Bottom	Linear, Homogeneous, Variable-Coefficient	Periodic in x Non-Periodic in y	(4), (5), (8)
14. Equatorial Inertia Gravity Wave	Linear in y (*beta-plane*)	Flat Bottom	Linear, Homogeneous, Variable-Coefficient	Periodic in x Non-Periodic in y	(4), (5), (8)

A1 Plane Wave, Diffusion, Advection-Diffusion and Viscous Burgers Test Cases

We offer a concise overview of the plane wave, diffusion, advection-diffusion, and viscous Burgers test cases, accompanied by visual representations of the exact solutions' temporal evolution.

A11 Test Case 7: Plane Wave

The plane wave is a solution of the linear homogeneous non-rotating shallow water equations, obtained by specifying $f = 0$ in (10). It only tests the implementation of the linear pressure gradient term in the momentum equations and the linear advection term in the continuity equation. This is the first test case against which the linear shallow water equations should be verified. In a domain with zonal and meridional extents denoted by L_x and L_y, the exact solution for the plane wave can be characterized as a Gaussian, given by

$$\begin{bmatrix} u \\ v \\ \eta \end{bmatrix} = \begin{bmatrix} 1/k_x \\ 1/k_y \\ 1/g \end{bmatrix} \exp\left[-\left\{ \frac{k_x(x - x_0) + k_y(y - y_0) - ct}{\sqrt{2}R_0} \right\}^2 \right], \tag{A1}$$

where (x_0, y_0) are the initial coordinates of the Gaussian peak, (k_x, k_y) are the wavenumber components, R_0 is the RMS width of the Gaussian peak, and $c = \sqrt{gH}$ is the propagation speed of this plane Gaussian wave, equivalent to the shallow water gravity wave speed. For the parameters, we have chosen $L_x = 10^6$ m, $x_0 = 0.25L_x$, $k_x = k_y = 1/\sqrt{2}$ m^{-1}, $g = 10$

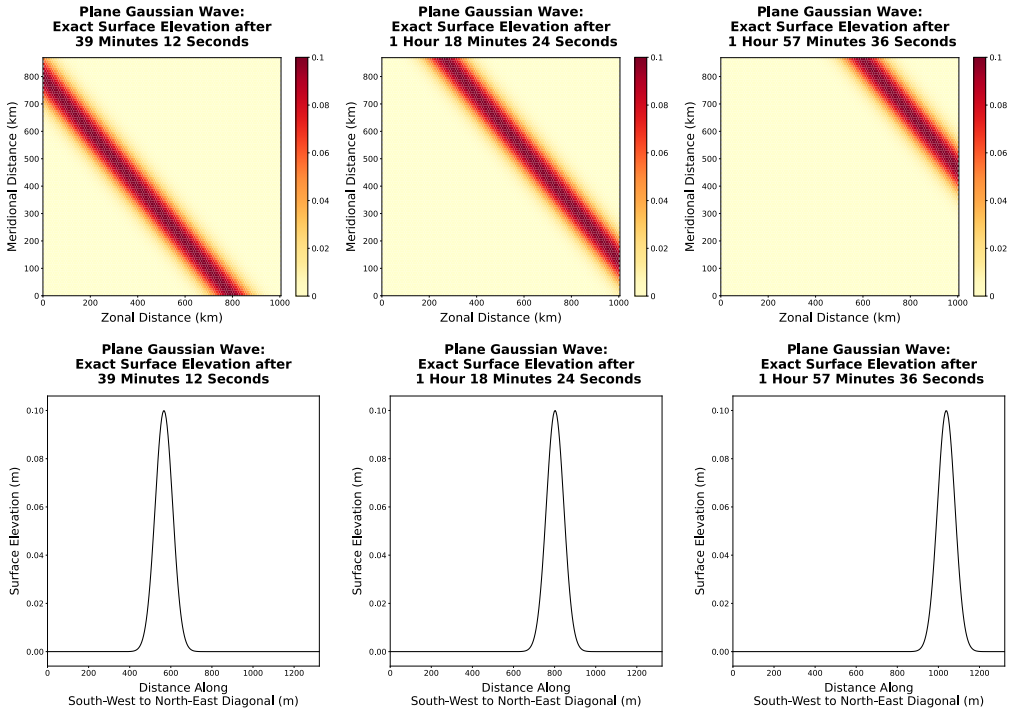

Figure A1. Time evolution of TC7, the plane Gaussian wave, showing the exact surface elevation (first row), and cross-section of the exact surface elevation along the south-west to north-east diagonal (second row).

m s^{-2}, $H = 1000$ m (yielding $c = 100$ m s^{-1}), and $R_0 = w/(2\sqrt{2\ln 2})$, where $w = 10^5$ m denotes the full width at half maximum. For the spectral element mesh, $y_0 = x_0$, and for the MPAS-Ocean mesh, $y_0 = \sqrt{3}/2x_0$. Figure A1 depicts the time evolution of the surface elevation of this plane wave in the entire domain (first row) and along the south-west to north-east diagonal (second row). The error patterns of the non-dispersive Kelvin wave, depicted in Figure 10 of the main paper, resemble this plane wave, as they all travel at the shallow water gravity wave speed.

A12 Test Case 8: Diffusion Equation

The heat or diffusion equation is a fundamental equation in the study of heat transfer and diffusion processes. It describes how a quantity, such as temperature or concentration of a substance, spreads out over time inside a specified region. In two dimensions, the equation is expressed as

$$\varphi_t = \nu \nabla^2 \varphi, \tag{A2}$$

where φ represents the diffusing quantity, and ν is the diffusion coefficient, a measure of the rate at which diffusion occurs. Based on Fick's laws of diffusion, (A2) assumes a homogeneous and isotropic medium, meaning the properties of the medium do not change with direction or position. It essentially states that the rate of change of the scalar field, φ, at any point in space is proportional to the curvature of φ at that point. This reflects the physical principle that diffusion acts to smooth out variations in the scalar field over time. Mathematically, (A2) is an example of a parabolic partial differential equation, and is derived under the assumption of a constant diffusion coefficient and the absence of any sources or sinks within the domain. Standard texts on partial differential equations and numerical analysis, including works by Strauss (2007), J. D. Logan (2014), Farlow

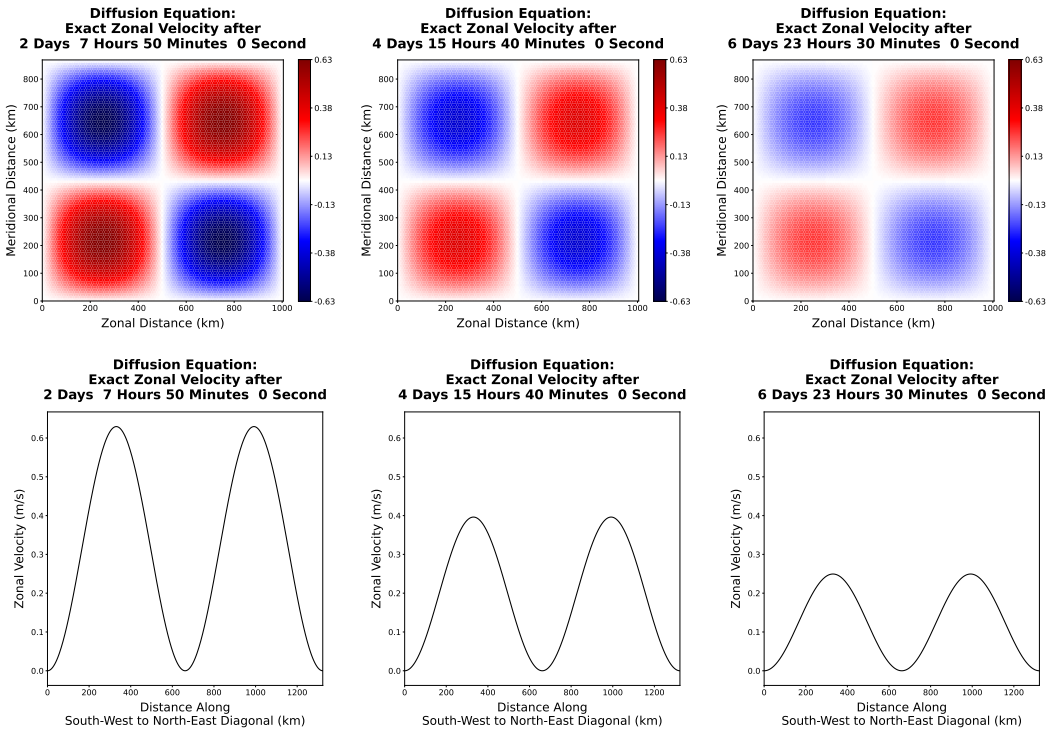

Figure A2. Same as Figure A1 but for TC8, the diffusion equation, showing the exact solution (first row), and cross-section of the exact solution along the south-west to north-east diagonal (second row).

(1993), and Haberman (1998), offer in-depth explorations of this equation. Solving the diffusion equation while employing the spatial discretization of an ocean model verifies the implementation of the Laplacian operator. In our numerical simulations, we employ the exact solution

$$\varphi(x, y, t) = \sin(k_x x) \sin(k_y y) e^{-\kappa t}, \tag{A3}$$

to set the initial and boundary conditions. The diffusivity, $\kappa = \nu \left(k_x^2 + k_y^2\right)$, represents the rate and pattern of diffusion, factoring in the spatial variability of the system. In a domain with a zonal extent of $L_x = 10^6$ m, key parameters include $k_x = 2\pi/L_x$, $k_y = 2\pi/L_y$, and $\nu = 25000$ m^2 s^{-1}. The exact solution's visualization, depicted in Figure A2, showcases the diffusion phenomenon across the entire domain (first row) and along the south-west to north-east diagonal (second row).

A13 Test Case 9: Advection-Diffusion Equation

The advection-diffusion equation models the combined effect of advection and diffusion on a scalar field, φ, such as concentration of a substance or temperature. This equation plays a pivotal role in fields including fluid dynamics, heat transfer, and environmental sciences. Mathematically, the equation is formulated as

$$\varphi_t + \boldsymbol{u}_0 \cdot \nabla\varphi \equiv \varphi_t + \nabla \cdot (\varphi \boldsymbol{u}_0) = \nu \nabla^2 \varphi. \tag{A4}$$

Here, φ is the scalar quantity of interest, $\boldsymbol{u}_0 = u_0 \boldsymbol{i} + v_0 \boldsymbol{j}$ is the velocity field causing advection, and ν is the diffusion coefficient. Comprehensive derivations and solutions of the advection-diffusion equation can be gleaned from standard PDE and numerical analysis texts, such as those by Strauss (2007), Smith (1985), Donea and Huerta (2003), and

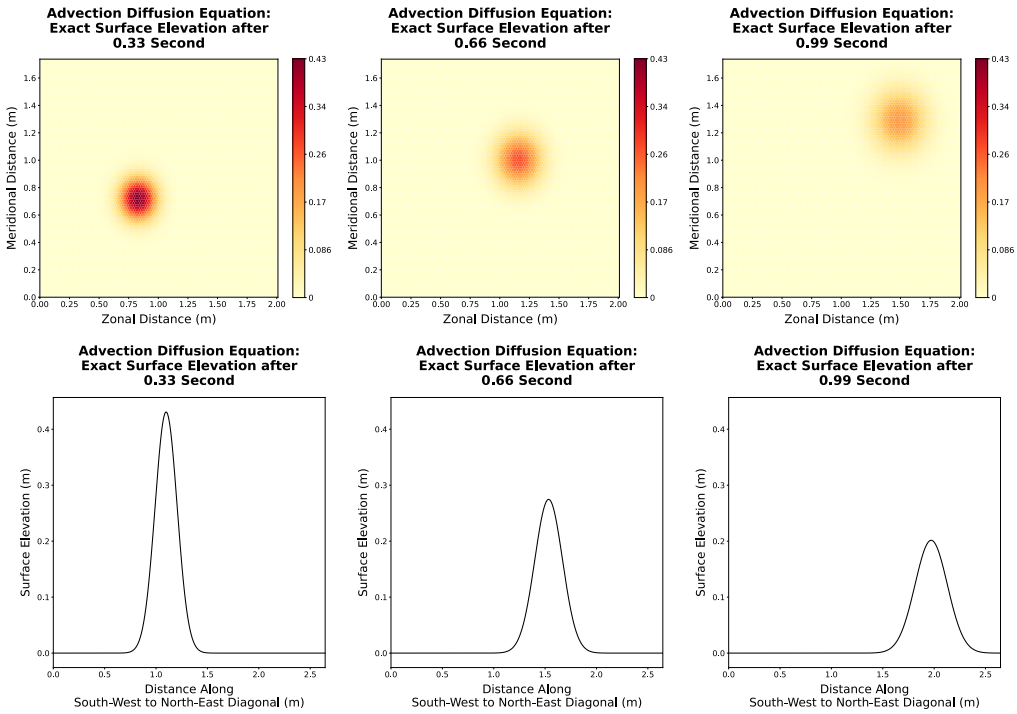

Figure A3. Same as Figure A1 but for TC9, the advection-diffusion equation, showing the exact solution (first row), and cross-section of the exact solution along the south-west to north-east diagonal (second row).

D. A. Kopriva (2009). When the advection-diffusion equation is solved using the spatial discretization of an ocean model, the implementation of the divergence and Laplacian operators can be verified. In our numerical simulations, we employ the exact solution

$$\varphi(x,y,t) = \frac{1}{4t+1}\exp\left[-\frac{\left\{(x-x_0-u_0t)^2+(y-y_0-v_0t)^2\right\}}{\nu(4t+1)}\right], \tag{A5}$$

to specify the initial and boundary conditions. This solution depicts a two-dimensional Gaussian patch with a time-dependent amplitude of $1/(4t+1)$ and a radial RMS width of $\sqrt{\nu(4t+1)/2}$. This patch is advected by the velocity $\boldsymbol{u}_0$ while undergoing diffusion at a rate of ν. The Gaussian's peak is initially located at coordinates $(x_0,\ y_0)$. In a domain with a zonal extent of $L_x = 2$ m, the parameters are chosen as $x_0 = 0.25L_x = 0.5$ m, $u_0 = 1$ m s^{-1}, and $\nu = 0.01$ m^2 s^{-1}. For the spectral element mesh, the parameters y_0, and v_0 mirror their zonal counterparts. In contrast, on the MPAS-Ocean mesh, these parameters are scaled by a factor of $\sqrt{3}/2$ relative to their zonal values. Figure A3 illustrates the exact solution of the advection-diffusion equation with the aforementioned parameters, in the entire domain (first row) and along the south-west to north-east diagonal (second row).

A14 Test Case 10: Viscous Burgers' Equation

The study of hyperbolic PDEs such as the Burgers' equation requires understanding the notion of "characteristics". In the context of the simpler linear advection equation, $u_t + au_x = 0$, the solution is given by $u(x,t) = u_0(x-at)$, where $u_0(x)$ represents the initial condition and a is the advection speed. For this equation, $x - at = c$ (where c takes different values) represents straight lines in the $x-t$ plane called characteristics. Along these characteristics, the solution remains unchanged, effectively signifying that information

propagates without alteration. Transitioning to the inviscid Burgers' equation, the situation becomes non-linear and significantly more complex. Here, the equation reads $u_t + uu_x = 0$ or $u_t + (f(u))_x = 0$, where $f(u) = u^2/2$. A crucial difference is noticed: while in the linear advection equation, the advection speed is constant, in the Burgers' equation, it is dependent on the solution magnitude u itself. This means the characteristics are determined by the local value of the solution, causing them to curve in the $x-t$ plane rather than being straight lines. As the local advection speed u varies across the domain, characteristics either converge or diverge.

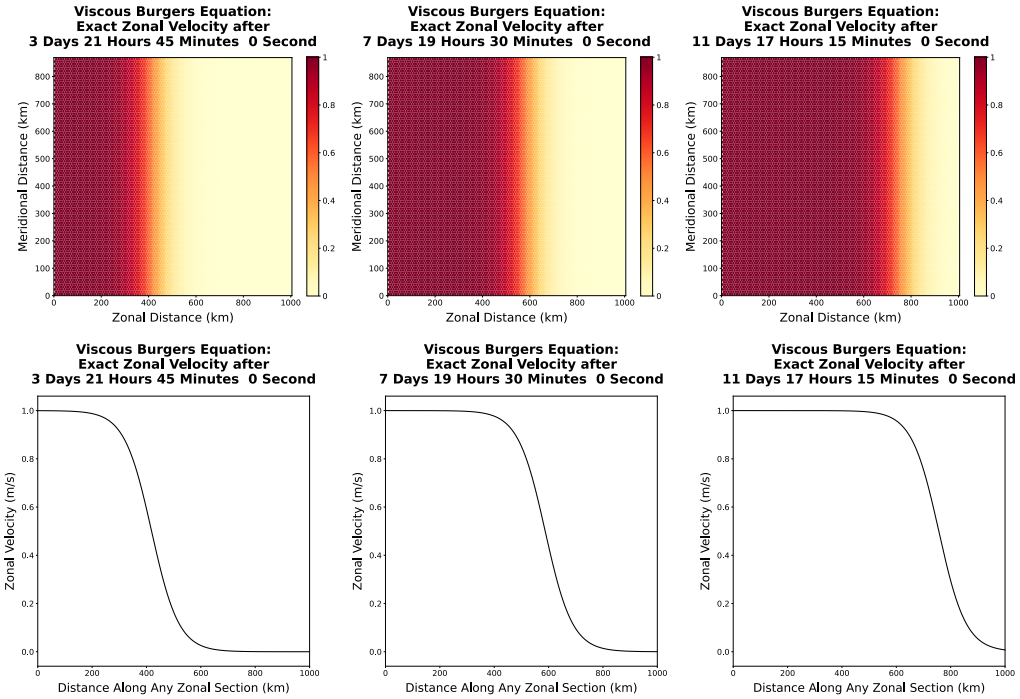

Figure A4. Same as Figure A1 but for TC10, the viscous Burgers' shock wave, showing the exact solution (first row) and cross-section of the exact solution (second row).

The Riemann problem, taken as an example, features a step-like initial condition:

$$u_0(x) = \begin{cases} u_l & \text{if } x < 0, \\ u_r & \text{if } x \geq 0, \end{cases} \tag{A6}$$

where u_l and u_r are constants. Due to the step-like variation, different advection speeds, u_l and u_r respectively, are possessed by the left and right sides. Characteristics are either caused to converge (if $u_l > u_r$) resulting in a shock wave, or to diverge (if $u_l < u_r$) leading to a rarefaction wave. With a smooth initial condition like a Gaussian $u(x, 0) = \exp(-x^2)$, the solution is continuously varying, and so is the local advection speed. Initially, the solution remains single-valued for every x. However, due to the higher magnitude (and thus higher advection speed) at the Gaussian's peak, it starts overtaking its leading edge, causing characteristics to converge. A triple-valued solution at certain x values is encountered, marking the breaking time. Replacing the multi-valued region with a discontinuity by the equal area rule ensures the conservation of the integral of u and sets the shock's position. Meanwhile, at the trailing (left) edge of the Gaussian bump, the characteristics diverge due to a lower advection speed, causing a rarefaction wave to form.

When characteristics converge leading to a shock formation, numerically the solution can become multi-valued in standard discretization schemes. This multi-valuedness is not physically realizable and leads to ambiguity. Numerical methods typically are not designed to handle multi-valued solutions directly. Instead, when faced with a choice among several possible values, the method may inadvertently pick one, leading to an artificially steep gradient. These steep gradients can induce numerical instabilities, particularly in explicit time-stepping schemes, where high gradients can result in time step restrictions (due to the CFL condition) or even solution blow-up. In the case of a rarefaction wave, the characteristics spread apart. Numerically, when modeling a rarefaction wave, the solution remains single-valued and smoother compared to a shock. There is not the same challenge of handling multi-valued solutions. However, if not captured accurately, numerical diffusion, an artifact of many discretization schemes, can overly smooth the rarefaction, making it wider and less pronounced than it should be. This is a common issue, especially in first-order numerical schemes.

We now transition to the viscous Burgers' equation, $u_t + uu_x = \nu u_{xx}$, where ν represents the viscosity or diffusion coefficient. The introduction of this viscous term plays a pivotal role in smoothing out the discontinuities found in the inviscid case. For instance, in the Riemann problem, the introduction of viscosity transforms what would be a shock wave in the inviscid case into a smooth transition in space and time, given by

$$u(x,t) = s - \frac{u_l - u_r}{2} \tanh\left\{\frac{(x - x_0 - st)(u_l - u_r)}{4\nu}\right\}, \tag{A7}$$

where $s = (u_l + u_r)/2$ represents the shock speed, and x_0 denotes the location of the initial discontinuity or transition in the solution. In the context of the inviscid Burgers' equation, s can be derived using the Rankine-Hugoniot jump condition:

$$s = \frac{\text{jump in } f(u)}{\text{jump in } u} = \frac{f(u_l) - f(u_r)}{u_l - u_r} = \frac{u_l^2 - u_r^2}{2\,(u_l - u_r)} = \frac{u_l + u_r}{2}. \tag{A8}$$

As $x \to +\infty$, the hyperbolic tangent function asymptotically approaches 1, ensuring that the solution tends to u_r. Conversely, as $x \to -\infty$, the hyperbolic tangent function gravitates towards -1, and hence the solution aligns with u_l. The term $(x - x_0 - st)(u_l - u_r)$ in the numerator ensures the solution progresses with the appropriate shock speed and correctly accounts for the position and magnitude of the initial discontinuity. When the viscosity ν is allowed to approach zero, the hyperbolic tangent function becomes increasingly sharp. In this limiting scenario, the solution of the viscous Burgers' equation converges to the step function solution that characterizes the inviscid Riemann problem, illustrating the connection between the viscous and inviscid formulations.

Using the viscous Burgers' equation as a verification test for ocean models can be quite advantageous. Ocean models inherently do not encounter shock waves due to viscous terms and numerical diffusion. The viscous Burgers' equation allows these models to verify both their non-linear advection and viscous terms. Moreover, by adjusting the viscosity parameter, we can modulate the solution's regularity, allowing us to closely approach a discontinuous step function and thus robustly test our numerical methods.

Figure A4 displays the exact solution of the viscous Burgers' equation in the entire domain (first row) and along any zonal section (second row). It is uniform in the meridional direction. In case of the TRiSK discretization, the normal velocity is the prognostic quantity of interest. So, we do not lose any generality by using a velocity field with zero meridional component as in this instance. Key parameters include $L_x = 10^6$ m, $x_0 = L_x/4 = 2.5 \times 10^5$ m, $u_l = 1$ m s^{-1}, $u_r = 0$, $s = (u_l + u_r)/2 = 0.5$ m s^{-1}, and $\nu = 2.5 \times 10^4$ m^2 s^{-1}.

A2 Equatorial Waves

Along the equator, the latitude $\phi_0 = 0$, and the Coriolis parameter $f_0 = 2\Omega \sin \phi_0$ vanishes. So, the equator is a dynamically special region. Therefore, in the vicinity of the

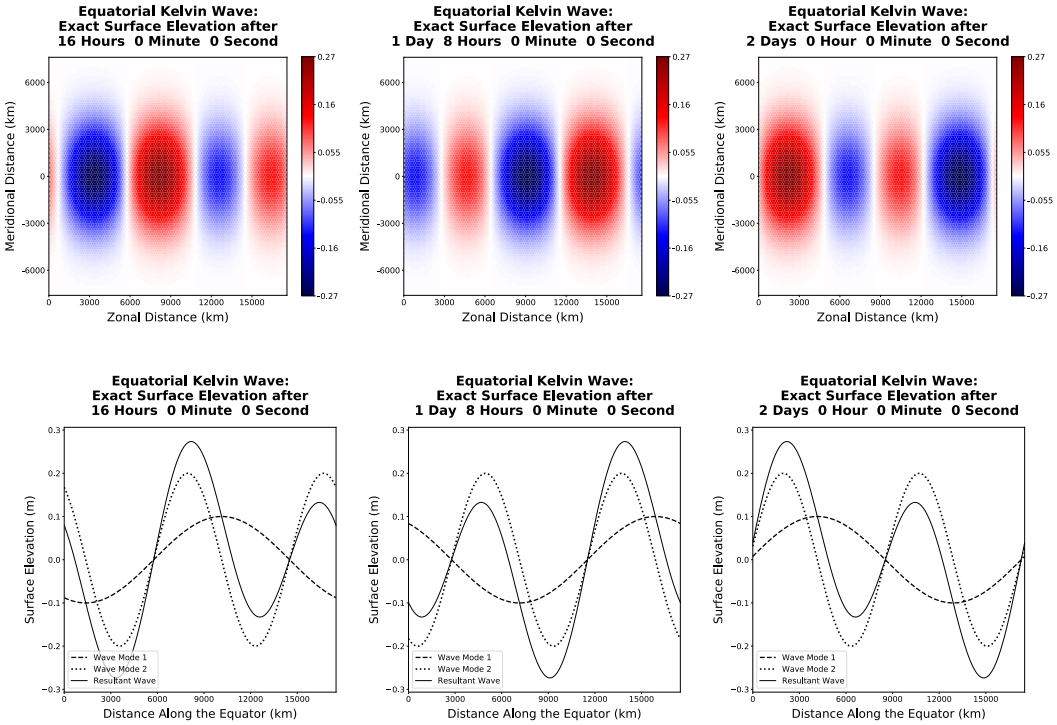

Figure A5. Time evolution of the TC11, the non-dispersive equatorial Kelvin wave, showing the exact surface elevation (first row) and cross-section of the exact surface elevation (second row).

equator, certain geophysical waves develop unusually strong signals and contribute to the generation of the Quasi-Biennial Oscillation (QBO) in the atmosphere (Hell, 2020; Baldwin et al., 2001) and the El Niño Southern Oscillation (ENSO) phenomenon in the ocean and atmosphere (Clarke, 2008; Sarachik & Cane, 2010; Philander et al., 1989).

The equatorial Kelvin, Yanai, Rossby, and inertia-gravity waves are solutions of the rotating shallow water equations

$$u_t - \beta_0 y v = -g\eta_x, \tag{A9a}$$

$$v_t + \beta_0 y u = -g\eta_y, \tag{A9b}$$

$$\eta_t + H\left(u_x + v_y\right) = 0, \tag{A9c}$$

where u and v are the zonal and meridional velocities, η is the surface elevation, H is the mean depth of the ocean with a flat bottom, β_0 is the first-order meridional gradient of the Coriolis parameter, and g is the acceleration due to gravity. Equation (A9) is obtained by replacing f with $\beta_0 y$ in equation (18) of the main paper. Detailed derivations of equatorial wave solutions are found in textbooks specializing in equatorial dynamics (Clarke, 2008) and many geophysical fluid dynamics textbooks (Vallis, 2017; Cushman-Roisin & Beckers, 2011).

A21 Test Case 11: Equatorial Kelvin Wave

The equatorial Kelvin wave is a long gravity wave trapped along the equator with decay scale $\sqrt{2}R_{eq} = (2c/\beta_0)^{1/2}$, where $c = \sqrt{gH}$ is the shallow water gravity wave speed, and R_{eq} is the equatorial Rossby radius of deformation. The equatorial Kelvin wave has zero meridional velocity, and travels eastward at speed c. It is non-dispersive and assumes a

solution of the form

$$\eta = HG(x-ct)\exp\left(-\frac{1}{2}\left(\frac{y}{R_{eq}}\right)^2\right), \tag{A10}$$

$$u = cG(x-ct)\exp\left(-\frac{1}{2}\left(\frac{y}{R_{eq}}\right)^2\right). \tag{A11}$$

In our numerical simulations, we specify

$$G(x-ct) = \hat{\eta}\sin(k(x-ct)) = \hat{\eta}\sin(kx-\omega t) = \hat{\eta}\mathrm{Im}\left(e^{i(kx-\omega t)}\right), \tag{A12}$$

where $\hat{\eta}$ is the amplitude, and the phase speed $\omega/k = c$ is a constant.

Figure A5 displays the time evolution of the equatorial Kelvin wave's surface elevation across the entire domain (first row) with zonal extent $L_x = 1.75 \times 10^7$ m, and along the equator (second row). Similar to our simulations of the coastal Kelvin wave and the inertia-gravity wave in the main paper, we specify the exact solutions to be a superposition of two wave components, where the second component possesses twice the amplitude and wavenumber of the first. Mathematically, $\hat{\eta}^{(2)} = 2\hat{\eta}^{(1)}$ and $k^{(2)} = 2k^{(1)}$, where $\hat{\eta}^{(1)} = 10^{-4}$ m and $k^{(1)} = 2\pi/L_x$. Being non-dispersive in nature, both components, as well as the resultant wave, propagate at an identical phase speed, thereby preserving the initial profile of the resultant wave.

A22 Test Cases 12, 13, and 14: Equatorial Yanai, Rossby, and Inertia-Gravity Waves

The equatorial Yanai, Rossby and inertia-gravity waves can be obtained from the non-dimensional form of (A9),

$$u'_{t'} - y'v' = -\eta'_{x'}, \tag{A13a}$$

$$v'_{t'} + y'u' = -\eta'_{y'}, \tag{A13b}$$

$$\eta'_{t'} + u'_{x'} + v'_{y'} = 0, \tag{A13c}$$

where $u = cu'$, $v = cv'$, $\eta = H\eta'$, $x = \sqrt{c/\beta_0}x'$, $y = \sqrt{c/\beta_0}y'$, and $t = 1/\sqrt{\beta_0 c}t'$. Dropping the primes for notational convenience, the non-dimensional meridional velocity of the dispersive equatorial Yanai, Rossby and inertia-gravity waves can be expressed in modal form as

$$v = \mathrm{Re}\left(e^{i(kx-\omega t)}\psi_m(y)\right) = \cos(kx-\omega t)\psi_m(y), \tag{A14}$$

where the Hermite function $\psi_m(y)$ is

$$\psi_m(y) = \frac{e^{-y^2/2}H_m(y)}{\sqrt{2^m m!\sqrt{\pi}}}, \tag{A15}$$

with $H_m(y)$ being the m^{th}-order Hermite polynomial. Since $H_m(y)$ is an odd function of y for odd m and an even function of y for even m, so is $\psi_m(y)$. The Hermite function $\psi(y)$ satisfies

$$\frac{d^2\psi_m}{dy^2} + \left(\omega^2 - k^2 - \frac{k}{\omega} - y^2\right)\psi \equiv \frac{d^2\psi_m}{dy^2} + \left(2m+1-y^2\right)\psi = 0, \quad m = 0, 1, \ldots, \tag{A16}$$

with the non-dimensional dispersion relation being

$$k^2 + \frac{k}{\omega} - \omega^2 + (2m+1) = 0, \quad m = 0, 1, \ldots. \tag{A17}$$

From (A16), it can be seen that $\psi_m(y)$ is oscillatory for $|y| < \sqrt{2m+1}$ and monotonically decaying for $|y| > \sqrt{2m+1}$. Since the nature of $\psi_m(y)$ changes at $y = \sqrt{2m+1}$, it is referred to as the turning latitude for mode m. Solving the quadratic equation (A17) in k,

$$k = -\frac{1}{2\omega} \pm \sqrt{\omega^2 + \frac{1}{4\omega^2} - (2m+1)}. \tag{A18}$$

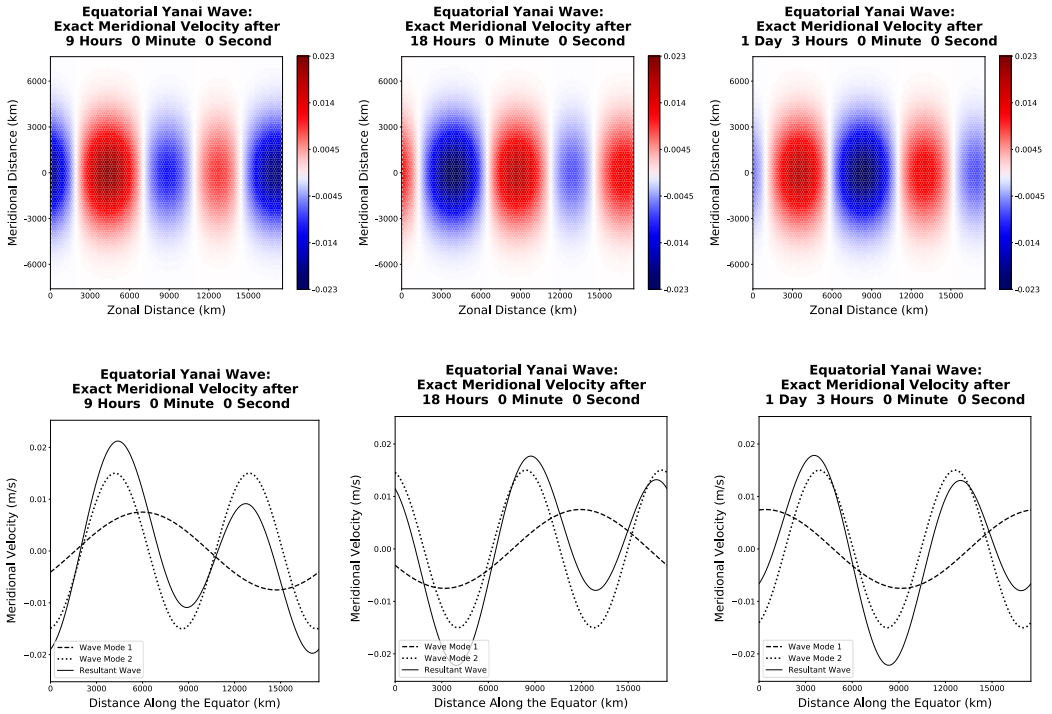

Figure A6. Time evolution of the TC12, the dispersive equatorial Yanai wave, showing the exact meridional velocity (first row) and cross-section of the exact meridional velocity along the equator (second row).

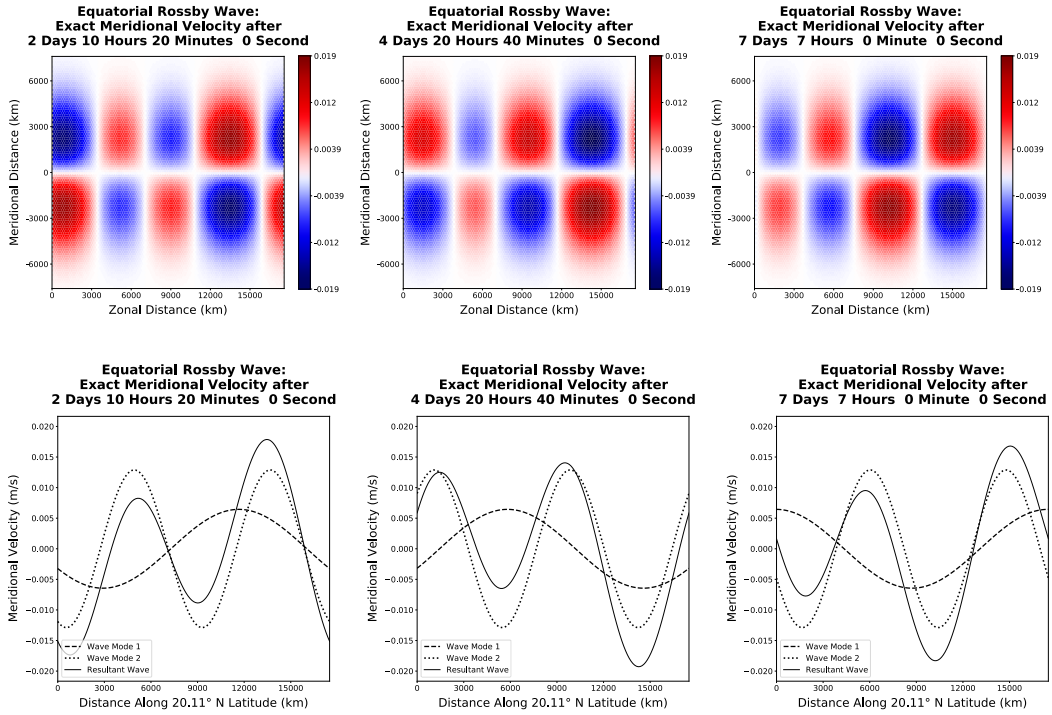

Figure A7. Time evolution of the TC13, the dispersive equatorial Rossby wave, showing the exact meridional velocity (first row) and cross-section of the exact meridional velocity along the 20.11°N latitude with maximum magnitude of the Hermite function $\psi_1(y)$ (second row).

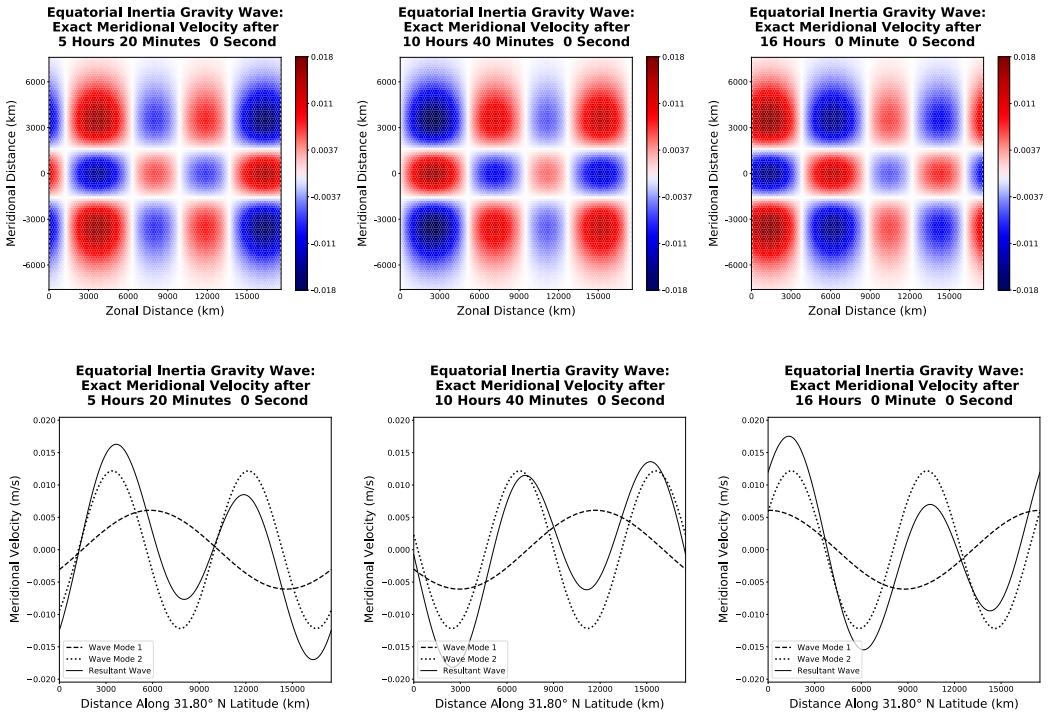

Figure A8. Time evolution of the TC14, the dispersive equatorial inertia-gravity wave, showing the exact meridional velocity (first row) and cross-section of the exact meridional velocity along the 31.80°N latitude with maximum magnitude of the Hermite function $\psi_2(y)$ (second row).

When $m = 0$, the roots are $k = \omega - 1/\omega$ and $k = -\omega$, both of which are real. The root $k = -\omega$ corresponds to a westward propagating Kelvin wave with unbounded velocity at large distances from the equator, and is therefore not a viable solution. The other root $k = \omega - 1/\omega$ gives rise to a Yanai or 'mixed' Rossby gravity wave with meridional velocity

$$v = \exp\left(i\left(\omega - \frac{1}{\omega}\right)x - \omega t\right)\psi_0(y). \tag{A19}$$

When the discriminant $\omega^2 + 1/\left(4\omega^2\right) - (2m+1) > 0$ and $m \geq 1$, both roots of (A18) are real and result in acceptable wave fields. But depending on the magnitude of ω, these waves can belong to one of two categories: low-frequency Rossby waves for small ω, or high-frequency inertia-gravity waves for large ω.

Equation (A18) expresses the wave number, k, in terms of the angular velocity, ω. Alternatively, the angular velocity, ω, corresponding to a particular wave number, k, can be determined by solving the non-linear equation

$$\mathcal{F}(\omega) \equiv \omega^3 - (k^2 + 2m + 1)\omega - k = 0, \tag{A20}$$

which is a variant of (A17). We use the Newton-Raphson method to solve (A20), and specify the magnitude of the initial guess for ω to be close to zero for the low-frequency equatorial Rossby wave and greater than one for the high-frequency equatorial inertia-gravity wave.

The non-dimensional zonal velocity and surface elevation are

$$u = \mathrm{Re}\left(\frac{k\frac{d\psi_m}{dy} - \omega y\psi_m}{k^2-\omega^2} ie^{i(kx-\omega t)}\right) = \frac{k\frac{d\psi_m}{dy} - \omega y\psi_m}{\omega^2-k^2}\sin(kx-\omega t), \tag{A21}$$

$$\eta = \mathrm{Re}\left(\frac{\omega\frac{d\psi_m}{dy} - ky\psi_m}{k^2-\omega^2} ie^{i(kx-\omega t)}\right) = \frac{\omega\frac{d\psi_m}{dy} - ky\psi_m}{\omega^2-k^2}\sin(kx-\omega t). \tag{A22}$$

Figures A6 through A8 showcase the meridional velocity of the equatorial Yanai, Rossby, and inertia-gravity waves. As with previous demonstrations, we define the exact solutions for these equatorial waves as a combination of two wave components, wherein the second component possesses twice the amplitude and wavenumber of the first. Mathematically, $\hat{\eta}^{(2)} = 2\hat{\eta}^{(1)}$ and $k^{(2)} = 2k^{(1)}$, where $\hat{\eta}^{(1)} = 10^{-4}$ m, $k^{(1)} = 2\pi/L_x$, and $L_x = 1.75 \times 10^7$ m. The first row of these figures portrays the equatorial wave across the entire domain, while the second row focuses on a segment of the resultant wave solution and its components along the latitude characterized by the peak magnitude of the Hermite function, $\psi_m(y)$. Due to the dispersive nature, these components propagate at different phase speeds causing the resultant wave profile to alter over time. For the equatorial Yanai wave (Figure A6) and inertia-gravity wave (Figure A8), we specify $m = 0$ and $m = 2$, so that the Hermite functions $\psi_0(y)$ and $\psi_2(y)$ are even, and therefore the solution is symmetric across the equator. For the equatorial Rossby wave (Figure A7), we specify $m = 1$, so that the Hermite function $\psi_1(y)$ is odd, and therefore the solution is antisymmetric across the equator. Moreover, $\psi_0(y)$, $\psi_1(y)$, and $\psi_2(y)$ attain their maximum magnitudes at $y = 0$, $y = \pm 1$, and $y = \pm\sqrt{2.5}$. After multiplying by the length scale $\sqrt{c/\beta_0}$, and dividing by the radius of the Earth, these non-dimensional values of y correspond to the 0° latitude or the equator (second row of Figure A6), the 20.11°N and S latitudes (second row of Figure A7), and the 31.80°N and S latitudes (second row of Figure A8).

A3 Numerical Results

We begin this section by addressing the time step limitations inherent to the numerical simulation of the diffusion, advection-diffusion and viscous Burgers' equations. The parabolic nature of these equations, resulting from the diffusion term, necessitates a more restrictive time step. Drawing from the Von Neumann stability analysis of the linear diffusion equation, we define the diffusive time step on a two-dimensional spatial domain as

$$\Delta t_{\text{diffusive}} = \begin{cases} \dfrac{1}{2\nu\left(\frac{1}{\Delta x^2} + \frac{1}{\Delta y^2}\right)} & \text{for TRiSK,} \\ \dfrac{1}{2\nu\left(\frac{P_x^2}{\Delta x^2} + \frac{P_y^2}{\Delta y^2}\right)} & \text{for DGSEM.} \end{cases} \tag{A23}$$

Here, ν symbolizes the diffusion coefficient, while Δx and Δy represent the widths of the cell (or element). On a uniform TRiSK mesh with hexagonal cells, we can set $\Delta y = \sqrt{3}/2\Delta x$. In the context of DGSEM, P_x and P_y signify the polynomial orders in the two horizontal directions. Based on (59)—(61) in the main paper, we define the advective time step to be

$$\Delta t_{\text{advective}} = \begin{cases} \dfrac{C}{\frac{c_x}{\Delta x} + \frac{c_y}{\Delta y}} & \text{for TRiSK,} \\ \dfrac{C}{\frac{c_x P_x^2}{\Delta x} + \frac{c_y P_y^2}{\Delta y}} & \text{for DGSEM.} \end{cases} \tag{A24}$$

In the equations above, C represents the Courant number. For the advection-diffusion equation, we specify $c_x = u_0$ and $c_y = v_0$. Similarly, for the viscous Burgers' equation, we set $c_x = \max(|u_l|, |u_r|)$ and $c_y = 0$. The actual time step is specified as $\Delta t = \Delta t_{\text{diffusive}}$ for

the diffusion equation and $\Delta t = \min\left(\Delta t_{\text{advective}}, \Delta t_{\text{diffusive}}\right)$ for the advection-diffusion and viscous Burgers' equations.

We present the numerical results, showcasing error plots and their temporal evolution. Figures A9 to A12 display the surface elevation errors for the plane Gaussian wave, the diffusion and advection-diffusion equation solutions, and the zonal velocity error of the viscous Burgers shock wave. Subsequently, Figures A13 to A16 depict the temporal evolution of the surface elevation error of the equatorial Kelvin wave, as well as the meridional velocity error for equatorial Yanai, Rossby, and inertia-gravity waves. The zonal extent of the rectangular domain for each test case is specified as follows: $L_x = 10^6$ m, 10^6 m, 2 m, 10^6 m, and 1.75×10^7 m for the plane Gaussian wave, the diffusion equation, the advection-diffusion equation, the viscous Burgers' equation, and the equatorial waves respectively. As for the meridional extent, it is defined by $L_y = \sqrt{3}/2 L_x$ for TRiSK, and by $L_y = L_x$ for DGSEM. In each horizontal direction, the planar hexagonal TRiSK mesh comprises $N = 100$ cells, and the spectral element mesh consists of $N = 5$ elements. The distance between the hexagonal cell centers of the TRiSK mesh, given by $\Delta x = L_x/N$, represents the zonal cell width, and $\Delta y = \sqrt{3}/2\Delta x$ provides a measure for the meridional cell width. Meanwhile, for the spectral element mesh, the side lengths are equal in both directions: $\Delta x = L_x/N$. The smallest grid spacings near the element boundaries approximate to $\Delta x/P^2$, with $P = 10$ indicating the order of the polynomial basis functions and the spatial order of accuracy of our DGSEM. For all test cases, we target an advective Courant number close to 0.5. For the diffusion equation, we choose the diffusive time step, and for the advection-diffusion and viscous Burgers test cases, we select the minimum between the advective and diffusive time steps, as elaborated in the preceding paragraph. When modeled with TRiSK, this leads to time step sizes of $\Delta t = 16$ s, 750 s, 5×10^{-3} s, 750 s, 900 s, 450 s, 1200 s, and 300 s for the plane Gaussian wave, the diffusion equation, the advection-diffusion equation, the viscous Burgers' equation, and the equatorial Kelvin, Yanai, Rossby, and inertia-gravity waves respectively. With DGSEM, the respective time steps for these cases are set at 3.5 s, 40 s, 4×10^{-4} s, 30 s, 180 s, 90 s, 240 s, and 60 s.

The first row of Figures A9—A16 demonstrates the error yielded by the second-order accurate TRiSK-based finite volume method. In contrast, the second row illustrates the error from the 10^{th}-order accurate DGSEM. As anticipated, the TRiSK error is a few orders of magnitude smaller, and the DGSEM error is several orders of magnitude smaller than the solution magnitude. As observed in our main paper's test case simulations, the error plots resonate with the intrinsic physics of the system. For example, the error associated with the plane wave propagates at the same phase speed as the solution, mirroring the speed of a shallow water gravity wave. In the TRiSK-based mimetic finite volume method, spurious reflections observed at domain boundaries are likely due to the implementation of Dirichlet boundary conditions that do not fully capture the characteristics of the incoming wave. The method involves updating the normal velocities at the boundary edges of the hexagonal mesh using exact solution values, whereas the normal velocities at the interior edges and the surface elevation at cell centers are updated prognostically through numerical gradient and divergence and formulations respectively. However, without direct boundary constraints on surface elevation, discrepancies can arise during wave-boundary interactions. In contrast, DGSEM updates zonal and meridional velocities as well as surface elevation at the interior Gauss quadrature points of each element, with tendencies computed from both interior fluxes at the quadrature points and numerical fluxes at the element's edges. Moreover, DGSEM applies the exact solution as the external state at boundary edges, offering a more accurate wave representation and minimizing reflections, aided by the dissipative properties of the LLF Riemann solver at these edges. This distinction in boundary treatment between the methods helps explain the observed differences in wave reflection.

Given that the error magnitude is contingent on the exact solution and its gradients, pronounced errors in regions characterized by high spatial gradients are unsurprising. This is most prominent for the plane Gaussian wave error (both TRiSK and DGSEM), and the

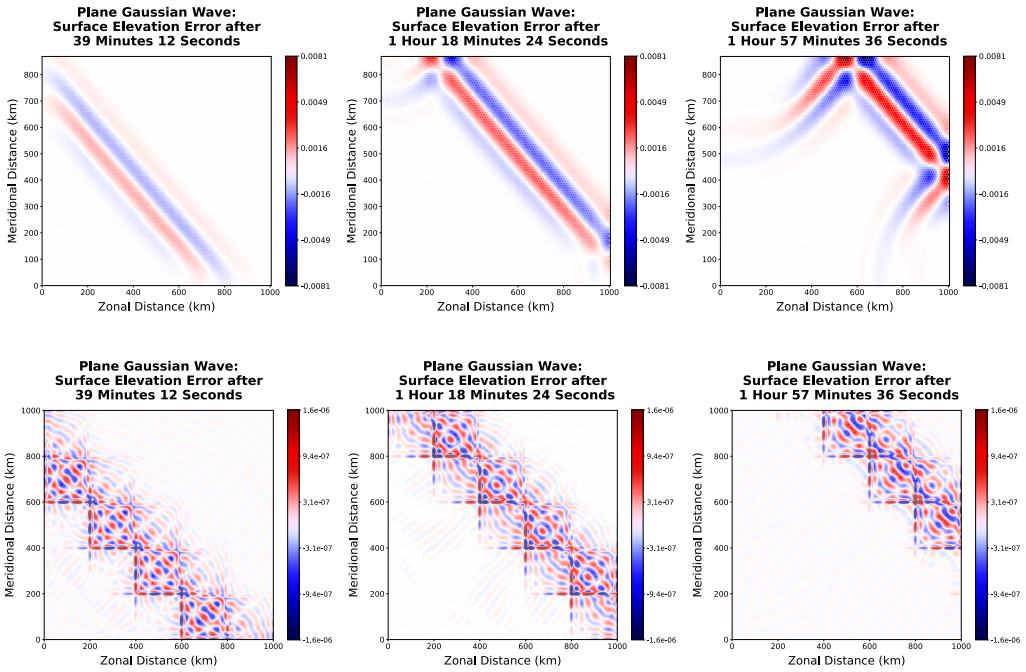

Figure A9. Time evolution of the surface elevation error of TC7, the plane Gaussian wave, spatially discretized with the TRiSK-based mimetic finite volume method (first row), and DGSEM using 5 elements and polynomial basis functions of order 10 in each horizontal direction (second row).

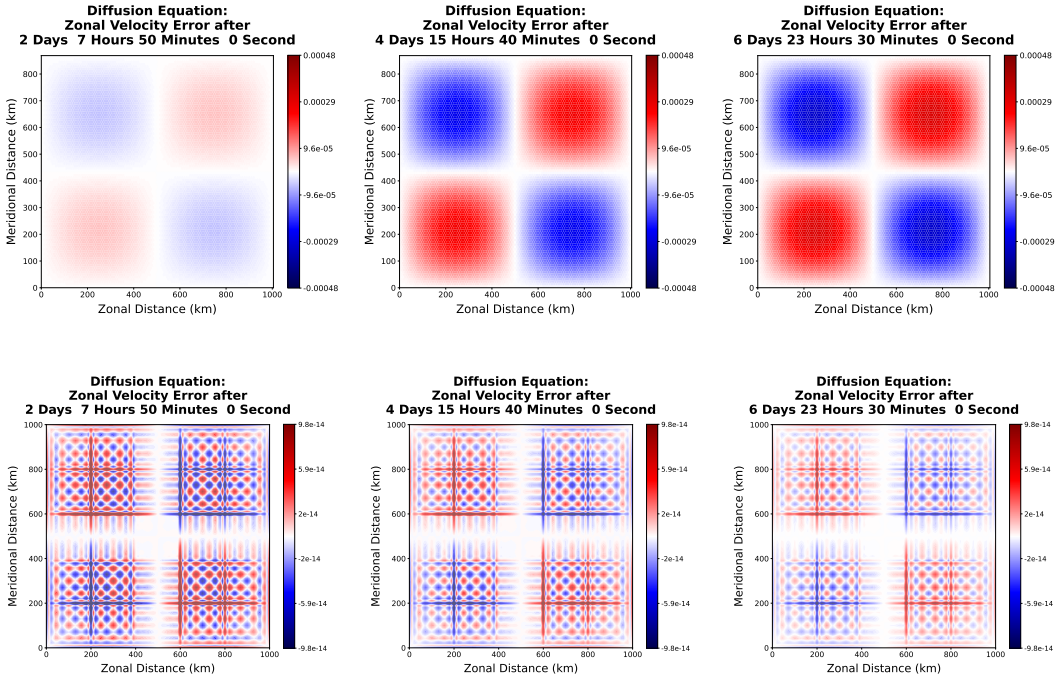

Figure A10. Same as Figure A9 but for TC8, the diffusion equation, showing error for TRiSK (first row) and DGSEM (second row).

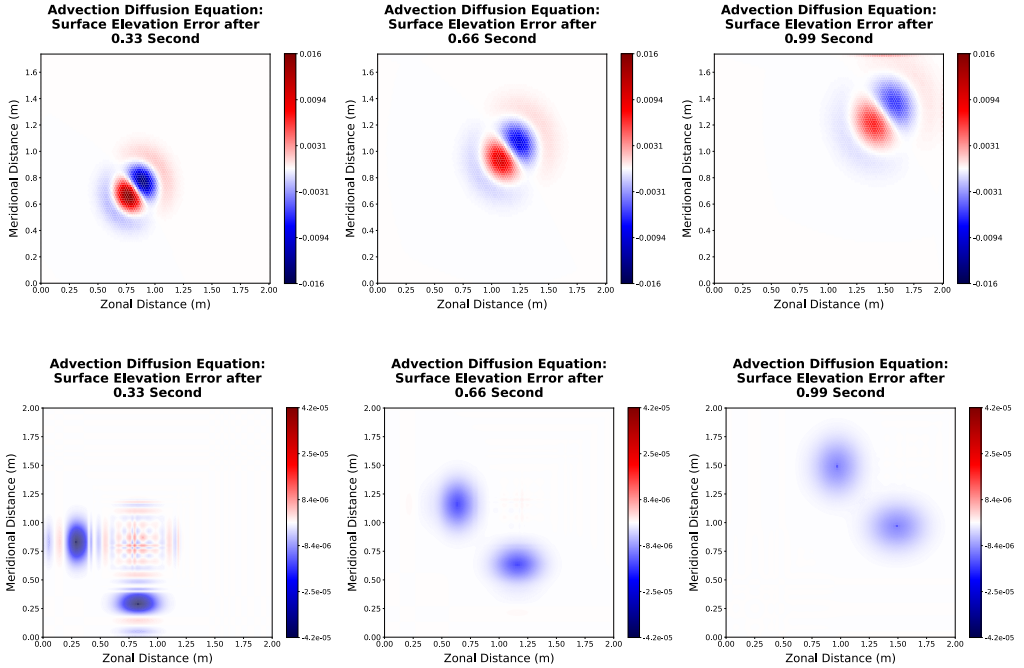

Figure A11. Same as Figure A9 but for TC9, the advection-diffusion equation, showing error for TRiSK (first row) and DGSEM (second row).

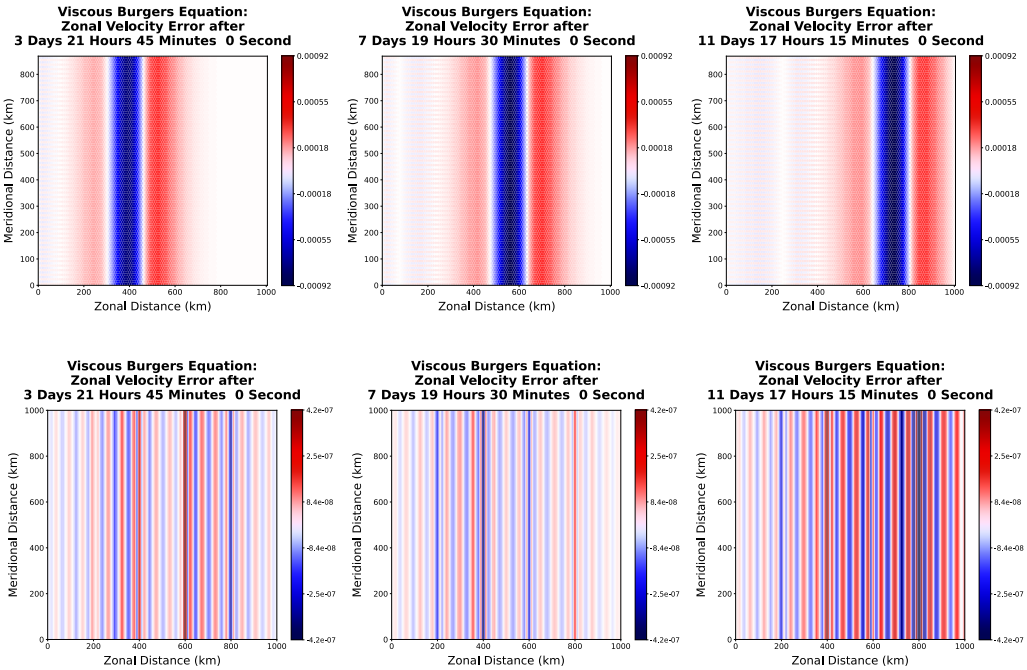

Figure A12. Same as Figure A9 but for TC10, the viscous Burgers shock wave, showing error for TRiSK (first row) and DGSEM (second row).

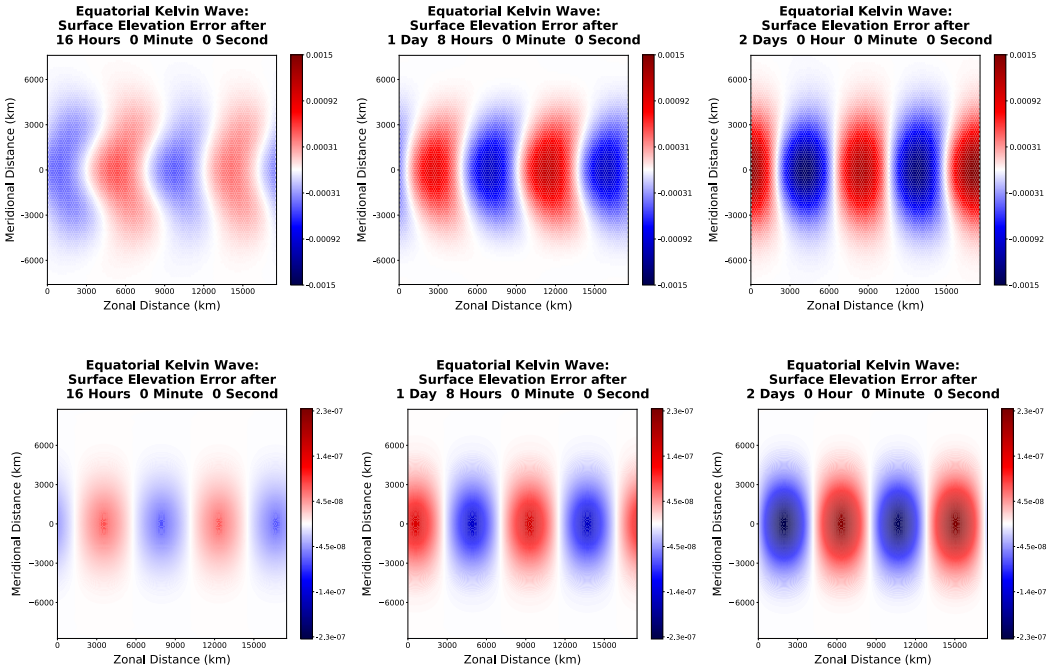

Figure A13. Time evolution of the surface elevation error of TC11, the non-dispersive equatorial Kelvin wave, spatially discretized with TRiSK (first row) and DGSEM (second row).

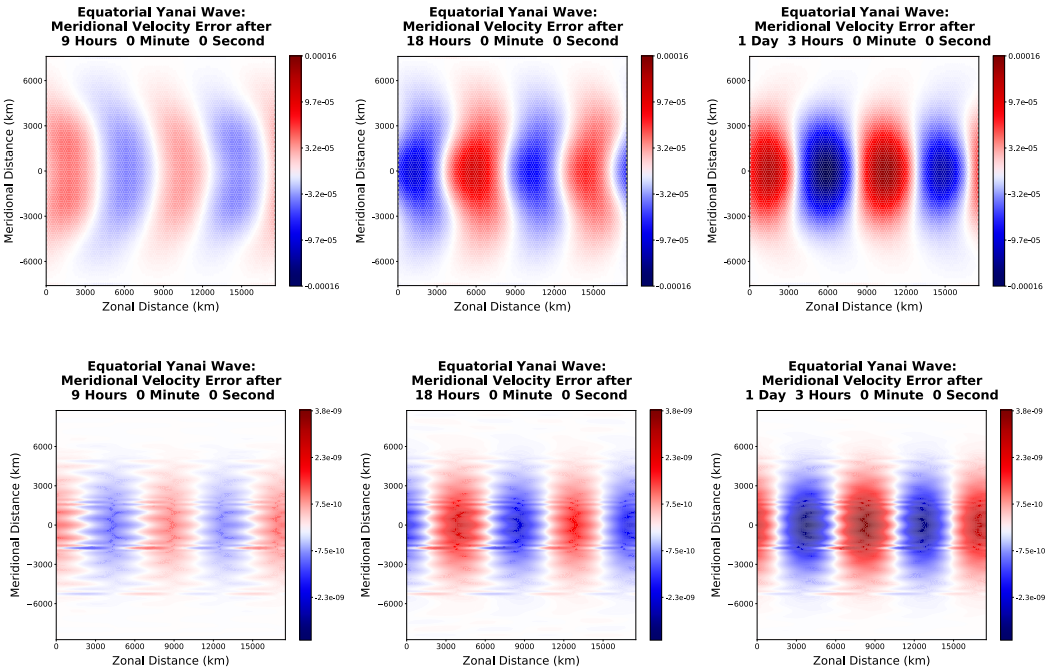

Figure A14. Same as Figure A13 but for TC12, the dispersive equatorial Yanai wave, showing the meridional velocity error for TRiSK (first row) and DGSEM (second row).

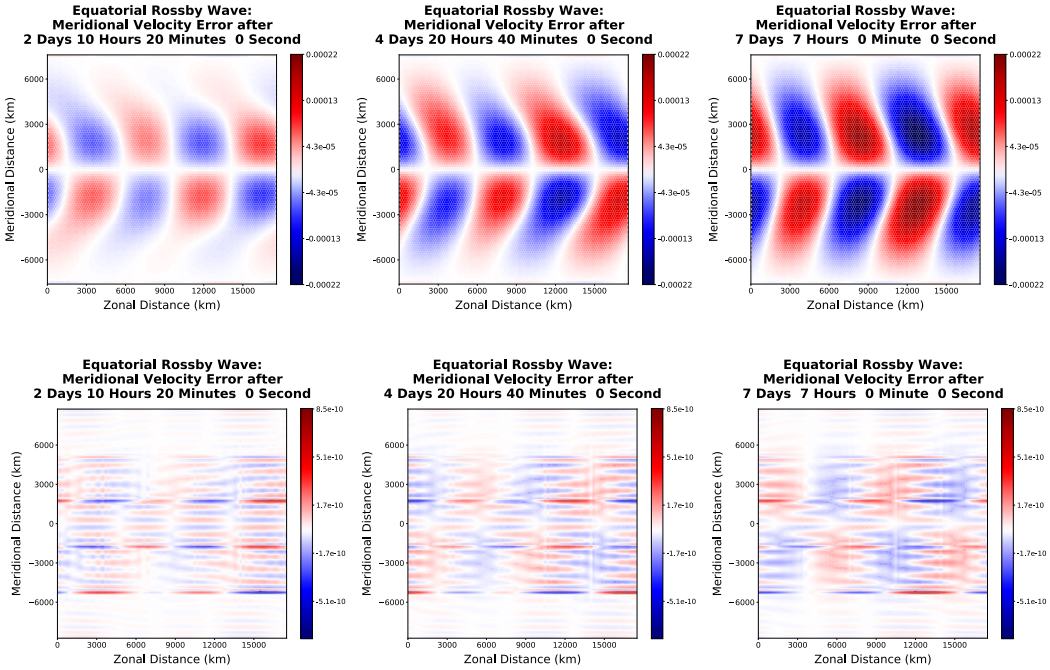

Figure A15. Same as Figure A13 but for TC13, the dispersive equatorial Rossby wave, showing the meridional velocity error for TRiSK (first row) and DGSEM (second row).

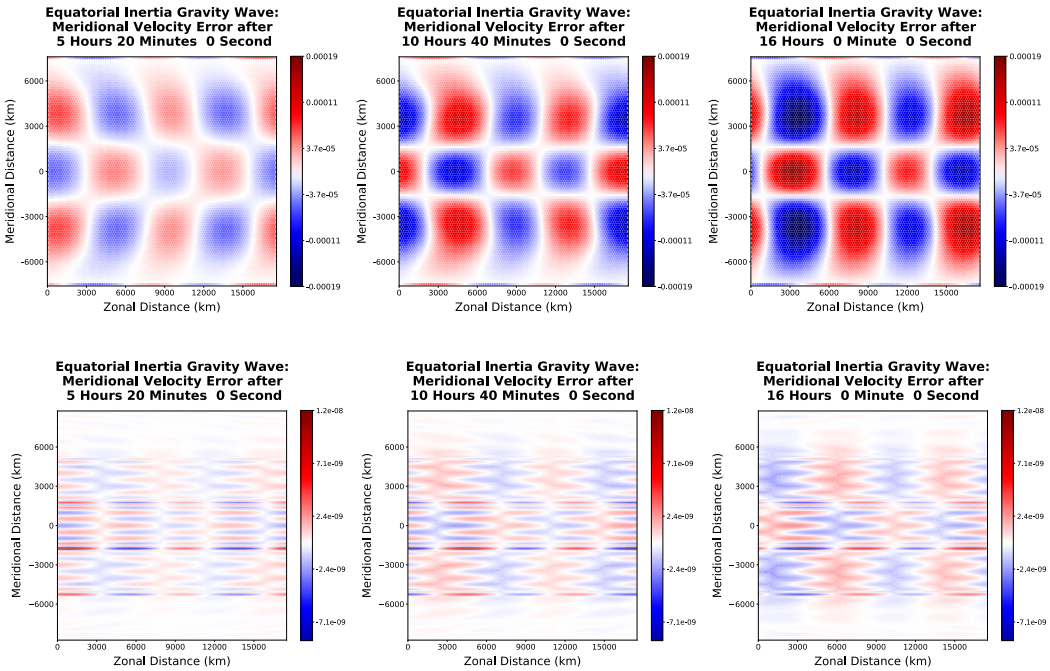

Figure A16. Same as Figure A13 but for TC14, the dispersive equatorial inertia-gravity wave, showing the meridional velocity error for TRiSK (first row) and DGSEM (second row).

TRiSK error for the diffusion, advection-diffusion, and viscous Burgers' equations. The DGSEM errors manifest in various forms, including numerical dispersion and dissipation, and spurious oscillations (Section 5). The setup for the viscous Burgers' equation amplifies the numerical dispersion and spurious oscillations (Figure A12), especially when compared to linear test cases like the barotropic tide. The dispersive errors traverse element boundaries and exit the domain at velocities surpassing that of the shock wave. For the equatorial Kelvin, Yanai, Rossby, and inertia-gravity waves, the inherent dissipation of the mimetic TRiSK scheme largely curtails the dispersive error prevalent in the DGSEM error. We again encourage interested readers to access low p- and h-resolution DGSEM solution plots from Bishnu (2024a), which reveal increased numerical dispersion and dissipation, although spurious oscillations are not as prevalent. This observation is attributed to the deployment of the LLF Riemann solver, whose primary function is to suppress such oscillations at the edges of spectral elements. However, this solver introduces its own dissipative error, which becomes more noticeable in coarser meshes where fewer elements are available to absorb it, leading to visibly enhanced errors at element boundaries. Despite not affecting the spatial order of accuracy (Section 5.1), the global pattern of this dissipative error unveils the element boundaries, revealing the spectral elements' positions in the mesh. This, in conjunction with the linear scaling of the color bars, rendering any error of magnitude lower than the dominant error nearly invisible, can create the impression of mesh effects in the plots (Figures A9 and A10). Numerical dispersion is accentuated in the coarser meshes due to less accurate representation of the physical phenomena at a given scale. For instance, the equatorial Kelvin wave, akin to its coastal counterpart, exhibits no physical dispersion. However, when simulated with less than three elements and third-order polynomial basis functions in each horizontal direction, numerical dispersion significantly alters the phase speed across varying wavelengths, which in turn, distort the shape of these physically non-dispersive Kelvin waves as the simulation unfolds.

Appendix B Problem of Multiple Time Scales and Barotropic-Baroclinic Splitting in Ocean Models

In this section, we highlight the applicability of shallow water test cases within the context of baroclinic-barotropic splitting in an ocean model. We initiate our discussion with the challenge of multiple time scales inherent in ocean models, elucidating how the splitting approach can effectively address this complication and boost computational efficiency. As a practical example of the splitting procedure, we derive the barotropic and baroclinic equations from the governing equations of MPAS-Ocean. We then demonstrate that the barotropic equations assume the form of inhomogeneous rotating shallow water equations.

Numerical ocean circulation models typically admit motions varying on a wide range of time scales. For instance, the fast external gravity waves, approximately independent of depth, propagate at a speed of $\mathcal{O}\left(100\ \mathrm{ms}^{-1}\right)$. On the other hand, the major current systems and internal gravity waves exhibit velocities of $\mathcal{O}\left(1\ \mathrm{ms}^{-1}\right)$ i.e. two orders of magnitude less. This vast disparity of time scales imposes a tremendous constraint on numerically modelling oceanic phenomena. For explicit time-stepping methods, the CFL condition states that, for a given Courant number, the maximum permissible time step of a hyperbolic system should be inversely proportional to the wave speed to attain a numerically stable solution (see, e.g. Griffies et al. (2005, Section 12.8). Therefore, the presence of external gravity waves forces the time step to be much smaller than what is required to resolve the internal gravity waves. Solving the full three-dimensional momentum equations with the smallest time step dictated by the CFL condition of the fastest waves is computationally impractical, as running a global simulation at high resolution (10 km grid cells or smaller) would require time steps on the order of minutes. While restrictions of the time step size can be addressed by using an implicit method, this would require solving a system of non-linear equations at every time step thereby compensating for the reduction in computational time achieved by increasing the time step size. A traditional alternative is to split the governing equations

into two subsystems: a barotropic one for solving the fast depth independent motions and a baroclinic one for solving the much slower depth dependent motions, as described in Griffies et al. (2005); T. Ringler et al. (2013). Being independent of the vertical coordinate, the fast barotropic subsytem is two-dimensional and the computational cost involved in solving it, either explicitly using a small time step or implicitly using a large time step, is drastically reduced. The full three-dimensional baroclinic subsystem modeling the slower internal motions is solved explicitly using a much larger time step. Finally, if the baroclinic variables are advanced explicitly using a small time step, a time-averaging filter is applied over the barotropic solutions to minimize mode-splitting and aliasing errors (Shchepetkin & McWilliams, 2005). The resulting time-averaged barotropic solutions are then reconciled with their baroclinic counterparts to arrive at the total 3D states.

As an illustrative example, we briefly discuss the barotropic-baroclinic splitting in MPAS-Ocean. The MPAS-Ocean z-level formulation solves the following equations for thickness, momentum, and tracers at layer k:

$$\frac{\partial h_k}{\partial t} + \nabla \cdot \left(h_k^{edge} \boldsymbol{u}_k \right) + \frac{\partial}{\partial z} \left(h_k w_k \right) = 0, \tag{B1}$$

$$\frac{\partial \boldsymbol{u}_k}{\partial t} + \frac{1}{2} \nabla \left| \boldsymbol{u}_k \right|^2 + (\boldsymbol{k} \cdot \nabla \times \boldsymbol{u}_k) \boldsymbol{u}_k^{\perp} + f \boldsymbol{u}_k^{\perp} + w_k^{edge} \frac{\partial \boldsymbol{u}_k}{\partial z} = -\frac{1}{\rho_0} \nabla p_k + \nu_h \nabla^2 \boldsymbol{u}_k + \frac{\partial}{\partial z} \left(\nu_v \frac{\partial \boldsymbol{u}_k}{\partial z} \right), \tag{B2}$$

$$\frac{\partial h_k \varphi_k}{\partial t} + \nabla \cdot \left(h_k^{edge} \varphi_k^{edge} \boldsymbol{u}_k \right) + \frac{\partial}{\partial z} \left(h_k \varphi_k w_k \right) = \nabla \cdot \left(h_k^{edge} \kappa_h \nabla \varphi_k \right) + h_k \frac{\partial}{\partial z} \left(\kappa_v \frac{\partial \varphi_k}{\partial z} \right). \tag{B3}$$

The layer thickness h, vertical velocity w, pressure p, and tracer φ, are scalar quantities defined at the center of near-hexagonal cells of the primal MPAS-Ocean mesh. The horizontal velocity vector $\boldsymbol{u}$ and the variables with *edge* superscript are defined at the edges of the cells. The gradient, divergence and curl operators are all defined on the horizontal plane. The barotropic and baroclinic velocities are

$$\overline{\boldsymbol{u}} = \frac{\sum_{k=1}^{N^{edge}} h_k^{edge} \boldsymbol{u}_k}{\sum_{k=1}^{N^{edge}} h_k^{edge}}, \tag{B4}$$

$$\boldsymbol{u'}_k = \boldsymbol{u}_k - \overline{\boldsymbol{u}}, \quad k = 1, 2, \ldots, N. \tag{B5}$$

If H is the mean depth in the absence of bottom topography, $h_b(x, y)$ is the topographic height at (x, y), and η is the surface elevation or the sea surface height (SSH),

$$\eta = \sum_{k=1}^{N^{edge}} h_k - \{H - h_b(x, y)\}. \tag{B6}$$

Summing over all layers results in the barotropic surface elevation equation

$$\frac{\partial \eta}{\partial t} + \nabla \cdot \left(\overline{\boldsymbol{u}} \sum_{k=1}^{N^{edge}} h_k^{edge} \right) \equiv \frac{\partial \eta}{\partial t} + \nabla \cdot \left[\overline{\boldsymbol{u}} \left\{ \eta + H - h_b(x, y) \right\} \right] = 0, \tag{B7}$$

using the boundary conditions $w_{\frac{1}{2}} = w_{N+\frac{1}{2}} = 0$. Defining

$$\boldsymbol{T}\left(\boldsymbol{u}_k, w_k, p_k \right) = -\frac{1}{2} \nabla \left| \boldsymbol{u}_k \right|^2 - (\boldsymbol{k} \cdot \nabla \times \boldsymbol{u}_k) \boldsymbol{u}_k^{\perp} - w_k^{edge} \frac{\partial \boldsymbol{u}_k}{\partial z} - \frac{1}{\rho_0} \nabla p_k + \nu_h \nabla^2 \boldsymbol{u}_k + \frac{\partial}{\partial z} \left(\nu_v \frac{\partial \boldsymbol{u}_k}{\partial z} \right), \tag{B8}$$

(B2) can be written in the more compact form

$$\frac{\partial \boldsymbol{u}_k}{\partial t} + f\boldsymbol{u}_k^{\perp} = \boldsymbol{T}\left(\boldsymbol{u}_k, w_k, p_k\right). \tag{B9}$$

Extracting the barotropic component of (B9),

$$\frac{\partial \overline{\boldsymbol{u}}}{\partial t} + f\overline{\boldsymbol{u}}^{\perp} = \overline{\boldsymbol{T}}\left(\boldsymbol{u}_k, w_k, p_k\right) \equiv -g\nabla\eta + \overline{\boldsymbol{G}}, \tag{B10}$$

where $\overline{\boldsymbol{T}}$ is the barotropic average of $\boldsymbol{T}_k = \boldsymbol{T}\left(\boldsymbol{u}_k, w_k, p_k\right)$ over all layers computed similar to $\overline{\boldsymbol{u}}$ with $\boldsymbol{u}_k$ replaced by $\boldsymbol{T}_k$ in (B4), and $\overline{\boldsymbol{G}}$ is defined as $\overline{\boldsymbol{G}} = \overline{\boldsymbol{T}}\left(\boldsymbol{u}_k, w_k, p_k\right) + g\nabla\eta$. Subtracting the barotropic equation (B10) from the total momentum equation (B9), we obtain the baroclinic momentum equation

$$\frac{\partial \boldsymbol{u'}_k}{\partial t} + f\boldsymbol{u'}_k^{\perp} = \boldsymbol{T}\left(\boldsymbol{u}_k, w_k, p_k\right) + g\nabla\eta - \overline{\boldsymbol{G}}. \tag{B11}$$

It is evident that the barotropic equations (B7) and (B10) exhibit a resemblance to the inviscid inhomogeneous rotating shallow water equations. However, this similarity is marked by two key differences: the omission of the non-linear advection term and the incorporation of a source term $\overline{\boldsymbol{G}}$ within the barotropic momentum equation. This latter term, $\overline{\boldsymbol{G}}$, represents the barotropic average of $\boldsymbol{T}\left(\boldsymbol{u}_k, w_k, p_k\right) + g\nabla\eta$. The splitting procedure and the split equations may vary slightly among different ocean models. One variation, as observed in Blumberg and Mellor (1987), is to extract the diffusion of the barotropic velocity out of the $\overline{\boldsymbol{G}}$ term so that the barotropic momentum equation becomes equivalent to the viscous inhomogeneous linear rotating shallow water momentum equation

$$\frac{\partial \overline{\boldsymbol{u}}}{\partial t} + f\overline{\boldsymbol{u}}^{\perp} = -g\nabla\eta + \nu_h\nabla^2\overline{\boldsymbol{u}} + \overline{\boldsymbol{G}}. \tag{B12}$$

Appendix C Details of Numerical Implementation

In this section, we discuss subtle details in the numerical implementation of the shallow water equations. Constructing the initial-boundary value problem to numerically obtain the solution of the various test cases necessitates careful attention, particularly in ensuring that the initial and boundary conditions are correctly applied on hexagonal meshes, and the source terms for the manufactured solutions are exact. We will methodically tackle these aspects, using a uniform MPAS-Ocean mesh with hexagonal primal cells and triangular dual cells as a case study. The discussion culminates with addressing the crucial process of interpolating the numerical solution or the error to the coarsest spatial mesh, before calculating the error norm, for refinement only in space.

C1 Specifying Initial and Boundary Conditions on Hexagonal Meshes

For MPAS-Ocean, the prognostic variables are the surface elevations defined at the centers of the primal cells and the normal velocities defined at the primal cell edges. The spatial discretization of MPAS-Ocean based on the TRiSK scheme belongs to the category of finite volume methods, which study the time evolution of cell- and edge-averaged quantities in two dimensions, as opposed to the cell- and edge-centered ones. So, for a test case, it is imperative to adopt an averaging procedure to determine the mean values of the prognostic variables within every cell and edge. Since the cell-averaged quantity is the cell-integrated quantity divided by the cell area, we need to first integrate the quantity over the area spanned by a hexagonal cell. If the quantity consists of a complex combination of polynomial, trigonometric, and exponential functions, performing the integration analytically may be a Herculean task if not impossible. So, we resort to numerical quadrature, which may not be exact but is definitely more accurate than the value at the cell center times the area of the cell. Rules for evaluating numerical quadrature on regular hexagons first appeared in

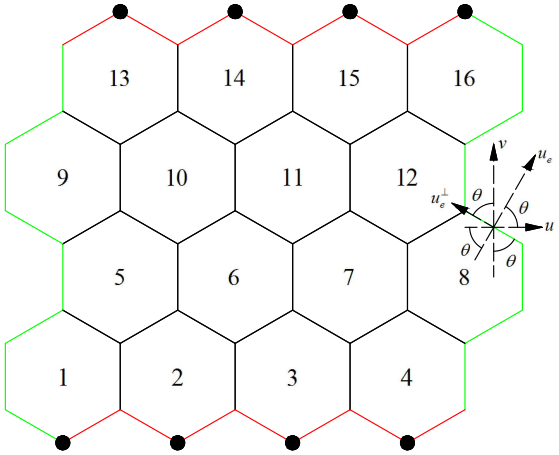

Figure C1. A 4×4 MPAS-Ocean mesh with non-periodic zonal and periodic meridional boundaries, showing the components of zonal and meridional velocities normal and tangential to an edge.

Stroud (1971) followed by Lyness and Monegato (1977). In all test cases, we employ Lyness' rule for integrating any scalar quantity over the hexagonal MPAS-Ocean cells. For exact evaluation of the integral of polynomials upto degree 15 over the unit hexagon inscribed within the unit circle centered at the origin, Table A.1 in Lyness and Monegato (1977) lists the number of quadrature points, their coordinates, and weights.

We use the Gauss-Legendre quadrature method to specify the edge-averaged normal velocity at the midpoint of

(a) every edge for the initial condition,
(b) every edge along a non-periodic boundary for the boundary condition.

Figure C1 is a schematic of a 4×4 MPAS-Ocean mesh with periodic zonal and non-periodic meridional boundaries. It also shows the resolution of the zonal and meridional velocities in the normal and tangential directions of a non-periodic boundary edge. Since the prognostic variables include only the normal and not the tangential velocity, we do not lose any generality by conducting a test case with zero zonal velocity (e.g. the Coastal Kelvin wave) or one with zero meridional velocity (e.g. the non-linear manufactured solution) since the normal velocity on these hexagonal MPAS-Ocean meshes will, in general, remain non-zero in either case.

C2 Specifying Source Terms for Manufactured Solutions

The non-linear manufactured solution (38) satisfies inhomogeneous non-linear rotating inviscid shallow water equations (38) on a flat bottom. The source terms (40) are obtained by inserting the manufactured solution and its spatial and temporal gradients into the left-hand side of these equations. On a hexagonal MPAS-Ocean mesh, the source term for the normal velocity on an edge, where the normal makes an angle θ with the positive direction of the x-axis is

$$s^{u^n} = s^u \cos\theta + s^v \sin\theta. \tag{C1}$$

The cell-averaged source term for the surface elevation and the edge-averaged one for the normal velocity can be obtained by following the same procedure outlined in Section C1 for computing the cell-averaged surface elevation and the edge-averaged normal velocity.

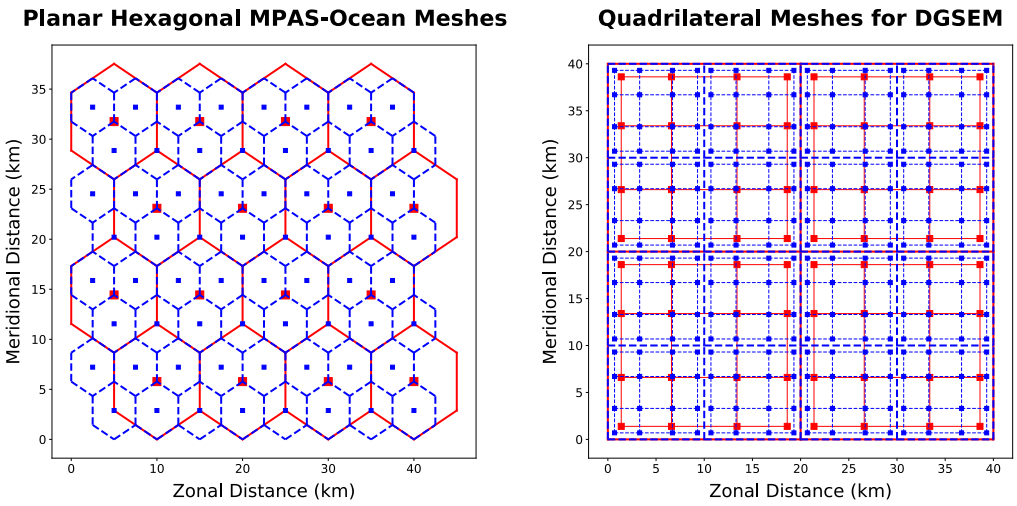

Figure C2. (a) A planar hexagonal MPAS-Ocean mesh consisting of 8 cells of width 5 km in each horizontal direction (in blue), superimposed on a coarser mesh consisting of 4 cells of width 10 km in each direction (in red) on the left. (b) A discontinuous Galerkin spectral element mesh (DGSEMesh) consisting of 4 elements of width 10 km and polynomial basis functions of order 4 in each horizontal direction (in blue) superimposed on a coarser mesh consisting of 2 elements of width 20 km and the same polynomial order in each direction (in red) on the right.

C3 Interpolation to the Coarsest Mesh

As a final note, for refinement only in space, we need to interpolate the numerical solution (or the error) to the coarsest mesh before taking the difference in the numerical solution (or the error) for successive spatial resolutions and computing its norm. Figure C2 illustrates (a) a planar hexagonal MPAS-Ocean mesh consisting of 8 cells of width 5 km in each horizontal direction (in blue), superimposed on a coarser mesh consisting of 4 cells of width 10 km in each direction (in red); and (b) a discontinuous Galerkin spectral element mesh (DGSEMesh) consisting of 4 elements of width 10 km and polynomial basis functions of order 4 in each horizontal direction (in blue) superimposed on a coarser mesh consisting of 2 elements of width 20 km and the same polynomial order in each direction (in red). The cell centers of the MPAS-Ocean meshes and the quadrature nodes within each element of the DGSEMeshes are represented by square markers. In Figure C2(a), the numerical solution (or the error) on the finer mesh is interpolated to the coarser mesh with a bilinear interpolant (Vetterling & Press, 1992). In Figure C2(b), a Newton-Raphson method is used to determine the physical coordinates of the quadrature nodes of the coarser mesh with respect to the computational coordinates of the quadrature nodes of the finer mesh. Then, the polynomial representation of the solution (or the error) on the finer mesh is evaluated at these physical coordinates.

Open Research Section

The model code and visualization scripts may be accessed from the GitHub repository at `https://github.com/siddharthabishnu/Rotating_Shallow_Water_Verification_Suite/tree/v1.2.5`, and may also be downloaded from the Zenodo release (Bishnu, 2024a) at `https://doi.org/10.5281/zenodo.10460245`. The mesh files (Bishnu, 2023) used for initialization, may be obtained from `https://doi.org/10.5281/zenodo.10161055`, and

the output files (Bishnu, 2024b) including the solution, error and convergence plots, may be downloaded from `https://doi.org/10.5281/zenodo.10460252`.

Acknowledgments

Siddhartha Bishnu has been supported by Scientific Discovery through Advanced Computing (SciDAC) projects LEAP (Launching an Exascale ACME Prototype) and CANGA (Coupling Approaches for Next Generation Architectures) under the U.S. Department of Energy (DOE), Office of Science, Office of Biological and Environmental Research (BER). Mark Petersen was supported as part of the Energy Exascale Earth System Model (E3SM) project, also funded by the DOE BER. This research used resources provided by the Los Alamos National Laboratory Institutional Computing Program, which is supported by the U.S. Department of Energy National Nuclear Security Administration under Contract No. 89233218CNA000001.

The authors extend their profound gratitude to the anonymous reviewers for their constructive feedback, encouraging comments, and invaluable recommendations. Their contributions have been instrumental in enhancing both the quality and the presentation of this paper. Additionally, the authors recognize the beneficial interactions with Tomasz Plewa and Sachin Shanbhag at the Florida State University and Darren Engwirda at the Los Alamos National Laboratory.

References

Asay-Davis, X., & Begeman, C. (2024). *Polaris.* `https://github.com/E3SM-Project/polaris`. GitHub.

Asay-Davis, X., Begeman, C., & Petersen, M. (2024). *COMPASS (Configuration Of Model for Prediction Across Scales Setups) repository.* `https://github.com/MPAS-Dev/compass`. GitHub.

Baldwin, M., Gray, L., Dunkerton, T., Hamilton, K., Haynes, P., Randel, W. J., ... others (2001). The quasi-biennial oscillation. *Reviews of Geophysics*, *39*(2), 179–229.

Barbeiro, S., Ferreira, J., & Grigorieff, R. (2005). Supraconvergence of a finite difference scheme for solutions in h s (0, l). *IMA journal of numerical analysis*, *25*(4), 797–811.

Bassi, F., & Rebay, S. (1997). A high-order accurate discontinuous finite element method for the numerical solution of the compressible navier–stokes equations. *Journal of computational physics*, *131*(2), 267–279.

Bathe, K.-J. (2006). *Finite element procedures.* Klaus-Jurgen Bathe.

Beel, A., Kim, T.-Y., Jiang, W., & Song, J.-H. (2019). Strong form-based meshfree collocation method for wind-driven ocean circulation. *Computer Methods in Applied Mechanics and Engineering*, *351*, 404–421.

Bishnu, S. (2021). *Time-Stepping Methods for Partial Differential Equations and Ocean Models* (Doctoral dissertation, Florida State University). doi: 10.5281/zenodo.7439539

Bishnu, S. (2023, November). *MPAS-Ocean Shallow Water Meshes.* Zenodo. Retrieved from `https://doi.org/10.5281/zenodo.10161055` doi: 10.5281/zenodo.10161055

Bishnu, S. (2024a, January). *Rotating shallow water verification suite.* Zenodo. Retrieved from `https://doi.org/10.5281/zenodo.10460245` doi: 10.5281/zenodo.10460245

Bishnu, S. (2024b, January). *Rotating shallow water verification suite output.* Zenodo. Retrieved from `https://doi.org/10.5281/zenodo.10460252` doi: 10.5281/zenodo.10460252

Bishnu, S., Strauss, R. R., & Petersen, M. R. (2023). Comparing the Performance of Julia on CPUs versus GPUs and Julia-MPI versus Fortran-MPI: a case study with MPAS-Ocean (Version 7.1). *Geoscientific Model Development*, *16*(19), 5539–5559. Retrieved from `https://gmd.copernicus.org/articles/16/5539/2023/` doi: 10.5194/gmd-16-5539-2023

Blackburn, M., & Hoskins, B. J. (2013). Context and aims of the aqua-planet experiment. *Journal of the Meteorological Society of Japan. Ser. II*, *91*, 1–15.

Blackburn, M., Williamson, D. L., Nakajima, K., Ohfuchi, W., Takahashi, Y. O., Hayashi, Y.-Y., ... others (2013). The aqua-planet experiment (ape): Control sst simulation. *Journal of the Meteorological Society of Japan. Ser. II*, *91*, 17–56.

Blumberg, A. F., & Mellor, G. L. (1987). A description of a three-dimensional coastal ocean circulation model. *Three-dimensional coastal ocean models*, *4*, 1–16.

Boyd, J. P. (1988). Spectral methods in fluid dynamics (c. canuto, my hussaini, a. quarteroni, and ta zang). *SIAM Review*, *30*(4), 666–668.

Burchard, H., & Rennau, H. (2008). Comparative quantification of physically and numerically induced mixing in ocean models. *Ocean Modelling*, *20*(3), 293–311.

Calandrini, S., Engwirda, D., & Petersen, M. (2021). Comparing numerical accuracy and stability for different horizontal discretizations in MPAS-Ocean. *Ocean Modelling*, *168*, 101908. Retrieved from `https://www.sciencedirect.com/science/article/pii/S146350032100161X` doi: https://doi.org/10.1016/j.ocemod.2021.101908

Canuto, C., Hussaini, M. Y., Quarteroni, A., & Zang, T. A. (2007a). *Spectral methods: evolution to complex geometries and applications to fluid dynamics*. Springer Science & Business Media.

Canuto, C., Hussaini, M. Y., Quarteroni, A., & Zang, T. A. (2007b). *Spectral methods: fundamentals in single domains*. Springer Science & Business Media.

Capodaglio, G., & Petersen, M. (2022). Local time stepping for the shallow water equations in MPAS. *Journal of Computational Physics*, *449*, 110818. Retrieved from `https://www.sciencedirect.com/science/article/pii/S0021999121007130` doi: https://doi.org/10.1016/j.jcp.2021.110818

Carpenter, M. H., & Kennedy, C. A. (1994). *Fourth-order 2N-storage Runge-Kutta schemes.* Langley Research Center.

Chavas, D. R., & Reed, K. A. (2019). Dynamical aquaplanet experiments with uniform thermal forcing: System dynamics and implications for tropical cyclone genesis and size. *Journal of the Atmospheric Sciences*, *76*(8), 2257–2274.

Chen, C., Beardsley, R. C., & Cowles, G. (2006, March). An unstructured grid, finite-volume coastal ocean model (fvcom) system. *Oceanography*, *19*, 78–89. Retrieved from `https://doi.org/10.5670/oceanog.2006.92`

Chen, Q., & Ju, L. (2018). Conservative finite-volume schemes for the quasi-geostrophic equation on coastal-conforming unstructured primal–dual meshes. *Quarterly Journal of the Royal Meteorological Society*, *144*(713), 1106–1122.

Clarke, A. J. (1991). The dynamics of barotropic tides over the continental shelf and slope. *Tidal Hydrodynamics*, *79*, 108.

Clarke, A. J. (2008). *An introduction to the dynamics of el niño and the southern oscillation.* Elsevier.

Clarke, A. J., & Battisti, D. S. (1981). The effect of continental shelves on tides. *Deep Sea Research Part A. Oceanographic Research Papers*, *28*(7), 665–682.

Cockburn, B., & Shu, C.-W. (1989). Tvb runge-kutta local projection discontinuous galerkin finite element method for conservation laws. ii. general framework. *Mathematics of computation*, *52*(186), 411–435.

Cockburn, B., & Shu, C.-W. (1998). The runge–kutta discontinuous galerkin method for conservation laws v: multidimensional systems. *Journal of computational physics*, *141*(2), 199–224.

Comblen, R., Lambrechts, J., Remacle, J.-F., & Legat, V. (2010). Practical evaluation of five partly discontinuous finite element pairs for the non-conservative shallow water equations. *International Journal for Numerical Methods in Fluids*, *63*(6), 701–724.

Cushman-Roisin, B., & Beckers, J.-M. (2011). *Introduction to geophysical fluid dynamics: physical and numerical aspects*. Academic press.

Danilov, S., Kivman, G., & Schröter, J. (2004). A finite-element ocean model: principles and evaluation. *Ocean Modelling*, *6*(2), 125–150.

Dennis, J. M., Edwards, J., Evans, K. J., Guba, O., Lauritzen, P. H., Mirin, A. A., ...

Worley, P. H. (2012). Cam-se: A scalable spectral element dynamical core for the community atmosphere model. *The International Journal of High Performance Computing Applications*, *26*(1), 74–89.

Donea, J., & Huerta, A. (2003). *Finite element methods for flow problems*. John Wiley & Sons.

Donohoe, A., Frierson, D. M., & Battisti, D. S. (2014). The effect of ocean mixed layer depth on climate in slab ocean aquaplanet experiments. *Climate dynamics*, *43*(3-4), 1041–1055.

Drago, M., & Iovenitti, L. (2000). σ-coordinates hydrodynamic numerical model for coastal and ocean three-dimensional circulation. *Ocean Engineering*, *27*(10), 1065–1085.

Düben, P. D., Korn, P., & Aizinger, V. (2012). A discontinuous/continuous low order finite element shallow water model on the sphere. *Journal of Computational Physics*, *231*(6), 2396–2413.

Evans, K. J., Archibald, R. K., Gardner, D. J., Norman, M. R., Taylor, M. A., Woodward, C. S., & Worley, P. H. (2019). Performance analysis of fully explicit and fully implicit solvers within a spectral element shallow-water atmosphere model. *The International Journal of High Performance Computing Applications*, *33*(2), 268–284.

Eymard, E., Gallouët, T., & Herbin, R. (2003). *Finite volume method handbook of numerical analysis, editors: Pg ciarlet and jl lions, vol. 70.* Amsterdam, North Holland.

Ezer, T., & Mellor, G. L. (2004). A generalized coordinate ocean model and a comparison of the bottom boundary layer dynamics in terrain-following and in z-level grids. *Ocean Modelling*, *6*(3-4), 379–403.

Farlow, S. J. (1993). *Partial differential equations for scientists and engineers*. Courier Corporation.

Ferreira, J. A., & Grigorieff, R. D. (1998). On the supraconvergence of elliptic finite difference schemes. *Applied numerical mathematics*, *28*(2-4), 275–292.

Foster, E. L., Iliescu, T., & Wang, Z. (2013). A finite element discretization of the streamfunction formulation of the stationary quasi-geostrophic equations of the ocean. *Computer Methods in Applied Mechanics and Engineering*, *261*, 105–117.

Fringer, O., Gerritsen, M., & Street, R. (2006). An unstructured-grid, finite-volume, nonhydrostatic, parallel coastal ocean simulator. *Ocean Modelling*, *14*(3-4), 139–173.

Garcia, M., Choboter, P. F., Walter, R. K., & Castillo, J. E. (2019). Validation of the nonhydrostatic general curvilinear coastal ocean model (gccom) for stratified flows. *Journal of computational science*, *30*, 143–156.

Gassner, G. J., Winters, A. R., & Kopriva, D. A. (2016). A well balanced and entropy conservative discontinuous galerkin spectral element method for the shallow water equations. *Applied Mathematics and Computation*, *272*(P2), 291-308. Retrieved from `https://EconPapers.repec.org/RePEc:eee:apmaco:v:272:y:2016:i:p2:p:291-308`

Gibson, A. H., Hogg, A. M., Kiss, A. E., Shakespeare, C. J., & Adcroft, A. (2017). Attribution of horizontal and vertical contributions to spurious mixing in an arbitrary Lagrangian–Eulerian ocean model. *Ocean Modelling*, *119*, 45–56.

Gill, A. E. (2016). *Atmosphere—ocean dynamics*. Elsevier.

Griffies, S. M., Gnanadesikan, A., Dixon, K. W., Dunne, J. P., Gerdes, R., Harrison, M. J., ... Zhang, R. (2005, September). Formulation of an ocean model for global climate simulations. *Ocean Sci.*, *1*(1), 45–79. Retrieved 2018-02-21, from `https://www.ocean-sci.net/1/45/2005/` doi: 10.5194/os-1-45-2005

Haberman, R. (1998). *Elementary applied partial differential equations: With fourier series and boundary value problems*. Prentice-Hall.

Haidvogel, D. B., & Beckmann, A. (1999). *Numerical ocean circulation modeling*. World Scientific.

Hecht, M. W., Wingate, B. A., & Kassis, P. (2000). A better, more discriminating test problem for ocean tracer transport. *Ocean Modelling*, *2*(1-2), 1–15.

Hell, M. C. (2020). *Atmosphere-ocean momentum exchange by extra-tropical storms*. University of California, San Diego.

Herzfeld, M., Schmidt, M., Griffies, S., & Liang, Z. (2011). Realistic test cases for limited area ocean modelling. *Ocean Modelling*, *37*(1-2), 1–34.

Hesthaven, J., & Warburton, T. (2007). *Nodal discontinuous galerkin methods: Algorithms, analysis, and applications*. Springer Science & Business Media.

Hughes, T. (2012). *The finite element method: Linear static and dynamic finite element analysis*. Dover Publications.

Hussaini, M. Y., & Zang, T. A. (1987). Spectral methods in fluid dynamics. *Annual review of fluid mechanics*, *19*(1), 339–367.

Ilıcak, M., Adcroft, A. J., Griffies, S. M., & Hallberg, R. W. (2012). Spurious dianeutral mixing and the role of momentum closure. *Ocean Modelling*, *45*, 37–58.

Jalali, M., Rapaka, N. R., & Sarkar, S. (2014). Tidal flow over topography: effect of excursion number on wave energetics and turbulence. *Journal of fluid mechanics*, *750*, 259–283.

Jankowski, J. A. (1999). *A non-hydrostatic model for free surface flows* (Unpublished doctoral dissertation). Inst. für Strömungsmechanik und Elektronisches Rechnen im Bauwesen.

Jiang, W., & Kim, T.-Y. (2016). Spline-based finite-element method for the stationary quasi-geostrophic equations on arbitrary shaped coastal boundaries. *Computer Methods in Applied Mechanics and Engineering*, *299*, 144–160.

Kärnä, T., Kramer, S. C., Mitchell, L., Ham, D. A., Piggott, M. D., & Baptista, A. M. (2018). Thetis coastal ocean model: discontinuous galerkin discretization for the three-dimensional hydrostatic equations. *Geoscientific Model Development*, *11*(11), 4359–4382.

Kärnä, T., Legat, V., & Deleersnijder, E. (2013). A baroclinic discontinuous galerkin finite element model for coastal flows. *Ocean Modelling*, *61*, 1–20.

Karniadakis, G., & Sherwin, S. (2005). *Spectral/hp element methods for computational fluid dynamics*. Numerical Mathematics and Scie.

Kim, T.-Y., Iliescu, T., & Fried, E. (2015). B-spline based finite-element method for the stationary quasi-geostrophic equations of the ocean. *Computer Methods in Applied Mechanics and Engineering*, *286*, 168–191.

Kopera, M. A., Gahounzo, Y., Enderlin, E. M., Giraldo, F. X., & Maslowski, W. (2023). Non-hydrostatic unified model of the ocean with application to ice/ocean interaction modeling. *GEM-International Journal on Geomathematics*, *14*(1), 2.

Kopera, M. A., Giraldo, F. X., & Maslowski, W. (2018). *Ice-sheet/ocean interaction model for greenland fjords using high-order discontinuous galerkin methods* (Tech. Rep.). University of California, Santa Cruz/Naval Postgraduate School.

Kopriva, D., & Gassner, G. (2010, 08). On the quadrature and weak form choices in collocation type discontinuous galerkin spectral element methods. *J. Sci. Comput.*, *44*, 136-155. doi: 10.1007/s10915-010-9372-3

Kopriva, D. A. (2009). *Implementing spectral methods for partial differential equations: Algorithms for scientists and engineers*. Springer Science & Business Media.

Kopriva, D. A., Nordström, J., & Gassner, G. J. (2017). Error boundedness of discontinuous galerkin spectral element approximations of hyperbolic problems. *Journal of Scientific Computing*, *72*, 314–330.

Lax, P. D., & Richtmyer, R. D. (1956). Survey of the stability of linear finite difference equations. *Communications on pure and applied mathematics*, *9*(2), 267–293.

Legg, S., Hallberg, R. W., & Girton, J. B. (2006). Comparison of entrainment in overflows simulated by z-coordinate, isopycnal and non-hydrostatic models. *Ocean Modelling*, *11*(1-2), 69–97.

LeVeque, R. J. (2002). *Finite volume methods for hyperbolic problems* (Vol. 31). Cambridge university press.

Levine, N. (1985). Superconvergent recovery of the gradient from piecewise linear finite-element approximations. *IMA Journal of numerical analysis*, *5*(4), 407–427.

Logan, D. L. (2022). *First course in the finite element method, enhanced edition, si version*. Cengage Learning.

Logan, J. D. (2014). *Applied partial differential equations*. Springer.

Lyness, J., & Monegato, G. (1977). Quadrature rules for regions having regular hexagonal symmetry. *SIAM Journal on Numerical Analysis*, *14*(2), 283–295.

Maday, Y., & Patera, A. T. (1989). Spectral element methods for the incompressible navier-stokes equations. *IN: State-of-the-art surveys on computational mechanics (A90-47176 21-64). New York*, 71–143.

Madec, G., et al. (2023, July). *Nemo ocean engine reference manual*. Zenodo. Retrieved from `https://doi.org/10.5281/zenodo.8167700` doi: 10.5281/zenodo.8167700

Marshall, J., Adcroft, A., Hill, C., Perelman, L., & Heisey, C. (1997). A finite-volume, incompressible Navier Stokes model for studies of the ocean on parallel computers. *Journal of Geophysical Research: Oceans*, *102*(C3), 5753–5766.

Medeiros, B., Williamson, D. L., & Olson, J. G. (2016). Reference aquaplanet climate in the c ommunity a tmosphere m odel, v ersion 5. *Journal of Advances in Modeling Earth Systems*, *8*(1), 406–424.

Merlis, T. M., & Held, I. M. (2019). Aquaplanet simulations of tropical cyclones. *Current Climate Change Reports*, *5*(3), 185–195.

Möbis, B., & Stevens, B. (2012). Factors controlling the position of the intertropical convergence zone on an aquaplanet. *Journal of Advances in Modeling Earth Systems*, *4*(4).

Munk, W. H., & Carrier, G. F. (1950). The wind-driven circulation in ocean basins of various shapes. *Tellus*, *2*(3), 158–167.

Myers, P. G., & Weaver, A. J. (1995). A diagnostic barotropic finite-element ocean circulation model. *Journal of Atmospheric and Oceanic Technology*, *12*(3), 511–526.

Neale, R. B., & Hoskins, B. J. (2000). A standard test for agcms including their physical parametrizations: I: The proposal. *Atmospheric Science Letters*, *1*(2), 101–107.

Patankar, S. (2018). *Numerical heat transfer and fluid flow*. Taylor & Francis.

Patera, A. (1984). A spectral element method for fluid dynamics: Laminar flow in a channel expansion. *Journal of Computational Physics*, *54*(3), 468-488.

Pedlosky, J. (1987). *Geophysical fluid dynamics* (Vol. 710). Springer.

Petersen, M. R., Jacobsen, D. W., Ringler, T. D., Hecht, M. W., & Maltrud, M. E. (2015). Evaluation of the arbitrary Lagrangian–Eulerian vertical coordinate method in the MPAS-Ocean model. *Ocean Modelling*, *86*, 93–113.

Philander, S., Holton, J., & Dmowska, R. (1989). *El nino, la nina, and the southern oscillation*. Elsevier Science. Retrieved from `https://books.google.com/books?id=9fwrkW\_B1YYC`

Ramadhan, A., Wagner, G. L., Hill, C., Campin, J.-M., Churavy, V., Besard, T., ... Marshall, J. (2020). Oceananigans.jl: Fast and friendly geophysical fluid dynamics on gpus. *Journal of Open Source Software*, *5*(53), 2018. Retrieved from `https://doi.org/10.21105/joss.02018` doi: 10.21105/joss.02018

Ranocha, H. (2016, dec). Shallow water equations: split-form, entropy stable, well-balanced, and positivity preserving numerical methods. *GEM - International Journal on Geomathematics*, *8*(1), 85–133. Retrieved from `https://doi.org/10.1007%2Fs13137-016-0089-9` doi: 10.1007/s13137-016-0089-9

Reckinger, S. M., Petersen, M. R., & Reckinger, S. J. (2015). A study of overflow simulations using MPAS-Ocean: Vertical grids, resolution, and viscosity. *Ocean Modelling*, *96, Part 2*, 291 - 313. Retrieved from `http://www.sciencedirect.com/science/article/pii/S146350031500164X` doi: http://dx.doi.org/10.1016/j.ocemod.2015.09.006

Reddy, J. N. (2019). *Introduction to the finite element method*. McGraw-Hill Education.

Ringler, T., Petersen, M., Higdon, R., Jacobsen, D., Jones, P., & Maltrud, M. (2013). A multi-resolution approach to global ocean modeling. *Ocean Modelling*, *69*(0), 211-232. Retrieved from `http://www.sciencedirect.com/science/article/pii/S1463500313000760` doi: http://dx.doi.org/10.1016/j.ocemod.2013.04.010

Ringler, T. D., Thuburn, J., Klemp, J. B., & Skamarock, W. C. (2010). A unified approach to energy conservation and potential vorticity dynamics for arbitrarily-structured

C-grids. *Journal of Computational Physics*, *229*(9), 3065–3090.
Roache, P. J. (2002). Code verification by the method of manufactured solutions. *J. Fluids Eng.*, *124*(1), 4–10.
Rotundo, N., Kim, T.-Y., Jiang, W., Heltai, L., & Fried, E. (2016). Error analysis of a b-spline based finite-element method for modeling wind-driven ocean circulation. *Journal of Scientific Computing*, *69*(1), 430–459.
Rusanov, V. (1961). Calculation of interaction of non-steady schock waves with obstacles. *J. Comp. Math. Phys*, *1*, 267–279.
Salari, K., & Knupp, P. (2000). *Code verification by the method of manufactured solutions* (Tech. Rep.). Sandia National Labs., Albuquerque, NM (US).
Santilli, E., & Scotti, A. (2015). The stratified ocean model with adaptive refinement (somar). *Journal of Computational Physics*, *291*, 60–81.
Sarachik, E. S., & Cane, M. A. (2010). *The el nino-southern oscillation phenomenon*. Cambridge University Press.
Shchepetkin, A. F., & McWilliams, J. C. (2005). The regional oceanic modeling system (ROMS): a split-explicit, free-surface, topography-following-coordinate oceanic model. *Ocean modelling*, *9*(4), 347–404.
Smith, G. D. (1985). *Numerical solution of partial differential equations: finite difference methods*. Oxford university press.
Spotz, W. F., Smith, T. M., Demeshko, I. P., & Fike, J. A. (2015). Aeras: A next generation global atmosphere model. *Procedia Computer Science*, *51*, 2097–2106.
Stommel, H. (1948). The westward intensification of wind-driven ocean currents. *Eos, Transactions American Geophysical Union*, *29*(2), 202–206.
Strauss, W. A. (2007). *Partial differential equations: An introduction*. John Wiley & Sons.
Strohmaier, E., & Dongarra, J. (2023). *Top 500, the list.* Retrieved 2023-08-01, from `https://www.top500.org/`
Stroud, A. H. (1971). *Approximate calculation of multiple integrals.* Prentice-Hall.
Taylor, M., Tribbia, J., & Iskandarani, M. (1997). The spectral element method for the shallow water equations on the sphere. *Journal of Computational Physics*, *130*(1), 92–108.
Thomas, S. J., & Loft, R. D. (2002). Semi-implicit spectral element atmospheric model. *Journal of Scientific Computing*, *17*(1), 339–350.
Thuburn, J., Ringler, T. D., Skamarock, W. C., & Klemp, J. B. (2009). Numerical representation of geostrophic modes on arbitrarily structured C-grids. *Journal of Computational Physics*, *228*(22), 8321–8335.
Vallis, G. K. (2017). *Atmospheric and oceanic fluid dynamics*. Cambridge University Press.
Versteeg, H. K., & Malalasekera, W. (2007). *An introduction to computational fluid dynamics: the finite volume method*. Pearson education.
Vetterling, W. T., & Press, W. H. (1992). *Numerical recipes: example book c*. Cambridge University Press.
Vitousek, S., & Fringer, O. B. (2014). A nonhydrostatic, isopycnal-coordinate ocean model for internal waves. *Ocean Modelling*, *83*, 118–144.
Walko, R. L., & Avissar, R. (2008). The ocean–land–atmosphere model (olam). part i: Shallow-water tests. *Monthly Weather Review*, *136*(11), 4033–4044.
Wang, D.-P. (1984). Mutual intrusion of a gravity current and density front formation. *Journal of Physical Oceanography*, *14*(7), 1191–1199.
Wang, Q., Danilov, S., & Schröter, J. (2008). Comparison of overflow simulations on different vertical grids using the finite element ocean circulation model. *Ocean Modelling*, *20*(4), 313–335.
Wang, Q., Danilov, S., Sidorenko, D., Timmermann, R., Wekerle, C., Wang, X., ... Schröter, J. (2014). The finite element sea ice-ocean model (fesom) v. 1.4: formulation of an ocean general circulation model. *Geoscientific Model Development*, *7*(2), 663–693.
Williamson, D. L., Drake, J. B., Hack, J. J., Jakob, R., & Swarztrauber, P. N. (1992). A standard test set for numerical approximations to the shallow water equations in

spherical geometry. *Journal of Computational Physics*, *102*(1), 211–224.

Williamson, J. (1980). Low-storage runge-kutta schemes. *Journal of Computational Physics*, *35*(1), 48–56.

Zarzycki, C. M., Levy, M. N., Jablonowski, C., Overfelt, J. R., Taylor, M. A., & Ullrich, P. A. (2014). Aquaplanet experiments using cam's variable-resolution dynamical core. *Journal of Climate*, *27*(14), 5481–5503.

Zienkiewicz, O., Taylor, R., & Zhu, J. (2005). *The finite element method: Its basis and fundamentals*. Elsevier Butterworth-Heinemann.